Quantum Storage of Light Using Nanophotonic Resonators Coupled to Erbium Ion Ensembles

A thesis by
Ioana Craiciu

In Partial Fulfillment of the Requirements for the
Degree of
Doctor of Philosophy

CALIFORNIA INSTITUTE OF TECHNOLOGY
Pasadena, California

2020
Defended May 19, 2020

Ioana Craiciu
ORCID: 0000-0002-8670-0715

ACKNOWLEDGEMENTS

I would first like to acknowledge the direct contributions of several persons to this work. Andrei Faraon supervised and helped conceive all experiments.

Evan Miyazono was the lead researcher on the erbium quantum memory project from before I joined until his graduation in 2017. The setups he built and the Er^{3+}:Y_2SiO_5 spectroscopy and resonator design work he did laid the groundwork for the work described in this thesis.

Mi Lei joined this project in 2018. Her contributions to this work were countless and essential. Mi has participated in nearly all aspects of the experiments described in Chapters 5 and 6, including simulation, design, nanofabrication, and measurement.

Jake Rochman designed and fabricated the nanobeam resonator used in Chapter 5. He designed the hybrid resonator used in Chapter 6, and the nanofabrication process for that resonator. Jake contributed to the efficiency calculations in Chapter 3.

Jonathan Kindem contributed ideas for to experiment methods, and the simulations in Chapter 6 are adapted from his code. John Bartholomew contributed with rare earth ions theory and interpretation of spectroscopic data. John Bartholomew, Andrei Ruskuc, and Hirsh Kamakari built the superconducting magnets. Tian Xie built the laser frequency locking setup used in Chapter 6. The superhyperfine calculations were performed with the help of Yan Qi Huan, and based on similar calculations he performed for a different material.

Next, I would like to express my gratitude to the many who helped me get here.

Thank you to Andrei for taking me on as a grad student. Thank you for giving me space to discover and make mistakes while also being present to provide guidance. Thank you for your patience, and the reminders to “breathe and take it slow.” Thank you to Evan for taking me in as a first-year grad student and teaching me everything from the very basics. Thank you for your friendship. Thank you to Mi for everything you’ve given to this project. Without your hard work, your curiosity, and your valuable insights, nothing we’ve achieved would have been possible. Thank you to Jake for always being willing to help, and for inspiring me to do a good job with your high standards. Thank you to Jon for your always sharing ideas, and for making science look fun. Thank you to John for being a top-notch scientist and mentor and sharing your extensive knowledge with everyone in the group. Andrei

R. and Tian, thank you for always bringing your science A-game while also making work fun. Thank you to Dimi Cielecki for your work and enthusiasm. Daniel, Chun, Hirsh, and Yan Qi, thank you for the helpful discussions during subgroup meetings and beyond. Thank you to Tian and Amir for the mentorship early on. Thank you to everyone in the flat-optics subgroup for always keeping me on my toes with your fast progress and impressive results.

Thank you to my defense and candidacy committee, Kerry Vahala, Andrei Faraon, Oskar Painter, and Manuel Endres, for your time and your guidance.

Thank you to Chuting for being my officemate for 6 years as well as my friend. Thank you to my book club friends/dictators who forced me to think of the world outside rare-earth ions and also fed me snacks. Thank you to Heidi for your friendship and for keeping me fit through our morning swims. Thank you Phil for your friendship. Thanks to Andrei and Greg for the Great Physics Bakeoffs. Thank you to my music, drama and art teachers Kathrin Jakob, Kyle LaLone, Brian Brophy, and Jim Barry for the creative outlet.

Thank you to all the staff at Caltech who has make it possible for students to learn and do research: Cecilia Gamboa, Jennifer Blankenship, Christy Jenstad for the countlessly many things you do to support students; everyone at Caltech Facilities and everyone at Caltech Dining Services.

Thank you to my professors and mentors at Caltech and the University of Waterloo and my teachers at St. Mary's High School, St. Michael's Jr. High, John Costello Elementary, Sacred Heard Elementary, all in Calgary, Canada, and Principesa Ileana School in Bucharest, Romania. I wouldn't be where I am without you.

Thank you to my partner, Max Jones, for the support, for believing in me and for valuing my work. Thank you for your advice, for listening to many practice presentations and for the many proof-readings, including this thesis. Thank you to my friends from Calgary and Waterloo for being a constant source of inspiration, love, and goofiness. There's too many of you to name, but you know who you are. Thank you to my brother Traian, sister-in-law Ankita and father Daniel Craiciu for your support. And finally, thank you to my mother, Iuliana Craiciu. Thank you for always supporting me. Thank you for your fierce belief in my abilities, often expressed as world-class helicopter parenting. Thank you for forcing me to apply to Caltech when I was convinced I would never get in. Thank you for teaching me that hard work is rewarding and that the world is beautiful when one is curious about it.

ABSTRACT

This thesis presents on-chip quantum storage of telecommunication wavelength light using nanophotonic resonators coupled to erbium ions. Storage of light in an optical quantum memory has applications in quantum information and quantum communication. For example, long distance quantum communication using quantum repeater protocols is enabled by quantum memories. Efficient and broadband quantum memories can be made from resonators coupled to ensembles of atoms. Like other rare earth ions, erbium is appealing for quantum applications due to its long optical and hyperfine coherence times in the solid state at low temperatures. However, erbium is unique among rare earth ions in having an optical transition in the telecommunication C band (1540 nm), making it particularly appealing for quantum communication applications. In this work, we use nano-scale resonators coupled to erbium-167 ions in yttrium orthosilicate crystals ($^{167}Er^{3+}$:Y_2SiO_5).

We demonstrate quantum storage in two types of resonators. In a nanobeam photonic crystal resonator milled directly in $^{167}Er^{3+}$:Y_2SiO_5, we show storage of weak coherent states using the atomic frequency comb protocol. The storage fidelity for single photon states is estimated to be at least 93.7% ± 2.4% using decoy state analysis. Storage of up to 10 μs and multimode storage are demonstrated. Using a hybrid resonator based on amorphous silicon on $^{167}Er^{3+}$:Y_2SiO_5 and on-chip electrodes, we demonstrate a multifunctional memory using the atomic frequency comb protocol with DC Stark shift control. In addition to dynamic control of memory time, Stark shift control allows modifications to the frequency and bandwidth of stored light. We show tuning of the output pulse by ±20 MHz relative to the input pulse, and broadening of the pulse bandwidth by more than a factor of three. The storage efficiency in both devices was limited to $< 1\%$.

On the way to these results, we describe $^{167}Er^{3+}$:Y_2SiO_5 spectroscopy measurements including optical coherence times and hyperfine lifetimes below 1 K, and we estimate the linear DC Stark shift along two crystal directions. The design and fabrication of the on-chip resonators is presented. We discuss the limitations to storage time and efficiency, including superhyperfine coupling and resonator parameters, and we outline a path forward for improving the storage efficiency in these types of devices.

PUBLISHED CONTENT AND CONTRIBUTIONS

[1] Ioana Craiciu, Mi Lei, Jake Rochman, Jonathan M. Kindem, John G. Bartholomew, Evan Miyazono, Tian Zhong, Neil Sinclair, and Andrei Faraon. Nanophotonic quantum storage at telecommunication wavelength. *Phys. Rev. Applied*, 12:024062, Aug 2019. doi: 10.1103/PhysRevApplied.12.024062. URL https://link.aps.org/doi/10.1103/PhysRevApplied.12.024062. I.C. built experimental setup, participated in measurement and data processing, and wrote manuscript.

[2] Evan Miyazono*, Ioana Craiciu*, Amir Arbabi, Tian Zhong, and Andrei Faraon. Coupling erbium dopants in yttrium orthosilicate to silicon photonic resonators and waveguides. *Opt. Express*, 25(3):2863–2871, Feb 2017. doi: 10.1364/OE.25.002863. URL http://www.opticsexpress.org/abstract.cfm?URI=oe-25-3-2863. *These authors contributed equally to this work. I.C. participated in setting up experiment, nanofabrication, measurements, and data processing, and gave input on the manuscript.

TABLE OF CONTENTS

LIST OF ILLUSTRATIONS

LIST OF TABLES

NOMENCLATURE

AFC. Atomic frequency comb. A quantum memory protocol.

CRIB. Controlled reversible inhomogeneous broadening. A quantum memory protocol.

FWHM. Full width at half maximum.

SEMM. Stark echo modulation memory. A quantum memory protocol.

SNSPD. Superconducting nanowire single photon detector.

ZEFOZ. Zero first-order Zeeman transition.

Chapter 1

INTRODUCTION

In this work, we present on-chip quantum storage at 1540 nm, in the telecommunication C band, using a nanophotonic resonator. This is the first demonstration of on-chip quantum storage in the telecom C band and the first demonstration of quantum storage in $^{167}Er^{3+}$:Y_2SiO_5. Further, we use on-chip electrodes to realize a multifunctional device which can change the frequency and bandwidth of stored light, thus providing capabilities for linear processing of light pulses. On the way to these results, we present: spectroscopy on $^{167}Er^{3+}$:Y_2SiO_5 in new parameter regimes; the design and fabrication process for on-chip resonators and electrodes; the coupling between the nanophotonic resonator and an ensemble of ions and the effect of this coupling on storage efficiency; measurements with light at the single-photon level in a dilution fridge at sub-kelvin temperatures. We discuss the efficiency of storage in these devices, with a focus on limitations including device design and fabrication, and superhyperfine coupling in $^{167}Er^{3+}$:Y_2SiO_5. We then outline a path towards on-chip storage with high efficiency.

In this introductory chapter, we present the motivation for creating on-chip quantum memories for light, with a focus on application in quantum networks, and we summarize the current state of the art. At the end of this chapter we outline the structure of this thesis.

1.1 The Quantum Internet, Quantum Repeaters, and Quantum Memories

A quantum memory for light is a device that stores light coherently for some portion of time. Figure 1.1 shows the basic principles of a quantum memory. Quantum memories should be able to store light efficiently for a length of time determined by the application, and to store a quantum state encoded in light with high fidelity.

Quantum memories enable long distance quantum communication. The transfer of quantum information over large distances enables secure communication via quantum key distribution [13, 58]. Other applications of long distance quantum communication include improved clock synchronization, distributed quantum computing, and improved measurements including large baseline optical telescope networks [104].

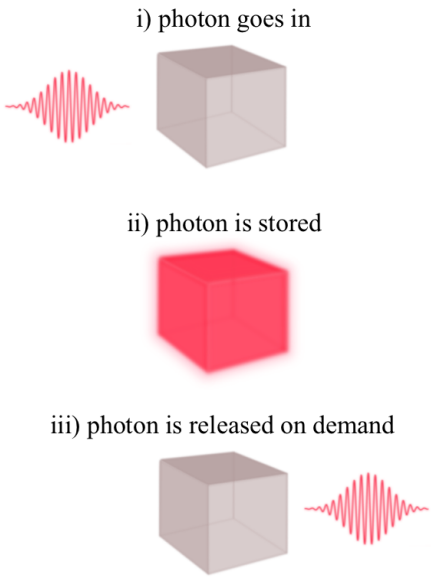

Figure 1.1: A quantum memory for light.

Due to their fast travel speed and low rates of decoherence, photons are a natural choice for transmitting quantum information. However, because quantum information cannot be amplified without introducing noise (the no-cloning theorem [108]), attenuation is a big problem for long distance quantum communication. Secure quantum key distribution through optical fibers has been demonstrated over distances up to 509 km [26]. The longest quantum communication link is 2000 km long between Beijing and Shanghai [111]. However, this link uses 32 trusted relays which are vulnerable to attacks. Demonstrations of satellite-to-ground quantum key distribution across 7600 km (using the satellite as a trusted relay) have shown that long distance optical quantum communication through free space is also promising [65].

Quantum repeaters enable long distance quantum communication without trusted relays beyond $\sim$ 500 km. Figure 1.2 shows a schematic of a quantum repeater network. The goal of the quantum repeater protocol, first introduced by Briegel et al. in 1998 [22], is to generate an entangled pair spanning a long distance A-B quickly and with high fidelity. This enables the transmission of quantum information over the channel using quantum teleportation. Entanglement distillation can be used to improve the fidelity of the final entangled state [20, 40]. Many types of quantum repeater protocols have been proposed. References [92] and [109] review protocols using atomic ensemble based memories.

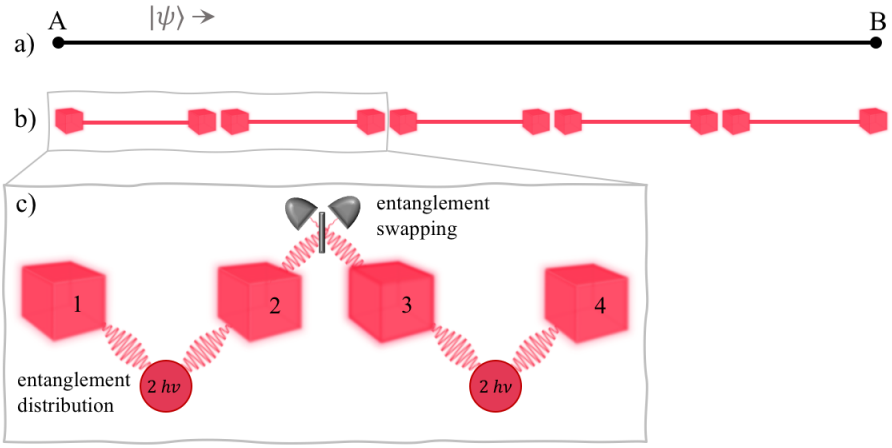

Figure 1.2: A quantum repeater network. a) In the simplest form, quantum communication works by sending quantum information over a channel from A to B. b) In a quantum repeater network, a long distance (A to B) is broken up into shorter segments. The boxes at the end of each segment represent quantum memories. c) A close up of two segments in the quantum repeater network. In the first step of a quantum repeater protocol, entanglement is shared across each segment. Here, this is accomplished by distributing entangled photon pairs, which are stored in quantum memories. In the second step, a Bell State measurement is performed on photons from adjacent memories (2 and 3) to swap entanglement: the photons in memories 1 and 4 are now entangled. Entanglement swapping continues until one entangled pair remains that spans the distance between A and B.

In order to synchronize the generation of entangled pairs across all segments, and then to store entangled pairs while swapping and distilling, most repeater protocols require quantum memories. Optical quantum memories for light have been proposed and demonstrated in a variety of systems [49] including single emitters such as NV and SiV centers [14], ensembles of cold atoms in a magneto-optical trap [53], warm atomic vapors [52], and ensembles of rare earth ions in crystals [47]. For single atoms or defect centers, the memory typically works by transferring the optical quantum state to a spin degree of freedom [8, 14, 58]. Many types of ensemble-based memories have been proposed and demonstrated.

The initial proposal for a quantum memory using atomic ensembles was using the DLCZ protocol, named after its creators [39]. Reference [92] analyzes several quantum repeater protocols using this type of memory. In the intervening years, many quantum storage protocols using ensembles of atoms have been proposed and realized [49]. Memory protocols including electromagnetically induced transparency (EIT) [41] and Raman scattering [59] use strong optical control pulses to read and

write information stored on spin transitions of an ensemble. Engineered absorption memories such as gradient echo memory (GEM) [5], controlled reversible inhomogeneous broadening (CRIB) [60], and atomic frequency comb (AFC) [4] store information in the optical transitions of an atomic ensemble. These protocols rely on spectral holeburning or quasi-static electric or magnetic fields to induce rephasing and emission of light stored in the ensemble. To extend memory times, optical control pulses can be used to transfer stored information from optical to spin transitions and back, but unlike in EIT and Raman memories, these control pulses do not coincide with the input or output pulses. Although the simple two-pulse photon echo involves rephasing and emission of light stored in an atomic ensemble, the associated population inversion leads to noise that renders this protocol unacceptable for quantum storage [88]. The revival of silenced echo (ROSE) protocol is an optical-pulse based storage protocol designed to avoid this inversion-induced noise [33]. References [21, 49] touch on a number of other proposed ensemble memory protocols.

For quantum memories to be useful in a real quantum repeater, they must be very efficient and their storage times must be sufficiently long. Most studies of "realistic" repeater protocols assume quantum memory efficiencies exceeding 90%. As a rule of thumb, the required memory time is given by the highest level of entanglement swapping, meaning storage time should equal the time it takes to create the final entangled pair spanning the distance A-B [92]. It is not trivial to estimate a typical entanglement rate (the inverse of the time it takes to create the final entangled pair), as it depends on many details, including the specific repeater scheme used, the total distance A-B, as well as the memory efficiency and memory time. Wu et al. studied entanglement rates for the realistic scenario where quantum memories have an exponentially decaying efficiency characterized by a decay constant. They predicted entanglement generation rates approaching 1 Hz for a 100 km distance and memory decay constants as low as 1 ms [109]. Another helpful metric for evaluating a quantum memory is whether it is superior to an optical fiber delay line in terms of efficiency vs. storage time. Most quantum memories realized to date are not [29].

Some progress has been made toward efficient and long-lived quantum memories for light. The record efficiency for storing coherent pulses is 92% using EIT in cold cesium atoms [53]. This result was for storing 895 nm light for 1 μs, although storage for up to $\sim$ 350 μs was shown with lower efficiency in the same work. For

storing a quantum state of light, the current record efficiency is 85% for storing a polarization qubit at 795 nm for 1 μs, using EIT in cold rubidium atoms [103]. For storage in solid state, the record storage efficiency of 76% used a cavity-enhanced EIT protocol in praseodymium doped Y_2SiO_5 (Pr^{3+}:Y_2SiO_5) [93]. Coherent pulses of 606 nm light were stored for 2 μs. Hedges et al. stored coherent pulses in Pr^{3+}:Y_2SiO_5 for 2 μs at 69% efficiency using the GEM protocol. Another notable result in solid state quantum memories is the storage of light for up to 1 minute using EIT in Pr^{3+}:Y_2SiO_5, albeit with efficiency lower than 1% [48]. These results show that, despite advancements in the last two decades, a highly efficient *and* long-lived quantum memory has yet to be achieved. Even so, there has been progress towards realizing elementary quantum networks using one or more memories [14, 102, 110].

The quantum storage protocol used in this work is the atomic frequency comb (AFC) protocol introduced by Afzelius et al. [4]. As detailed in Section 3.1 of this thesis, this protocol relies on spectral holeburning to shape the absorption spectrum of an ensemble into a comb. There are several advantages to the AFC protocol:

- For the basic protocol, only optical control is required.
- Optical control pulses are not required during memory readout. Control pulses during readout are a source of noise.
- The AFC bandwidth can be large, allowing multiplexing in frequency. Multiplexing can significantly improve entanglement generation rates in quantum repeater networks [96].

There have been many demonstrations of quantum storage using the AFC protocol since its introduction in 2008 [4, 34]. Storage of coherent pulses for up to 1 second was realized with the full AFC protocol (spin-wave AFC) in Eu^{3+}:Y_2SiO_5 at 580 nm, albeit with low efficiency. With cavity enhancement, also in Eu^{3+}:Y_2SiO_5, storage efficiencies of up to 52% at 2 μs were achieved using AFC in (12% at 15 μs using spin-wave AFC) [56]. The multimode capacity of this protocol was demonstrated in Reference [15], in which over 1000 temporal modes were stored at the same time in an AFC memory in Tm^{3+}:YAG (793 nm), and in Reference [97], in which 26 spectral modes were stored simultaneously in a Tm:$LiNbO_3$ waveguide (795 nm).

Most demonstrations of AFC storage have relied on crystals doped with ions such as europium, thulium, and praseodymium [94]. These ions, which have an even number of electrons, typically have long-lived hyperfine levels which enable spectral

holeburning, as well as the highly coherent optical and hyperfine transitions. For ions such as erbium, which has an odd number of electrons, electron spin coupling to other spins and phonons, as well as superhyperfine interactions, make it difficult to create atomic frequency combs. AFC storage in the optical transition was realized in erbium doped Y_2SiO_5 [63, 64], erbium doped fibers [91], and erbium doped lithium niobate waveguides [9], although with efficiency below 1% and short storage times. This sets the stage for the AFC storage in $^{167}Er^{3+}$:Y_2SiO_5 presented in this work. Recently, AFC storage with spin-wave was achieved using another rare earth ion with an unpaired electron, $^{171}Yb^{3+}$:Y_2SiO_5 [23]. In that work, Businger et al. leveraged the zero first-order Zeeman (ZEFOZ) hyperfine and optical transitions of $^{171}Yb^{3+}$:Y_2SiO_5 at zero field. They observed long-lived hyperfine states, as well as evidence of strongly suppressed superhyperfine coupling, which enabled AFC spin-wave storage of 979 nm light for up to 1.3 ms.

In addition to storing information, atomic ensembles can also be used to manipulate input states. The ability to adjust the temporal profile or frequency of stored light can be useful when quantum memories act as interfaces between multiple emitters, as in a quantum repeater network. For example, Hosseini et al. used a GEM scheme to modify the amplitude, bandwidth, and order of stored pulses [51]. In this work, we use electrodes in parallel or quadrupole configurations to change the memory time, as well as adjust the frequency and bandwidth of light stored using the AFC protocol. Lauritzen et al. used a similar scheme, where electric field control was used to modify the otherwise fixed memory time in an AFC without spin-wave [64].

1.2 $^{167}Er^{3+}$:Y_2SiO_5 for Optical Quantum Memories

Crystals doped with rare earth ions are an appealing platform for optical quantum memories because of the ions' long optical [17] and hyperfine [112] coherence times. As a solid state platform, it is straightforward to couple rare earth ion doped crystals to nanoscale resonators and on-chip components [35, 79, 84, 114, 115]. Ions across the lanthanide series are called rare earths despite their abundance in the earth's crust (iodine, silver, gold, and cadmium are rarer than most of the rare earths). The long coherence times of rare earth ions, even in the solid state, stem from their unique electronic structure, in which the electrons participating in optical transitions are in the partially occupied 4f shell, which is shielded from the environment by the electrons in the 5s and 5p shells [66].

Erbium is particularly interesting because it is the only rare earth ion with an

optical transition in the telecommunication C band, at 1540 nm. This is important for long distance quantum communication applications because standard optical fiber has the lowest attenuation in the C band, at ~ 0.17 dB/km. For this reason, erbium has been extensively studied for quantum memory applications. We have already mentioned some initial erbium quantum storage demonstrations using AFC, including Er^{3+}:Y_2SiO_5 [63, 64], erbium doped fibers [91], and lithium niobate waveguides [9]. The storage efficiencies in these works were limited in part by the lack of suitable long-lived shelving states in the erbium ions in these hosts. Using the ROSE protocol, which does not require any state preparation, storage of coherent optical states in Er^{3+}:Y_2SiO_5 for 16 μs with an efficiency of 42% was shown [32].

For memory protocols requiring spectral holeburning such as AFC, erbium doped materials pose some challenges. Natural isotopic abundance erbium is 23% ^{167}Er, which has nuclear spin $I = \frac{7}{2}$, with the balance comprised entirely of isotopes with zero nuclear spin, predominantly ^{166}Er, ^{168}Er, and ^{170}Er. This means that in crystals doped with natural abundance erbium, most erbium ions do not have long lived hyperfine states in the optical ground state. In the absence of hyperfine states, spectral holeburning can be achieved using Zeeman (electron spin levels). In initial studies of holeburning and AFC storage in Er^{3+}:Y_2SiO_5 [46, 62, 63], the ratio between the Zeeman lifetime and the optical lifetime was found to be too low for good holeburning.

It is therefore advantageous to use ^{167}Er doped materials, which do have hyperfine ground states, for spectral holeburning based memories such as AFC. Rančić et al. found that long lived spectral holes could exist in $^{167}Er^{3+}$:Y_2SiO_5, provided the electron spin was frozen using large fields (> 3 T) and low temperatures (1.4 K) [86]. In the same work, Rančić et al. measured hyperfine coherence times longer than 1 s, which would be important for AFC spin-wave storage. In this work, we use $^{167}Er^{3+}$:Y_2SiO_5 at lower fields (0.4 – 1 T), and also lower temperatures (< 1 K) to achieve spectral holes with measured lifetimes of 30 minutes, and to create good spectral combs. With these spectral combs, we demonstrated for the first time quantum storage in $^{167}Er^{3+}$:Y_2SiO_5 and for the first time quantum storage at telecommunications wavelength in an on-chip resonator.

Another appealing property of $^{167}Er^{3+}$:Y_2SiO_5 is that ZEFOZ hyperfine transitions have been predicted to exist in this material [75, 85]. Because ZEFOZ transitions are first-order insensitive to magnetic field, they could have even longer coherence times. Moreover, the superhyperfine interaction between the erbium electron spin and

neighboring yttrium nuclear spins would be suppressed for these levels. As described in this work, superhyperfine coupling limits the performance of AFC memories by limiting the minimum spectral feature. ZEFOZ transitions in $^{167}Er^{3+}$:Y_2SiO_5 were not explored in this work; we address them again in the Future Directions portion of this thesis.

In addition to ensemble quantum memories, erbium doped crystals can be used for a suite of quantum technologies. There have been proposals [8] and demonstrations [35, 84] using cavity-coupled single erbium ions for quantum technologies, and a proposal for efficient quantum microwave-to-optical transduction using erbium ensembles [107].

1.3 Cavity Quantum Memories Using Nanophotonic Resonators

For ensemble quantum memories, a resonator can be used to achieve high efficiency. Afzelius et al. [3] and Moiseev et al. [80] showed that an ensemble quantum memory can achieve unity efficiency in the impedance matched condition, when the ensemble absorption rate equals the cavity coupling to free space (characterized by an ensemble cooperativity of 1). Since these proposals, optical resonators have been used to improve storage efficiencies to above 50% in rare earth ion doped crystals [56, 76, 89, 93] and cold atoms [10, 106]. Resonators led to higher efficiencies not only for the AFC memory protocol [56, 89], but also for storage using EIT [93, 106], DLCZ [10], and ROSE [76].

This work focuses on integrating rare earth ion ensembles with nano-scale on-chip resonators. In addition to the improvement in memory efficiency, nano- and micro-scale resonators enable miniaturization and on-chip integration. For example, multiple atomic memories on the same chip could be used in an entanglement distillation protocol [20, 40] as part of a quantum network. In this work, we use nanobeam resonators milled directly in $^{167}Er^{3+}$:Y_2SiO_5 [30, 79, 114], and amorphous silicon resonators coupled evanescently to the $^{167}Er^{3+}$ ensemble [78]. The first on-chip cavity quantum memory was demonstrated in our lab in Nd^{3+}:YVO [115]. This work followed that result by achieving on-chip quantum storage at telecommunication wavelengths in a $^{167}Er^{3+}$:Y_2SiO_5 nanophotonic resonator. We note several studies which have used on-chip waveguides for ensemble quantum memories [9, 73, 90, 95].

1.4 Structure of this Thesis

Chapter 2 introduces erbium-167 doped yttrium orthosilicate ($^{167}Er^{3+}$:Y_2SiO_5), the material used throughout this work to store and manipulate light. Methods used to initialize the ions and burn atomic frequency combs are introduced. Superhyperfine coupling is also introduced.

Chapter 3 describes the atomic frequency comb protocol used to store light in this work. The theoretical efficiency of this protocol in a cavity is discussed.

Chapter 4 describes the design and fabrication of on-chip resonators and on-chip electrodes used for storage and control in this work. Two types of resonators are presented: an $^{167}Er^{3+}$:Y_2SiO_5 photonic crystal nanobeam, and a hybrid resonator using amorphous silicon (αSi) waveguides and photonic crystals on $^{167}Er^{3+}$:Y_2SiO_5.

Chapter 5 shows on-chip storage of telecom wavelength light in a nanobeam resonator in $^{167}Er^{3+}$:Y_2SiO_5. The multimode storage capacity and storage fidelity are presented, as are a discussion of storage efficiency and a path toward higher efficiency. This chapter is adapted from Reference [30].

Chapter 6 shows a new multifunctional optical quantum memory using a hybrid αSi-$^{167}Er^{3+}$:Y_2SiO_5 resonator and on-chip electrodes. This device combines AFC storage with DC Stark shift control to dynamically control the memory time, and apply corrections to the frequency and bandwidth of the stored light.

Chapter 7 concludes this thesis. The results are summarized with a focus on the potential of $^{167}Er^{3+}$:Y_2SiO_5 and nanophotonic resonators for efficient quantum memories. Future directions are recommended.

Chapter 2

ERBIUM-167 IN YTTRIUM ORTHOSILICATE

In this chapter, we introduce erbium-167 doped yttrium orthosilicate ($^{167}Er^{3+}$:Y_2SiO_5). We outline its energy structure, with a focus on the telecom optical transitition and hyperfine ground state levels. We present optical coherence measurements at temperatures below 100 mK, and moderate magnetic fields (0.4-1 T), and also measure the hyperfine lifetime under these conditions. We introduce the concept of spectral holeburning, which is used to create atomic frequency combs. The methods used to initialize the ions into a few hyperfine states at the beginning of every experiment are discussed. Finally, we introduce superhyperfine coupling, which is an important limitation to the performance of the AFC protocol in this material.

2.1 System Overview

For a concise introduction to the energy structure of rare earth ions in crystals beyond what is described here, I recommend Chapter 3 in John Bartholomew's thesis [11].

The Hamiltonian describing the energy levels of $^{167}Er^{3+}$:Y_2SiO_5 in an applied magnetic field is:

$$H = H_{\mathrm{FI}} + H_{\mathrm{CF}} + H_{e\mathrm{Z}} + H_{\mathrm{HF}} + H_{n\mathrm{Z}} + H_{\mathrm{SHF}} \tag{2.1}$$

where H_{FI} is the Hamiltonian of a free Er^{3+} ion including spin-orbit coupling, and H_{CF} is the crystal field correction from Y_2SiO_5. For $^{167}Er^{3+}$, the first two energy levels of H_{FI} are $^4I_{\frac{15}{2}}$ and $^4I_{\frac{13}{2}}$, separated by ~ 0.8 eV = 195 THz = 1.5 μm. These levels are $(2J+1)$-fold degenerate. H_{CF} lifts the degeneracy of these levels, splitting each into $J+1/2$ twofold degenerate levels, separated by ~ 5 meV = 40cm^{-1} = 1THz [16]. The lowest two-fold degenerate levels of the $^4I_{15/2}$ and $^4I_{13/2}$ manifolds, called Z_1 and Y_1, respectively, are Zeeman doublets and they behave as spin-1/2 electrons. The optical transition used in this thesis is between the Z_1 and Y_1 states. This transition is very weak, characterized by an oscillator strength of 2×10^{-7} [74]. It is both weakly electric-dipole allowed due to the crystal field and magnetic-dipole allowed [16, 67].

The remaining terms in Equation 2.1 form the spin Hamiltonian for the electron and

nuclear spins. Equations 2.2 to 2.4 and Equation 2.6 in Section 2.4 describe these terms.

H_{eZ} is the electron spin Zeeman Hamiltonian characterizing with an external applied field $\vec{B}$:

$$H_{eZ} = \mu_B \vec{B} \cdot \hat{g} \cdot \vec{S}, \tag{2.2}$$

where $\mu_B = 14.0 GHz/T$ is the Bohr magneton and $\hat{g}$ is the 2$^{\text{nd}}$ rank g-tensor, and S is the electron spin operator. Due to the low symmetry of the Y_2SiO_5 crystal field, the $\hat{g}$ tensor is characterized by 6 independent parameters, which are experimentally determined in Refs. [50, 99]. $\vec{I}$ is the spin operator for the $I = 7/2$ nuclear spin of ^{167}Er ions. ^{167}Er comprises 23% of natural abundance erbium, and the remaining isotopes all have $I = 0$. H_{HF} is the hyperfine Hamiltonian characterizing the interaction between the electron spin and ^{167}Er nuclear spin:

$$H_{\text{HF}} = \vec{I} \cdot \hat{A} \cdot \vec{S} + \vec{I} \cdot \hat{Q} \cdot \vec{I}, \tag{2.3}$$

where $\hat{A}$ and $\hat{Q}$ are also 2$^{\text{nd}}$ rank, experimentally determined tensors [44, 50]. This interaction splits each twofold degenerate electron spin level into 16, with a splitting on the order of 1 GHz. The second term in Eq. 2.3 describes the quadrupole interaction and the second-order hyperfine interaction. H_{nZ} describes the $^{167}Er^{3+}$ nuclear spin Zeeman interaction,

$$H_{nZ} = \mu_n g_{n,Er} \vec{B} \cdot \vec{I}, \tag{2.4}$$

where $\mu_n = 7.62$ MHz/T is the nuclear magneton and $g_{n,Er} = -0.1611$ is the nuclear g-factor of ^{167}Er [98]. This effect leads to a small correction to the energy of the hyperfine levels and usually ignored. The last term of Eq. 2.1, H_{SHF} describes the superhyperfine interaction, as defined in Eq. 2.6 and discussed in Section 2.4.

Figure 2.1 shows a primitive Y_2SiO_5 unit cell, containing 8 yttrium atoms, 4 silicon atoms, and 20 oxygen atoms [1, 70, 81]. The structure of the crystal is based on SiO_4 tetrahedra, YO_6 octahedra, and YO_7 polyhedra [28]. Erbium can substitute for either of two inequivalent yttrium crystallographic sites, nominally with equal probability [16]. Each of these two yttrium sites is repeated four times in the unit cell with different orientations. This leads to four subclasses for each crystallographic

site, related by inversion or C_2 symmetry. For magnetic field interactions, all four subclasses are equivalent if the magnetic field is applied parallel or perpendicular to the crystal symmetry axis (the b axis) [99].

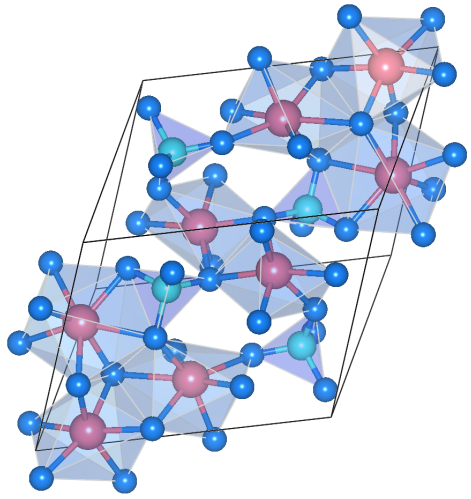

Figure 2.1: Y_2SiO_5 primitive unit cell. Pink spheres represent yttrium atoms; cyan spheres represent silicon atoms; blue spheres represent oxygen atoms. The size of the spheres is meaningless. The translucent blue polyhedra indicate the structure of the crystal (see main text). The unit cell is shown in an arbitrary orientation chosen to highlight the structure.

The crystal field corrections are different for the optical ground and excited states (Z_1 and Y_1), as well as for the two crystallographic sites. The tensors $\hat{g}$, $\hat{A}$, and $\hat{Q}$ must therefore be measured for each crystallographic site in both the ground and excited optical states. Usually, these tensors are measured in a right-handed cartesian coordinate system defined by the optical extinction axes of the crystal, D_1, D_2, and b. b is also the crystal symmetry axis [16].

The simplified energy structure of $^{167}Er^{3+}$:Y_2SiO_5 is shown in Figure 2.2. The energy values are for crystallographic site 2, which has an optical transition at 1539 nm, with a magnetic field applied along the D_1 Y_2SiO_5 axis. The magnitude of the Zeeman interaction $|\vec{B} \cdot \hat{g} \cdot \vec{S}| \sim 210$ GHz/T is maximized for this site and this direction [99]. All experiments in this thesis were performed using this crystallographic site and magnetic field orientation to freeze out the $^{167}Er^{3+}$ electron spin, for reasons described in Section 2.3.

A note about the crystallographic sites in Er^{3+}:Y_2SiO_5: in crystallographic studies, the two sites are labelled as "Y1" and "Y2," where "Y2" is the yttrium site surrounded by 6 oxygen atoms and "Y1" is the yttrium site surrounded by 7 oxygen atoms

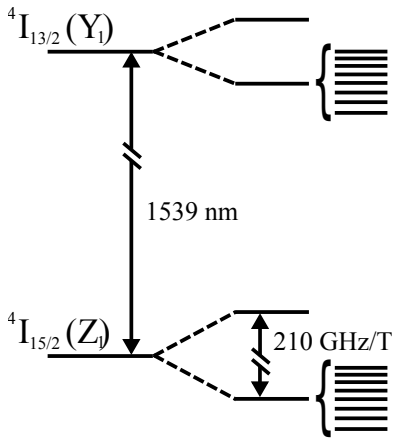

Figure 2.2: Simplified energy diagram for $^{167}Er^{3+}$:Y_2SiO_5 (crystallographic site 2) with a magnetic field applied parallel to the D_1 crystal axis (adapted from Ref. [30]). From left to right, the levels shown are: (i) the spin-orbit levels with crystal field corrections $^4I_{15/2}(Z_1)$ and $^4I_{13/2}(Y_1)$; (ii) the Zeeman split electron spin doublet in an applied magnetic field; (iii) the eight-fold hyperfine splitting on the lowest electron spin level.

[28]. Using spectroscopy and crystal field calculations, Doualan et al. identified the yttrium site surrounded by 6 oxygen atoms as having a $^4I_{15/2}(Z_1)$ to $^4I_{13/2}(Y_1)$ transition at 6507 cm^{-1} (1536.8 nm) and called this "site 1," and they identified the yttrium site surrounded by 7 oxygen atoms as having a $^4I_{15/2}(Z_1)$ to $^4I_{13/2}(Y_1)$ transition at 6497 cm^{-1} (1539.1 nm) and called this "site 2" [37]. This assignment ("site 1" has a transition at $\sim$ 1536.5 nm and "site 2" has a transition at $\sim$ 1539 nm) is the norm in recent spectroscopic studies, for example, References [16, 44, 99]. In short, in Er^{3+}:Y_2SiO_5 literature, site "Y1" is "site 2," and site "Y2" is "site 1."

2.2 Optical Coherence

One of the key advantages of an $^{167}Er^{3+}$:Y_2SiO_5 system is the long coherence time of the optical transition. For all-optical storage protocols such as those discussed in this work, storage time is limited by optical coherence time, and therefore this is an important metric.

In general, rare earth ions in solids have long coherence times due to their unique electronic structure in which the electrons in the partially occupied 4f shell are shielded by the electrons in the 5s and 5p shells [66]. The main source of decoherence is the interactions between phonons in the crystal and the $\sim$ 200 THz transitions which arise from crystal field perturbation on optical transitions. Below 4 K, the phonon distribution peaks below 100 GHz, so phonon processes at 200 THz are

suppressed and optical coherence times can be quite long. For this reason, coherent experiments involving rare earth ions are performed at cryogenic temperatures.

In rare earth ions with unpaired electron spins such as erbium, the interaction between Zeeman levels and phonons can also lead to decoherence in hyperfine and optical transitions. If the phonon distribution at 4 K is peaked at $\sim$ 50 GHz and the $^{167}Er^{3+}$:Y_2SiO_5 electron Zeeman splitting is 210 GHz/T (see Figure 2.2), then magnetic fields must be much higher than 250 mT, and/or the crystal temperature must be much lower than 4 K, in order to freeze out the electron spin and eliminate spin-lattice relaxation as a source of decoherence. For example, Böttger et al. measured optical coherences times of up to 4.38 ms in Er^{3+}:Y_2SiO_5 at 7 T and 1.5 K [19]. Rančić et al. measured highly coherent hyperfine transitions in $^{167}Er^{3+}$:Y_2SiO_5 at 7 T and 1.4 K [86].

Beyond interactions with phonons, there exist two additional mechanisms affecting coherence times in $^{167}Er^{3+}$:Y_2SiO_5, both related to magnetic field noise [17]. The first is magnetic field noise induced by spin flip-flops between $^{167}Er^{3+}$ electron spins. Since these flip-flops are energy preserving, they persist even at low temperatures, unless the electron spins are frozen using a combination of high magnetic field and low temperatures. The spin flip-flop rate is highly dependent on $^{167}Er^{3+}$ doping concentration [17, 25]. For this reason, we use dilute $^{167}Er^{3+}$ doping of 50 or 200 ppm. The second decoherence mechanism is magnetic field noise due to electronic and nuclear spin flips in other species. This can include other inadvertent rare earth ion dopants or the nuclear spins in Y_2SiO_5 itself. Yttrium nuclei are 100% spin-$1/2$, silicon nuclei are 4.7% spin-$1/2$, and oxygen nuclei are 0.04% spin-$5/2$, where the percentages represent relative isotopic abundance. The nuclear spins have very low energy transitions, and cannot be frozen at reasonable magnetic fields and temperatures. Nuclear spin flips are therefore the limit to coherence times in a bulk $^{167}Er^{3+}$:Y_2SiO_5 crystal [17, 86].

In this work, we use moderate magnetic fields ($<$ 1 T) and dilution refrigerator temperatures ($<$ 100 mK) to freeze the $^{167}Er^{3+}$ electron spin. We thus achieve long optical coherence times, as well as long hyperfine lifetimes (see Section 2.3). Figures 2.3 and 2.4 show two-pulse photon echo measurements [2] of the optical coherence time of site 2 in $^{167}Er^{3+}$:Y_2SiO_5, in bulk and in nanophotonic devices.

Figure 2.3 shows optical coherence measurements in bulk $^{167}Er^{3+}$:Y_2SiO_5 and in the nanobeam device used in the experiments in Chapter 5. A magnetic field of 380 mT was applied parallel to the D_1 optical axis. The $^{167}Er^{3+}$ concentration was nominally

50 ppm, although it was measured by secondary ion mass spectrometry to be 37 ppm. The optical coherence time was measured to be $T_2 = 4 \times \tau(1/e) = 759 \pm 41\,\mu$s in bulk at 35 mK. The coherence time of the ions coupled to the nanobeam cavity was $149 \pm 4\,\mu$s, about 1/4 the coherence time of the bulk ions at the same dilution refrigerator temperature. This is due in part to the elevated temperature in the nanobeam compared to bulk, which was measured to be 317 mK (see Section 5.6). The coherence time of the bulk ions at 1 K was found to have a similar value of $136 \pm 9\,\mu$s. Ions coupled to the nanobeam are also closer to the surface, where coherence times can be lower due to surface charge fluctuations [12]. It is also possible that the fabrication process caused disorder that affected the coherence time of the ions. Rare-earth ions coupled to similar nanobeam resonators have been shown to have coherence times similar to the bulk [113, 115], however, the longer bulk coherence times measured in the current work allow a much more sensitive probe of the ions' environment.

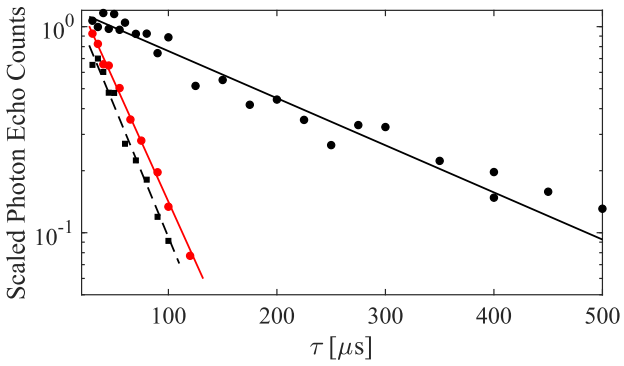

Figure 2.3: Optical coherence time measurement in nanobeam resonator and bulk $^{167}Er^{3+}$:Y_2SiO_5. Two-pulse photon echo counts versus inter-pulse time delay with exponential fits; the vertical axis is scaled for clarity. Measurements in the bulk $^{167}Er^{3+}$:Y_2SiO_5 crystal at 35 mK (black circles and solid black line fit), in bulk at 940 mK (black squares and dashed black line fit), and in the nanobeam at 42 mK (red circles and solid red line fit). Temperatures were measured at the dilution refrigerator stage to which the sample was thermally connected.

Figure 2.4 shows a similar experiment in bulk $^{167}Er^{3+}$:Y_2SiO_5 and in the hybrid resonator based on amorphous silicon resonators on $^{167}Er^{3+}$:Y_2SiO_5 (αSi-$^{167}Er^{3+}$:Y_2SiO_5) used in Chapter 6. The nominal $^{167}Er^{3+}$ concentration was 200 ppm, although it was measured by secondary ion mass spectrometry to be 135 ppm. A magnetic field of 980 mT was applied parallel to the D_1 optical axis. The higher magnetic field was used to suppress erbium electron flip-flops at this higher concentration. In the bulk $^{167}Er^{3+}$:Y_2SiO_5 crystal, the optical coherence time was

measured to be $T_2 = 1.11 \pm 0.15$ ms. In the hybrid αSi-$^{167}Er^{3+}$:Y_2SiO_5 resonator we measured $T_2 = 108 \pm 13\,\mu$s. The similarity between this T_2 value and the one for the nanobeam resonator in Fig. 2.3 suggests that proximity to the surface might play an important factor, since the bulk crystal T_2 values and fabrication processes were different for the two resonators. The hybrid αSi-$^{167}Er^{3+}$:Y_2SiO_5 resonator was surrounded by electrodes (see Section 4.3). Applying equal and opposite square pulses to the electrodes between the first and second optical pulses did not significantly affect the measured optical coherence time, indicating that electric pulses were not a source of optical decoherence.

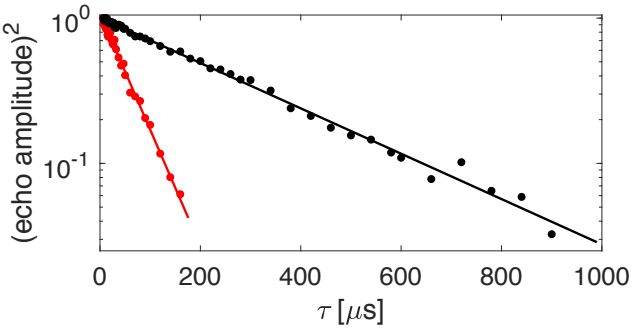

Figure 2.4: Optical coherence time measurement in hybrid αSi-$^{167}Er^{3+}$:Y_2SiO_5 resonator and bulk $^{167}Er^{3+}$:Y_2SiO_5. Two-pulse photon echo energy versus inter-pulse time delay with exponential fits. Measurements in the bulk $^{167}Er^{3+}$:Y_2SiO_5 crystal at 71 mK (black circles and solid black line fit) and in the hybrid resonator at 90 mK (red circles and solid red fit). For the resonator measurement, the data is scaled photon counts, measured on an SNSPD. The bulk data was measured using a heterodyne setup (see Appendix D), and the signal was squared to match the resonator data, then scaled. Temperatures were measured at the dilution refrigerator stage to which the sample was thermally connected.

2.3 Spectral Holeburning, Hyperfine Levels, and Initialization

In order to implement the atomic frequency comb protocol, the $^{167}Er^{3+}$:Y_2SiO_5 ions must be initialized into a long-lived frequency comb. Atomic frequency combs are atomic absorption profiles which contain transparent (non-absorbing) gaps, called spectral holes. Creating these long-lived spectral features requires long hyperfine state lifetimes, which are observed in $^{167}Er^{3+}$:Y_2SiO_5 at low temperatures and moderate magnetic fields.

Spectral Holeburning

Spectral holeburning occurs in systems with optical transitions and long-lived states in the optical ground state manifold. To create a spectral hole, it is simply required to move population from one long-lived state to another. In the case of $^{167}Er^{3+}$:Y_2SiO_5, the long-lived states are hyperfine states. Figure 2.5 shows a simple schematic of holeburning in a 4-level system (2 ground states and 2 excited states). We assume that the two ground-state levels start with equal population. In the case of an ensemble, population can be interpreted as number of ions in each state. Pumping on the "h" transition with a laser leads to population moving to the excited state and eventually falling to the other ground state. This depletes the lowest ground state of population, leaving behind a spectral hole "h" when the absorption spectrum (optical depth vs. frequency) of the 4-level system is probed. The spectrum will also show a side-hole "s" corresponding to the transition from the depleted ground state to the other excited state. The other ground state level has more population than normal, so the transitions connecting the upper ground state level to the two excited states will be more absorbing, leading to two anti-holes "a_1" and "a_2."

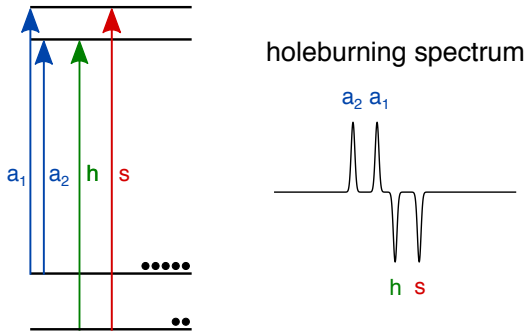

Figure 2.5: Spectral holeburning schematic. Left hand side shows a 4-level energy diagram. Black circles represent ion population. Arrows show transitions corresponding to a spectral hole "h," a side-hole "s," and two anti-holes "a_1" and "a_2". On the right hand side is a representation of an absorption spectrum after holeburning, with less absorption in the hole and side-hole, and more absorption in the anti-holes.

Figure 2.5 shows the hole, side-hole and anti-holes that form as a result of population moving between ground state levels. There are other types of side-holes called transient holes, which can be observed a short time after a laser pulse has been used to burn a spectral hole, before population has had time to decay from the optical excited states ($t < T_1$, where T_1 is the optical lifetime). In the experiments presented in this work, we wait tens of milliseconds ($t > 3 \times T_1$) after spectral holeburning to

make sure that all population has decayed from the excited state to one of the ground states, so transient holes do not play a role in our spectra.

In rare-earth ion doped crystals, the absorption spectrum of optical transitions can be quite broad, on the order of tens of megahertz to gigahertz. This inhomogeneous broadening is a result of the slightly different crystal environment that each ion experiences. Variance in the radii of different isotopes, mismatch between the radii of the dopant and host, crystal defects, and strain on a crystal can all increase the inhomogeneous broadening [18]. In $^{167}Er^{3+}$:Y_2SiO_5, we measured the inhomogeneous broadening to be 150 - 350 MHz.

Figure 2.6 shows the theoretical holeburning spectrum in an inhomogeneously broadened system. A particular laser frequency "h" will not match the same transition for each ion. Rather, for a four-level system, there are four sets of ions (four energy level combinations), which have one transition with frequency "h." Set 1 is the same as in Fig. 2.5. Sets 2 - 4 all have a spectral hole at frequency "h," but the frequencies of their side-hole and anti-holes are all different, as shown in the spectra under the level diagrams. When the inhomogeneous linewidth is greater than the energy splittings in the ground and excited states, all four sets of ions are present in the inhomogeneous line, and the spectrum will look like the top image in Figure 2.6. In this case, the holeburning spectrum will always be symmetric about the hole.

The schematic shown in Fig. 2.6 is shown with 4 levels for simplicity. In general if the inhomogeneous broadening is larger than the frequency span of all ground states and the span of all excited states, each spectral hole creates $n_e - 1$ side-holes and $(n_g - 1) \times n_e$ anti-holes, where n_e (n_g) is the number of excited (ground) state energy levels.

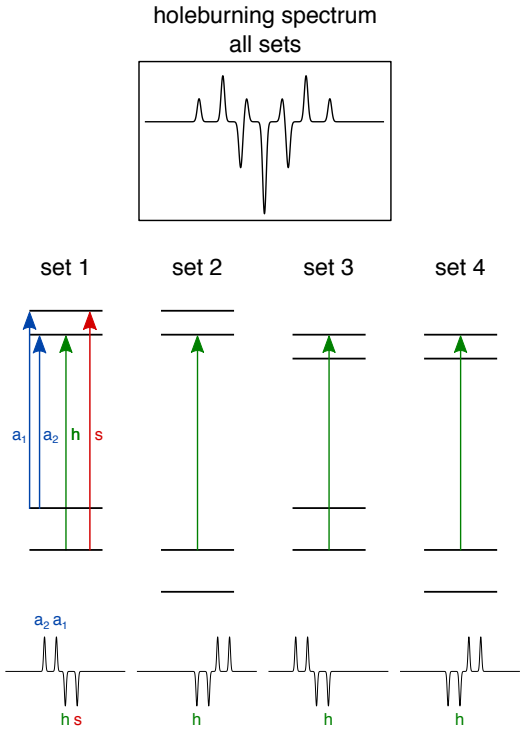

Figure 2.6: Spectral holeburning in an inhomogeneous distribution. Top figure shows the holeburning spectrum in an inhomogeneously broadened ensemble of ions. The central feature is the spectral hole, and there are also 2 side-holes and 6 anti-holes. Below the spectrum are four level diagrams showing the four sets of ions in the ensemble which have one transition at frequency "h." Arrows show transitions corresponding to a spectral hole "h," a side-hole "s," and two anti-holes "a_1" and "a_2." Each of these sets has a distinct side structure (side-holes and anti-holes) shown below the level diagrams. These spectra add up to create the observed holeburning spectrum at the top of the figure.

Hyperfine State Lifetime

In order for spectral holes to be deep and long lived, the lifetime of the ground state levels must be much larger than the optical lifetime [46, 62]. In $^{167}Er^{3+}$:Y_2SiO_5, this is possible when the ground state levels are hyperfine levels. The optical transition lifetime is 9 ms [16]. Rančić et al. measured spectral holes in $^{167}Er^{3+}$:Y_2SiO_5 with lifetimes larger than 1 minute at 3 T and 1.4 K [86]. They attributed these long lived holes to long hyperfine state lifetimes, and found that the hyperfine state lifetimes were limited by electron spin flips. If the electron spin is frozen using a combination of high magnetic field and low temperatures, the hyperfine lifetime is sufficient to allow long-lived spectral features. In this work, we use dilution refrigerator temperatures ($<$ 100 mK) and moderate magnetic fields ($<$ 1 T) to

freeze the electron spin.

Figure 2.7 shows a scan of the inhomogeneously broadened $^{167}Er^{3+}$:Y_2SiO_5 absorption line (black curve) in a bulk crystal with 50 ppm $^{167}Er^{3+}$ doping concentration (site 2). A magnetic field of 380 mT was applied parallel to the D_1 crystal axis. The sample was thermally connected to the dilution refrigerator plate at $\sim$ 25 mK. Transitions between individual hyperfine levels (in the lower electron spin branch) in the optical ground and excited state manifolds are partially resolved. There is likely some splitting of inequivalent magnetic subclasses due to a misalignment of the magnetic field and the D_1 crystal axis (see Section 2.1), contributing to the complex shape of the spectrum. A wide spectral transparency (trench) was created in this absorption line by optical pumping: a laser was scanned slowly and repeatedly over a 140 MHz band, which depleted those hyperfine levels with resonant optical transitions. The population was then allowed to return to its equilibrium distribution while measuring transmission using a room temperature InGaAs photodiode. Scanning the line to probe the hole depth likely led to an underestimation of T_1 by redistributing population, but this effect was minimized by using low scan power. The width of the trench was chosen to minimize effects of spectral diffusion on the T_1 measurement. The depth of the spectral feature, or hole depth d, is a measure of how much population is missing from the hyperfine levels that were optically pumped:

$$d(t) = \frac{\text{optical depth}(t \rightarrow \infty) - \text{optical depth}(t)}{\text{optical depth}(t \rightarrow \infty)}. \tag{2.5}$$

The maximum $d(t = 0)$ achieved here was 0.9. This was in part due to a noisy background from detector noise and Fabry-Perot resonances in the setup, which made it difficult to accurately measure the depth of the hole. It is also possible that hole depth is limited by the $^{167}Er^{3+}$ isotopic purity.

Figure 2.7b shows the decay in time of the hole depth $d(t)$ as measured in the center of the trench. The fast decay is fit to an exponential with a lifetime of 29 min, while the slow decay is fit to a lifetime of 6 hours. Following Reference [86], we interpret these lifetimes as a two-step change in the spectrum: first, the trench fills in due to spin-spin interactions between $^{167}Er^{3+}$ electron spins, then, at a slower rate, the population is redistributed among hyperfine levels due to electron spin-lattice relaxation.

For spectral holeburning memories, it is also important that spectral diffusion be

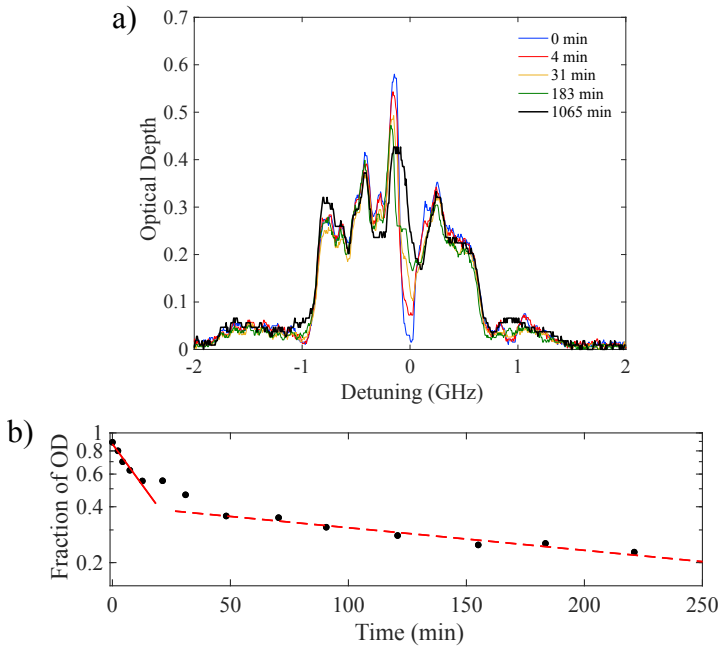

Figure 2.7: $^{167}Er^{3+}$:Y_2SiO_5 spectral hole lifetime. b) Inhomogeneous $^{167}Er^{3+}$:Y_2SiO_5 line showing the hyperfine structure and a spectral trench at 0 GHz detuning, shown as a function of time after trench creation. The detuning is measured from 194814 GHz ± 1 GHz. c) Depth of trench measured as a fraction of optical depth vs. time (black circles) and fits to two exponential curves (red lines).

small, since it leads to washing out of spectral features over time. Böttger et al. characterized the spectral diffusion for Er^{3+}:Y_2SiO_5 at various magnetic fields and temperatures in Reference [17]. We found that below 1 K and at a magnetic field of 380 mT applied parallel to the D_1 axis, the spectal diffusion was small but not insignificant. With a three pulse photon echo measurement in the nanobeam resonator device (Section 4.1) we estimated the increase to optical linewidth due to spectral diffusion to be $\sim$ 130 kHz/s.

Hyperfine Initialization

Due to the hyperfine splitting in $^{167}Er^{3+}$:Y_2SiO_5, the linewidth of the absorption feature at 1539 nm is broadened from the inhomogeneous linewidth of a single optical transition ($\sim$ 150 MHz) to $\sim$ 1.5 GHz, since the optical transitions from the various hyperfine levels in the ground state to the various hyperfine levels in the excited state occur at different frequencies (see Figure 2.2). Because of this, the optical depth in the center of the line is decreased relative to an otherwise identical Er^{3+}:Y_2SiO_5 sample using an erbium isotope with zero nuclear spin. Moving population into fewer hyperfine states can increase this optical depth.

At high magnetic fields, where the electron spin Zeeman term is very large compared to the hyperfine term, the hyperfine levels can be approximately labelled with $|m_s, m_I\rangle$ quantum numbers (see Figure 2.9b). The quantization axis for the nuclear spin in this case is the electron spin dipole moment. Since the $\hat{g}$ tensors of the optical ground and excited states are different, the electron spin dipole moment in the optical excited state is different from that in the ground state. Because the quantization axes for the nuclear spin are different, not only are optical transitions of the type $|m_s = -\frac{1}{2}, m_I = -\frac{7}{2}\rangle_{\text{ground}}$ to $|m_s = -\frac{1}{2}, m_I = -\frac{7}{2}\rangle_{\text{excited}}$ allowed, but $|m_s = -\frac{1}{2}, m_I = -\frac{7}{2}\rangle_{\text{ground}}$ to $|m_s = -\frac{1}{2}, m_I = -\frac{5}{2}\rangle_{\text{excited}}$ transitions are also allowed, although they are weaker. In what follows, we refer to transitions of the former type as $\Delta m_I = 0$ transitions and the latter type as $\Delta m_I = +1$. Since we always use the lower electron spin levels ($m_s = -\frac{1}{2}$) in both the optical ground and excited state, we will drop the m_s label.

At high magnetic fields, the entire optical ground state population can be initialized into one hyperfine state by pumping on all $\Delta m_I = +1$ or all $\Delta m_I = -1$ transitions, as done by Rančić et al. [86]. The idea is that by pumping on all $\Delta m_I = +1$ transitions, all ions end up in the $m_I = |+\frac{7}{2}\rangle$ ground state level, since there is no $\Delta m_I = +1$ transition for that ground state level. Similarly, pumping on the $\Delta m_I = -1$ transition should initialize the ions into the $m_I = |-\frac{7}{2}\rangle$ ground state level. At 380 mT applied parallel to the D_1 axis, only a partial initialization can be performed because the $\Delta m_I = \pm 1$ optical transitions are not fully resolved from the $\Delta m_I = 0$ optical transitions.

Figure 2.8 shows the $^{167}Er^{3+}$:Y_2SiO_5 1539 nm transition in a bulk crystal, both with and without initialization, always with a spectral comb created in the center. Initialization was performed by turning on strong sidebands of an EOM modulator and sweeping their detuning over a range of ±(0.37 GHz – 0.82 GHz). This was the full range of the voltage controlled oscillator used to sweep the sidebands. Both 1$^{\text{st}}$ order sidebands were used in the initialization procedure, and the amplitude of the 0$^{\text{th}}$ order sideband was minimized by using strong RF drive power. This procedure was used at the beginning of every atomic frequency comb storage experiment in Chapter 5. A pulse sequence schematic is shown in Fig. 5.2. We think this procedure moved population from the higher and lower energy hyperfine states to the middle few hyperfine states. However, we did not identify the frequencies of the various optical transitions, so this is not a conclusive assignment. Additionally, there may be some splitting of inequivalent magnetic subclasses due to a misalignment of the magnetic

field and the D_1 crystal axis. This would lead to a more complicated spectrum. The optical depth was improved by a factor of ~ 3 compared to the uninitialized case. Sweeping one sideband to pump on only one side of the inhomogeneous line produced a similar enhancement in optical depth.

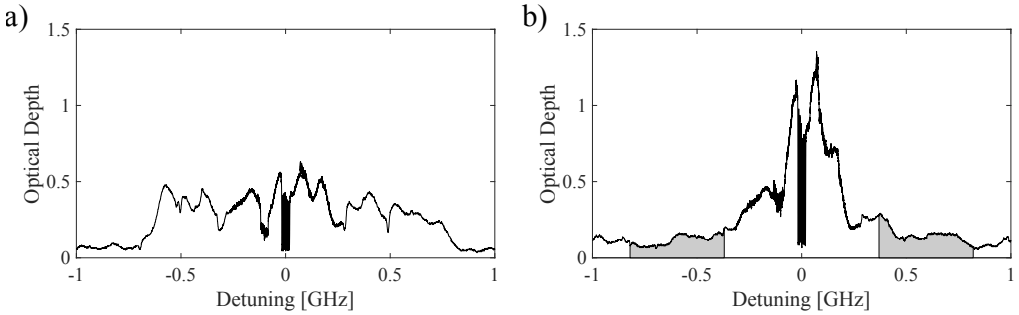

Figure 2.8: $^{167}Er^{3+}$:Y_2SiO_5 hyperfine initialization and comb burning in 50 ppm $^{167}Er^{3+}$:Y_2SiO_5 sample. Absorption spectrum of the inhomogeneous line in bulk $^{167}Er^{3+}$:Y_2SiO_5 at 18 mK and 380 mT (parallel to D_1) with 40 MHz wide comb created in the center. a) Without initialization, the peak optical depth of comb is 0.4. b) With initialization into a few hyperfine states before comb creation, the peak optical depth of comb is 0.9. Gray area shows the extent of the sweep of the EOM sidebands during the initialization step. The detuning was measured from 194814 GHz ± 1 GHz.

Figure 2.9 shows a similar hyperfine initialization procedure in the 200 ppm $^{167}Er^{3+}$:Y_2SiO_5 sample used in experiments in Chapter 6. The sample was at 70 mK (measured at the dilution refrigerator plate) with an applied field of 980 mT parallel to D_1. In this case, the magnetic field along the b axis was cancelled using trim coils, so the spectra of the two magnetically inequivalent subclasses are overlapping. Figure 2.9b shows the predicted splittings between the lowest 8 hyperfine levels at this field (see Figure 2.2 for a schematic of the other energy levels in the system).

Before any initialization, the red curve in Fig. 2.9a shows 3 broad peaks, which we think belong to sets of transitions with $\Delta m_I = -1$, 0, and 1. These sets of transitions are not fully resolved, even at a field close to 1 T. Rančić et al. found that these transitions were fully resolved at 7 T, and used this to perform highly efficient initialization into only one hyperfine state [86]. For the initialization shown in Fig. 2.9a, the laser frequency was swept back and forth using its piezo drive in the region shown by the green area for 100 ms. By pumping in the range of the $\Delta m_I = -1$ transitions, most ions were pumped into the lowest energy hyperfine state $m = |-\frac{7}{2}\rangle$, which has a $\Delta m_I = 0$ transition on the left side of the central peak at high fields

[86]. However, since the $\Delta m_I = -1$ and 0 transitions are not fully resolved, this initialization was only partly effective.

For the experiments in Chapter 6, the initialization procedure was closer to that shown in Figure 2.8. A fast EOM (10 GHz) was driven around 6 GHz using a VCO. $\sim$ 650 MHz wide trenches were burned on either side of the atomic frequency comb ($\sim$ 70 MHz away from the comb edge), which was toward the right hand side of the absorption profile. We think that the higher frequency trench was pumping on the $\Delta m_I = +1$ transition, which put most of the population to the highest energy hyperfine level $m = |+\frac{7}{2}\rangle$, with its $\Delta m_I = 0$ on the right hand side of the central peak. The lower frequency trench was added after experimentally determining that it improved the AFC storage efficiency. We think this trench was burning population out of lower hyperfine levels through $\Delta m_I = 0$ transitions. This would lead to more efficient initialization into the higher energy hyperfine level because the $\Delta m_I = 0$ transitions are stronger than $\Delta m_I = +1$ transitions.

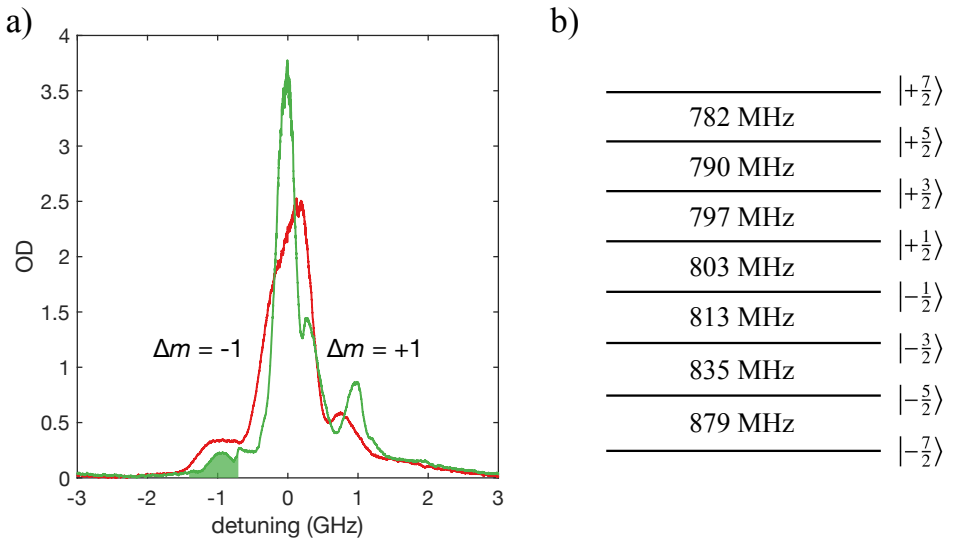

Figure 2.9: $^{167}Er^{3+}$:Y_2SiO_5 hyperfine initialization in 200 ppm sample. a) Red curve shows absorption spectrum (optical depth) of the inhomogeneous line in bulk $^{167}Er^{3+}$:Y_2SiO_5. Green curve shows the same spectrum, but initialized into a few hyperfine states. Green shaded area shows frequency range of laser burning for initialization. The detuning was measured from 194823 GHz ± 1 GHz. b) Lowest 8 hyperfine levels ($m_s = -\frac{1}{2}$) showing splittings for site 2 with a field of 980 mT parallel to D_1, predicted with g, A, and Q tensors from [27].

2.4 Superhyperfine Broadening

In Y_2SiO_5, yttrium atoms are a source of nuclear spin interactions and magnetic noise in this material. There is only one stable isotope of yttrium, ^{89}Y, which has nuclear spin number $s = 1/2$. The unpaired Er^{3+} electron has a large magnetic dipole moment $\mu_e \sim g\frac{\mu_B}{\hbar}$ characterized by a large Landé factor $g \sim 15$. This creates a "frozen core" effect in Er^{3+}:Y_2SiO_5, where the nuclear transition frequencies of nearby yttrium atoms are modified by the Er^{3+} electron spin [45]. This is called a superhyperfine interaction (cf. the hyperfine interaction, which describes the interaction of an atom's electron spin with its *own* nuclear spin). Due to the low symmetry of the Y_2SiO_5 crystal, the magnetic field generated by the electron spin dipole moment is highly anisotropic, characterized by a 2^{nd} rank tensor $\hat{g}$ [99]. This leads to a number of inequivalent electron-nuclear interactions between an erbium ion and its yttrium neighbors [24]. In this section, we look at the effect of these interactions on the holeburning spectra in $^{167}Er^{3+}$:Y_2SiO_5.

Figure 2.10a shows a part of the Y_2SiO_5 unit cell with an erbium ion substituting for a yttrium atom. The four closest yttrium atoms are 3.4 Å to 3.7 Å away from the Er^{3+} atom. The superhyperfine Hamiltonian is a sum of nuclear Zeeman and dipole-dipole interactions [24]:

$$H_{\text{SHF}} = \sum_{i}^{N_Y} -\vec{\mu}_Y^{(i)} \cdot \vec{B} - \frac{\mu_0}{4\pi r^3}\left(\vec{\mu}_Y^{(i)} \cdot \vec{\mu}_e + 3(\hat{r} \cdot \vec{\mu}_Y^{(i)})(\hat{r} \cdot \vec{\mu}_e)\right), \tag{2.6}$$

where N_Y is the number of yttrium atoms being considered, μ_0 is the vacuum permeability, $\vec{\mu}_Y = \mu_n g_{n,Y}\vec{I}$ is the yttrium nuclear spin dipole moment, and $\vec{\mu}_e = \mu_B \hat{g_{e,Er}} \cdot \vec{S}$ is the erbium electron spin dipole moment. $\mu_n = 7.62$ MHz/T is the nuclear magneton, $\mu_B = 14.0$ GHz/T is the Bohr magneton, $g_{n,Y} = -0.2748$ is the yttrium nuclear spin g-factor [98], and $g_{e,Er}$ is the 2^{nd} rank magnetic g-tensor for the Er^{3+}:YSO electron spin, measured for both ground (Z_1) and excited (Y_1) optical states in Reference [99]. For the spin-$1/2$ yttrium nuclear spin and the effective spin-$1/2$ erbium electron spin, $\vec{I} = \vec{S} = \frac{\hbar}{2}\{\sigma_x, \sigma_y, \sigma_z\}$, where σ_i are the Pauli matrices.

Each neighboring yttrium atom splits the energy levels of the Er^{3+} electron spin in two. For large magnetic fields, this splitting is dominated by the nuclear Zeeman term $\mu_Y B = 2.1$ MHz/T. For small magnetic fields, this is dominated by the dipole-dipole interaction, which is on the order of ~ 0.3 MHz and is different for each yttrium atom due to the low symmetry of the crystal. If we consider the closest

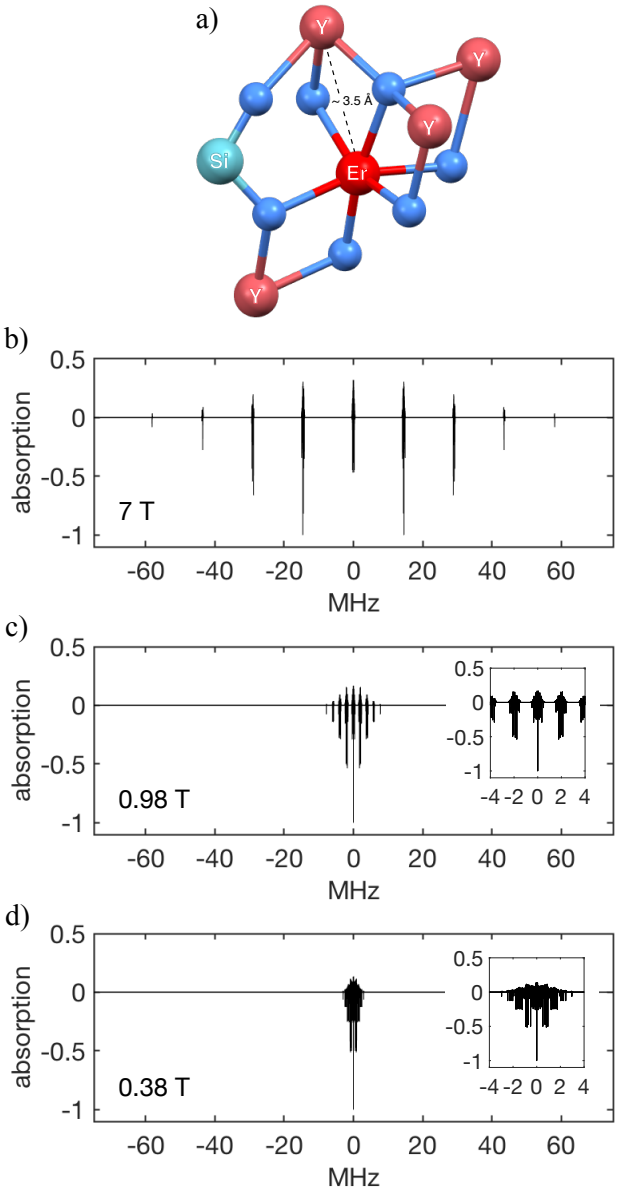

Figure 2.10: Superhyperfine side structure in Er^{3+}:Y_2SiO_5 holeburning. a) Part of the Y_2SiO_5 unit cell with an erbium ion substituting for a yttrium atom. Blue spheres represent oxygen atoms. b)-d) anti-holes and side-holes created when a spectral hole is burned at 0 MHz detuning for various magnetic fields applied parallel to the D_1 crystal axis for a site 2 Er^{3+}:Y_2SiO_5 ion. y-axis shows optical depth in arbitrary units. Insets show a closeup of structure around 0 MHz. b) $B = 7$ T c) $B = 0.98$ T, the magnetic field applied in Chapter 6 experiments. d) c) $B = 0.38$ T, the magnetic field applied in Chapter 5 experiments.

four yttrium atoms, each electron spin level is split into $2^4 = 16$ levels. If we look at electron-spin-preserving optical transitions, this splitting leads to $16 \times 16 = 256$

transitions.

When a spectral hole is burned in $^{167}Er^{3+}$:Y_2SiO_5, these numerous transitions lead to a large number of side-holes and anti-holes. As discussed in Section 2.3, if the inhomogeneous broadening is larger than the frequency span of all ground states and of all excited states, each spectral hole creates $n_e - 1$ side-holes, and $(n_g - 1) \times n_e$ anti-holes, where n_e (n_g) is the number of excited (ground) states.

Figures 2.10b-d show the superhyperfine side hole structure that is expected when a 10 kHz wide hole is burned at zero detuning, considering only the 4 nearest yttrium spins for a site 2 Er^{3+}:Y_2SiO_5 ion. For this calculation, the superhyperfine energy levels in the optical ground and excited states were computed by diagonalizing $H = H_{eZ} + H_{SHF}$ from Equations 2.2 and 2.6. Only transitions connecting the $m_s = -\frac{1}{2}$ electron spin states in the ground and excited optical manifolds were considered. The relative amplitudes of the hole, each side-hole and each anti-hole were estimated using $|\langle\psi_e|\psi_g\rangle|^2$, where ψ_g and ψ_e are the ground and excited states from which that spectral feature resulted. The assumption is made that the population burned away from the hole is evenly distributed among the remaining 15 ground state superhyperfine levels. For this calculation, the $^{167}Er^{3+}$ nuclear spin was not considered. The electron spin dipole $\langle\vec{\mu}_e\rangle$ is modified through the hyperfine interaction with the $^{167}Er^{3+}$ nuclear spin. However, for fields as low as 380 mT (parallel to the D_1 crystal axis), the hyperfine interaction $\sim$ 1 GHz is much smaller than the electron Zeeman interaction $\sim$ 210 GHz/T, so including the hyperfine interation is not expected to have a qualitative effect on the results in Fig. 2.10.

As expected, at high magnetic fields, the side structure is dominated by the nuclear Zeeman term $\mu_Y B$ = 2.1 MHz/T. However, at low to medium magnetic fields, the Zeeman and dipole-dipole terms are comparable, leading to a forest of side-holes and anti-holes that lead to an effective hole broadening. At 380 mT, for example, the entire spectral feature has an effective linewidth of $\sim$ 2 MHz.

Chapter 3

ATOMIC FREQUENCY COMB STORAGE - THEORY

This chapter describes the atomic frequency comb protocol used to store light in this work [4]. After introducing the protocol, we present the theoretical efficiency of storage using the AFC protocol and an ensemble of ions in a cavity [3]. When the ensemble cooperativity is 1 and the cavity is one-sided, known as the impedance-matched condition, this protocol can have an efficiency of 100%.

3.1 Storing Light in an Atomic Frequency Comb

When a photon is absorbed by an ensemble of ions, the excitation is distributed among the ions, creating an entangled Dicke state $|\Psi\rangle$, as shown in Equation 3.1 [4]:

$$|\Psi\rangle = \sum_{j=1}^{N} c_j \, e^{i\omega_j t} \, e^{-ik\vec{r}_j} \left|0...1_j...0_N\right\rangle . \tag{3.1}$$

Each ket in the sum represents one ion absorbing the optical pulse and being promoted to the excited state $|1\rangle$, and the rest of the ions remaining in the ground state $|0\rangle$. Each ion has a position in the crystal $\vec{r}_j$ and an optical transition frequency ω_j. Due to inhomogeneous broadening, the state $|\Psi\rangle$ rapidly dephases as each ion accumulates a different phase $\phi_j = \omega_j t$.

Figure 3.1 presents this dephasing by representing each term in the sum in equation 3.1 as a vector on the equator of the Bloch sphere. Shortly after absorption, at time $t \sim \epsilon$, the different terms of the sum dephase. By $t \sim \frac{1}{\Delta_{\text{inhom}}}$, where Δ_{inhom} is the linewidth of the inhomogeneously broadened distribution, the ions are mostly dephased. The coherence can be restored by reversing the phase evolution, for example by sending in an optical π pulse as in two pulse photon echo [2]. However, this will also create population inversion in the case of a weak input pulse, which leads to amplification and therefore cannot be used for quantum storage [88]. If no additional rephasing pulses are sent in, the energy will leave the system as incoherent photoluminescence.

The atomic frequency comb storage protocol works by limiting which frequencies ω_j ions are allowed to posses. Specifically, in an ideal comb, the ions can only have

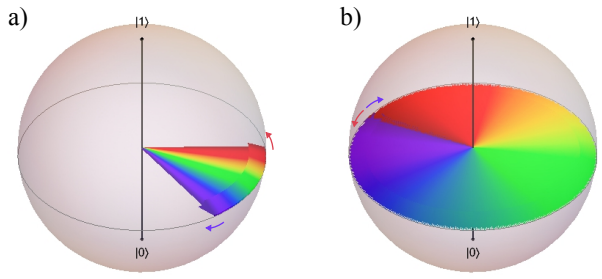

Figure 3.1: Schematic of dephasing due to inhomogeneous broadening on a Bloch sphere. a) Dephasing a short time after absorption. b) Dephasing at $t \sim \frac{1}{\Delta_{\text{inhom}}}$. Details in main text.

frequencies that are multiples of the comb period Δ:

$$\omega_j = 2\pi\Delta\, n_j, \;\; n_j \in \mathbb{Z}. \tag{3.2}$$

In that case, the Dicke state $|\Psi\rangle$ characterizing the ion ensemble after a photon is absorbed is given by Equation 3.3:

$$|\Psi\rangle = \sum_{j=1}^{N} c_j\, e^{i2\pi\Delta\, n_j\, t}\, e^{-ik\vec{r}_j}\, \left|0...1_j...0_N\right\rangle \tag{3.3}$$

Looking at the phase evolution term, when $\Delta \times t = m$ where m is an integer, the term is equal to $e^{i2\pi m\, n_j} = 1$ for all ions, indicating a rephasing event. This means that a chain of rephasing events will occur at $t = \frac{m}{\Delta}$, $m = 1, 2, 3...$ where $t = 0$ is the time when the photon was absorbed.

Figure 3.2 presents the dephasing and first rephasing of a photon absorbed by an atomic frequency comb (AFC). Each term in the sum in Equation 3.3 is represented as an arrow on the Bloch sphere. The inset shows a sketch of an AFC with 5 teeth. Each tooth is not an ideal delta function, but rather a distribution of frequencies, as in a realistic AFC. Immediately after the photon is absorbed, the ions start to dephase, but the phase evolution is described by just 5 groups, one for each comb tooth. At $t = \frac{1}{4\Delta}$, the phases of the 5 groups are maximally scrambled, but the phase evolution continues. By $t = \frac{1}{\Delta} - \epsilon$, all groups are close to arriving at the same phase again: the phase of one group of ions (green) has stayed put, two groups (cyan and orange) have evolved by $\phi = \pm 2\pi$, and two groups (red and purple) have evolved

by $\phi = \pm 2 \times 2\pi$, and all groups are rephasing. When all arrows point in the same direction again at $t = \frac{1}{\Delta}$, the ions will spontaneously emit a photon that is identical in frequency, polarization, and spatial distribution to the one that was absorbed at $t = 0$. This is the output pulse of the AFC memory. Note that the groups of arrows are now broader than when they started. This results from the finite width γ of the comb, and leads to a limit on the efficiency of storage through the term η_d [4] (see Section 3.2).

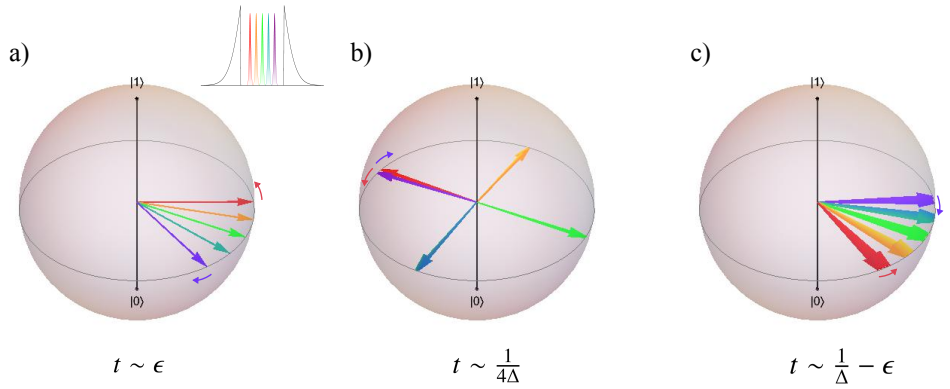

Figure 3.2: Sketch of atomic frequency comb evolution on a Bloch sphere. a) Dephasing a short time after absorption ($t = \epsilon$). Inset shows a schematic of an atomic frequency comb (optical depth versus frequency). (b) Dephasing at $t = \frac{1}{4\Delta}$. c) Shortly before rephasing, at $t = \frac{1}{\Delta} - \epsilon$. The diagram is in the rotating frame of the ions in the center of the comb (green). Details in main text.

Although the AFC protocol can in principle store any kind of photonic qubit, qubits encoded in the polarization degree of freedom of light are not compatible with our implementation. This is because the photonic crystal cavities only support one polarization of light. In this work, we store time-bin qubits for the form $|\psi_{\text{in}}\rangle = \alpha|\text{early}\rangle + e^{i\phi}\sqrt{1-\alpha^2}|\text{late}\rangle$. Since AFC is a first-in-first-out storage protocol [101], the $|\text{early}\rangle$ and $|\text{late}\rangle$ pulses will be emitted in the same order, leading to an output state identical to the input state in the case of an ideal protocol: $|\psi_{\text{out}}\rangle = \alpha|\text{early}\rangle + e^{i\phi}\sqrt{1-\alpha^2}|\text{late}\rangle$.

The atomic frequency comb is created using spectral holeburning. To create an atomic frequency comb in $^{167}Er^{3+}$:Y_2SiO_5 in our experiments, a set of periodic spectral holes is burned in the absorption line after hyperfine initialization (see Section 2.3). Each hole is created by pumping on the transitions at that optical frequency with a laser, until population is moved to other long-lived hyperfine levels. The teeth of the comb are the remaining absorption peaks between the

spectral holes. See Figure 5.2 for pulse sequence and comb scan. Side-holes and anti-holes from other hyperfine transitions are usually outside of the frequency window of the comb. Superhyperfine side-holes and anti-holes, however, affect the comb structure (see Section 2.4). Combs of arbitrary finesse $F = \frac{\Delta}{\gamma}$ are created by creating spectral trenches between the comb teeth. These trenches are created by scanning the laser in frequency as it pumped away population. See Figure 6.2 for pulse sequence, and Figure 6.3 for a scan of a high finesse comb.

In some cases, the AFC was created using the accumulated AFC method [34], where the entire frequency comb is created simultaneously by creating an optical frequency comb and imprinting that onto the ion absorption line. See Figure 5.3 for a pulse sequence used to generate a comb in this way. The finesse obtained with this method is always $F \sim 2$.

AFC with spin-wave

Up to this point, we have described storing light on an optical transition using an atomic frequency comb. All quantum storage experiments in this thesis were done according to this procedure, which is usually referred to as "optical AFC". However, this is only part the AFC protocol as it was originally proposed in Reference [4].

The full protocol, called spin-wave AFC, requires two additional optical pulses and an empty hyperfine level to which population from the excited state can be coherently and reversibly transferred. Additionally, a microwave frequency oscillating magnetic field ($\sim$ 850 MHz) would be needed to rephase the inhomogeneously broadened spins during storage.

In the AFC with spin-wave protocol, after an input pulse (or input qubit) is stored on the optical transition, an optical π pulse coherently moves population from the optical excited state to a second long-lived spin state in the optical ground state manifold. The coherence is then stored between the two ground state levels for a time that is limited by the spin coherence time T_{spin}. This time can be much longer than the optical coherence time. For example, in $^{167}Er^{3+}$:Y_2SiO_5, hyperfine coherence times longer than 1 second have been measured [86]. After some desired wait time $T_s < T_{\text{spin}}$, another optical π pulse moves the population from the second spin state back to the excited state, and the phase evolution continues until $t = \frac{1}{\Delta} + T_s$, when the ions rephase and the output pulse is emitted. During the storage on the spin state, microwave pulses are usually used to rephase the inhomogeneously broadened spin ensemble.

3.2 AFC Storage Efficiency in a Cavity

In this work, we use on-chip resonators to enhance the coupling between light and ensembles of $^{167}Er^{3+}$:Y_2SiO_5 ions. This allows the miniaturization of devices and can in theory lead to highly efficient storage of light using the atomic frequency protocol. Afzelius et al. showed that an atomic frequency comb memory can approach unit efficiency when the ensemble of ions is coupled to a cavity, and that coupling is characterized by an ensemble cooperativity of $C = 1$ [3]. This is called an impedance matched cavity quantum memory. A similar result was derived more generally by Moiseev et al. [80].

The efficiency of AFC storage in a cavity is given by [3, 80, 115]:

$$\eta_{AFC} = \left(\frac{4\kappa_{\text{in}}\Gamma_{\text{comb}}}{(\kappa_{\text{total}} + \Gamma_{\text{comb}} + \Gamma_{\text{bg}})^2} \right)^2 \eta_d, \tag{3.4}$$

where κ_{in} is the rate of cavity coupling through the input/output port, κ_{total} is the total energy decay rate of the cavity, and η_d accounts for dephasing due to the finite width of comb teeth [4]. Assuming spectral teeth with a Gaussian profile, this dephasing term equals:

$$\eta_d = \exp\left(-\frac{\pi^2}{2\ln 2(\Delta/\gamma)^2} \right). \tag{3.5}$$

Γ_{comb} and Γ_{bg} are the absorption rates of the cavity field by the ensemble of ions in the comb and background, respectively. Background ions are those ions remaining after optical pumping, with transition frequencies where transparency is desired (i.e. between the teeth of the comb). Nonzero Γ_{bg} results from limitations in spectral holeburning. Using η_{spectral}, the fractional optical depth of a spectral hole, Δ, the comb period, and γ, the width of one comb tooth, these can be estimated as follows:

$$\Gamma_{\text{comb}} \approx \eta_{\text{spectral}} \frac{\gamma}{\Delta} \Gamma_{\text{ions}}, \tag{3.6}$$

$$\Gamma_{\text{bg}} = \left(1 - \eta_{\text{spectral}}\right) \Gamma_{\text{ions}}, \tag{3.7}$$

where $\Gamma_{\text{ions}} = |W(\omega = \omega_{\text{ions}})| = \sqrt{\pi \log 2}\, g_{\text{total}}^2 / (\Delta_{\text{ions}}/2)$ is the absorption rate of the cavity field by the ensemble of ions before comb preparation (see Section 5.1 for definition of $W(\omega)$).

We can define an effective AFC cooperativity, C':

$$C' = \frac{\Gamma_{\text{comb}} + \Gamma_{\text{bg}}}{\kappa_{\text{total}}/2} = \left(\frac{\eta_{\text{spectral}}}{F} + (1 - \eta_{\text{spectral}})\right) C, \tag{3.8}$$

where $C = \Gamma_{\text{ions}}/(\kappa/2)$ is the ensemble cooperativity and $F = \frac{\Delta}{\gamma}$is the comb finesse.

Rewriting Equation 3.4 gives rise to the following expression for the AFC storage efficiency:

$$\eta_{AFC} = \left(\frac{1}{F\left(\frac{1}{\eta_{\text{spectral}}} - 1\right) + 1} \frac{\kappa_{\text{in}}}{\kappa_{\text{total}}} \frac{4C'}{(1 + C')^2}\right)^2 \eta_d. \tag{3.9}$$

The efficiency is maximized when $C' \to 1$. This is the impedance matched condition. In the case where the atomic frequency comb is burned efficiently (no background ions, $\eta_{\text{spectral}} \to 1$) and the cavity loss is minimal, $\frac{\kappa_{\text{in}}}{\kappa_{\text{total}}} \to 1$, and $\eta_d \to 1$ (which requires narrow teeth comb teeth), the memory efficiency approaches unity.

Ensemble Cooperativity

The ensemble cooperativity can be estimated from material parameters and simulation values. Consider the cooperativity before any spectral initialization for an ensemble of ions with a Gaussian distribution of transition frequencies:

$$C = \frac{\Gamma_{\text{ions}}}{\kappa/2} = \frac{4\sqrt{\pi \log 2} g_{\text{total}}^2}{\kappa \Delta_{\text{ions}}}. \tag{3.10}$$

Note that the factor of $\sqrt{\pi \log 2}$ comes from considering a Gaussian distribution [36, 79]. To estimate g_{total}, we first approximate the sum over ion couplings with an integral:

$$g_{\text{total}}^2 = \sum_i g_i^2 \approx \int_{V_{\text{YSO}}} \mathrm{d}\vec{r}\, \rho_{\text{ions}} g^2(\vec{r}) \tag{3.11}$$

where ρ_{ions} is the number density of ions. Using

$$g_i = \sqrt{\frac{\omega}{2\hbar V_{\text{mode}} \max\left\{\epsilon(\vec{r}) \left|\vec{E}(\vec{r})\right|^2\right\}}} \left|\vec{\mu} \cdot \vec{E}(\vec{r})\right|, \tag{3.12}$$

where μ is the ion optical dipole moment, and

$$V_{\text{mode}} = \frac{\int_V \mathrm{d}\vec{r}\, \epsilon(\vec{r}) |\vec{E}(\vec{r})|^2}{\max\left\{\epsilon(\vec{r}) \left|\vec{E}(\vec{r})\right|^2\right\}}, \tag{3.13}$$

g^2_{total} can be estimated by:

$$g^2_{\text{total}} \approx \frac{\rho_{\text{ions}}\omega|\mu|^2}{2\hbar\epsilon_{\text{YSO}}}\beta, \tag{3.14}$$

where

$$\beta = \frac{\int_{V_{\text{YSO}}} \mathrm{d}\vec{r}\, \epsilon_{\text{YSO}}|\vec{E}(\vec{r})\cdot\hat{\mu}|^2}{\int_V \mathrm{d}\vec{r}\, \epsilon(\vec{r})|\vec{E}(\vec{r})|^2}. \tag{3.15}$$

Note that this β is very similar to the fraction of the resonator mode energy in Y_2SiO_5, β_{mode}, defined in Eq. 4.1. If the electric field component optical mode of the resonator is mostly aligned with the electric dipole moment of the ions, then $|\vec{E}(\vec{r})\cdot\hat{\mu}| \approx |\vec{E}(\vec{r})|$ and $\beta \approx \beta_{\text{mode}}$. In this case, the ensemble cooperativity is approximated by:

$$C \approx \frac{2\sqrt{\pi \log 2}\rho_{\text{ions}}|\mu|^2\beta_{\text{mode}}Q}{\hbar\epsilon_{\text{YSO}}\Delta_{\text{ions}}}, \tag{3.16}$$

where $Q = \omega/\kappa$ is the resonator quality factor. This relationship shows that the ensemble cooperativity scales linearly with cavity quality factor, and the fraction of the optical mode in the Y_2SiO_5. It is inversely proportional to the linewidth of the ensemble absorption spectrum. Note that the ensemble cooperativity does not scale with the number of ions coupled to the cavity, but rather scales with the density of ions, $\rho_{\text{ions}} \sim \frac{N_{\text{ions}}}{V_{\text{mode}}}$.

Chapter 4

NANOPHOTONIC RESONATORS: DESIGN AND FABRICATION

In this chapter, we introduce the optical resonators coupled to $^{167}Er^{3+}$:Y_2SiO_5 ions which are used in Chapters 5 and 6 to store light with the AFC protocol. We first introduce the $^{167}Er^{3+}$:Y_2SiO_5 nanobeam resonators which will be used for quantum storage in Chapter 5. Not much is said about these resonators as they have been previously described elsewhere. Next, we introduce in more detail the hybrid amorphous silicon $^{167}Er^{3+}$:Y_2SiO_5 resonators, which will be used in Chapter 6. We describe their design and fabrication. We end with the design and fabrication of the electrodes used for Stark shift control in Chapter 6. We show simulations of the electric field for two configurations, parallel and quadrupole, which enable the multiple functions of this device.

4.1 Y_2SiO_5 Nanobeam Resonators

Figure 4.1 shows the nanoresonator used in the quantum storage experiment described in Chapter 5. Jake Rochman designed and fabricated the resonator, as described in Reference [114]. The triangular nanobeam photonic crystal cavity was milled in a Y_2SiO_5 crystal from Scientific Materials doped with isotopically purified $^{167}Er^{3+}$ (92% purity) at a nominal concentration of 50 ppm. The nanobeam was 1.5 μm wide and $\sim$ 20 μm long. The slots in the nanobeam created a photonic crystal bandgap and the periodic pattern (lattice constant = 590 nm, groove width = 450 nm) was modified quadratically in the center to create a cavity mode.

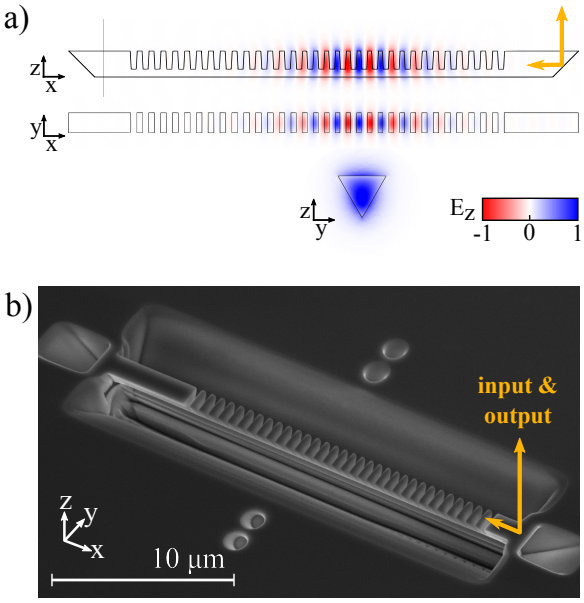

Figure 4.1: Nanobeam resonator simulation and micrograph (adapted from Ref. [30]). (a) Finite element analysis simulation of the TM cavity mode in the triangular nanobeam resonator. Red-blue color gradient indicates the electric field component normal to the surface, E_z; black outline indicates Y_2SiO_5 -air interface; yellow arrow indicates coupling. (b) Scanning electron micrograph of the resonator, showing input/output coupling through a 45° angled slot coupler.

4.2 Hybrid Amorphous Silicon-Y_2SiO_5 Resonators

The hybrid αSi-$^{167}Er^{3+}$:Y_2SiO_5 resonator used for the Stark shift AFC-storage experiment is described in Chapter 6. The Fabry-Perot type resonator was comprised of a waveguide with photonic crystal mirrors on either end. The resonators were designed by Jake Rochman and fabricated by myself and Mi Lei.

Design

Figure 4.2a shows an amorphous silicon (αSi) waveguide on a Y_2SiO_5 substrate (w = 605 nm, h = 310 nm), and Figure 4.2b shows the fundamental TM mode in this waveguide, simulated using COMSOL. A fraction of the optical mode penetrates into the $^{167}Er^{3+}$:Y_2SiO_5 and evanescently couples to $^{167}Er^{3+}$ions.

The effective mode index for the fundamental TM mode is n_{eff} = 2.5. The fraction of the optical mode energy in $^{167}Er^{3+}$:Y_2SiO_5 was found from simulation to be β_{mode} = 0.1 using:

$$\beta_{\text{mode}} = \frac{\int_{V_{\text{YSO}}} d\vec{r}\, \epsilon_{\text{YSO}} |\vec{E}(\vec{r})|^2}{\int_V d\vec{r}\, \epsilon(\vec{r}) |\vec{E}(\vec{r})|^2}, \tag{4.1}$$

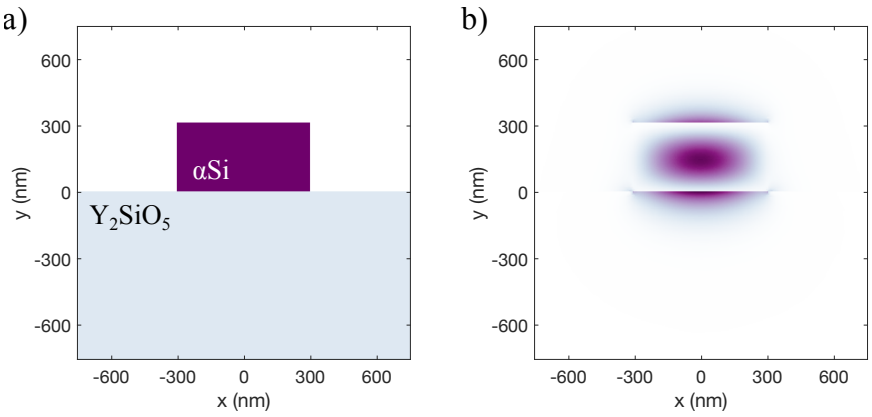

Figure 4.2: Hybrid αSi-$^{167}Er^{3+}$:Y_2SiO_5 waveguide simulation. a) Materials: amorphous silicon ($n = 3.5$) in purple, Y_2SiO_5 ($n = 1.8$) in light blue, surroundings in white are air ($n = 1$). b) Fundamental TM mode in waveguide. Purple-white gradient shows electric field in the y-direction, E_y.

where $\vec{E}(\vec{r})$ is the electric field, $\epsilon(\vec{r})$ is the material permittivity (ϵ_{YSO} is the permittivity of Y_2SiO_5), and V is the simulation volume (V_{YSO} is the Y_2SiO_5 volume in the simulation).

To maximize coupling between the optical mode and the ensemble of ions, β_{mode} should be as large as possible. Its role in the efficiency of AFC quantum storage is discussed in Section 3.2.

Mirrors in the form of 1D photonic crystal (periodic dielectric waveguides [55]) are placed on either side of a 100 μm long waveguide to create an on-chip Fabry-Perot resonator. As shown in Figure 4.3, elliptical air holes are added to the αSi-$^{167}Er^{3+}$:Y_2SiO_5 waveguide in a periodic pattern to create a photonic crystal bandgap centered at the design frequency of $\nu_\circ = 195$ THz. Figure 4.3a shows the simulated bandgap of an infinite 1D photonic crystal, along with the dispersion of the waveguide mode. For the photonic crystal simulation, even y symmetry was imposed to ensure that the first band gap was the fundamental TM mode (in this 3D simulation the electric field of the TM mode is along the z axis). The wavenumber of the evanescent mode in the photonic crystal is $k_{\mathrm{PhC}} = \frac{2\pi}{a_\circ}$, while the wavenumber of the TM waveguide mode is $k_{\mathrm{PhC}} = \frac{2\pi n_{\mathrm{eff}}}{\lambda_\circ}$ (given by the intersection of the two red lines in Figure 4.3a), where $\lambda_\circ = c/\nu_\circ$ and $n_{\mathrm{eff}} = 2.5$. The difference in k values of the two modes leads to scattering between photonic crystal and waveguide. To mitigate this scattering, a taper region is introduced in the photonic crystal, where the hole size and period are both gradually reduced. The purpose of the taper is to adiabatically change the photonic crystal Bloch mode into the TM waveguide mode.

The last hole in the taper is circular with a radius of $r_{1,f} = r_{2,f} = 25$ nm and the last spacing between holes is $a_f = 310$ nm. A photonic crystal with these parameters was simulated, and as shown in Fig. 4.3a, one of the modes in its band diagram has a k value at $\nu_\circ = 195$ THz very close to that of the waveguide.

Figure 4.3b shows a COMSOL simulation of a finite photonic crystal mirror (20 holes) with tapered regions on either side. A TM waveguide mode is launched from the port on the left and the reflectance is measured to be $R = 0.988$ from simulation. To make one side of the resonator more strongly coupled, one mirror could have fewer holes. In the resonators used in Chapter 6, 30 taper holes (15 on either side) were used in all resonators, and the coupling side mirror had either 4 or 6 holes excluding the taper, while the second, more reflective, mirror had 30 holes excluding the taper. Appendix A describes the COMSOL simulation in more detail and includes the code for the band diagram simulations.

To couple light into the waveguide mode, a grating coupler similar to that in [79] was used. A scanning electron micrograph of such a coupler is shown in Figure 4.8. The simulated and measured one-way coupling of the grating coupler was 40% – 50%.

When measuring our devices at cryogenic temperatures, we observed that the resonances shifted by ~ 14 nm to the blue (lower wavelength) when cooling down from room temperature to 4 K. Therefore, the target resonance for the fabricated device at room temperature should actually be at ~ 193 THz (~ 1553 nm). A bandgap centered at this new frequency can be easily achieved with small modifications to the photonic crystal described in Fig. 4.3, for example increasing the period to $a_\circ = 380$ nm and increasing the hole semi-major axis to $r_{1,\circ} = 135$ nm.

One approach to increase β_{mode} in a hybrid device is to decrease the height of the αSi waveguide, which pushes more of the mode into the $^{167}Er^{3+}$:Y_2SiO_5. Another approach is to use a slot-mode waveguide [6], where the mode maximum is in an air gap between two αSi waveguides. Since the slot mode is mainly in air, the denominator of Equation 4.1 is smaller, leading to higher β_{mode} values. During his SURF, Dimitrie-Calin Cieleki simulated slot mode resonators using slot waveguides with photonic crystal mirrors for quantum memories. Both thinner waveguides ($h = 250$ nm) and slot mode waveguides were fabricated, but neither led to improvements

[1]Note that in Figure 4.3, the blue area (extended modes in the Y_2SiO_5) on the left applies to all modes, but the blue area on the right only applies to modes in the photonic crystal with period $a_\circ = 370$ nm, since that crystal's band diagram is symmetric about $k = \frac{2\pi}{a_\circ}$, whereas the band diagram for the photonic crystal with period $a_f = 310$ nm is symmetric about $k = \frac{2\pi}{a_f}$, and the band diagram for the waveguide is not symmetric.

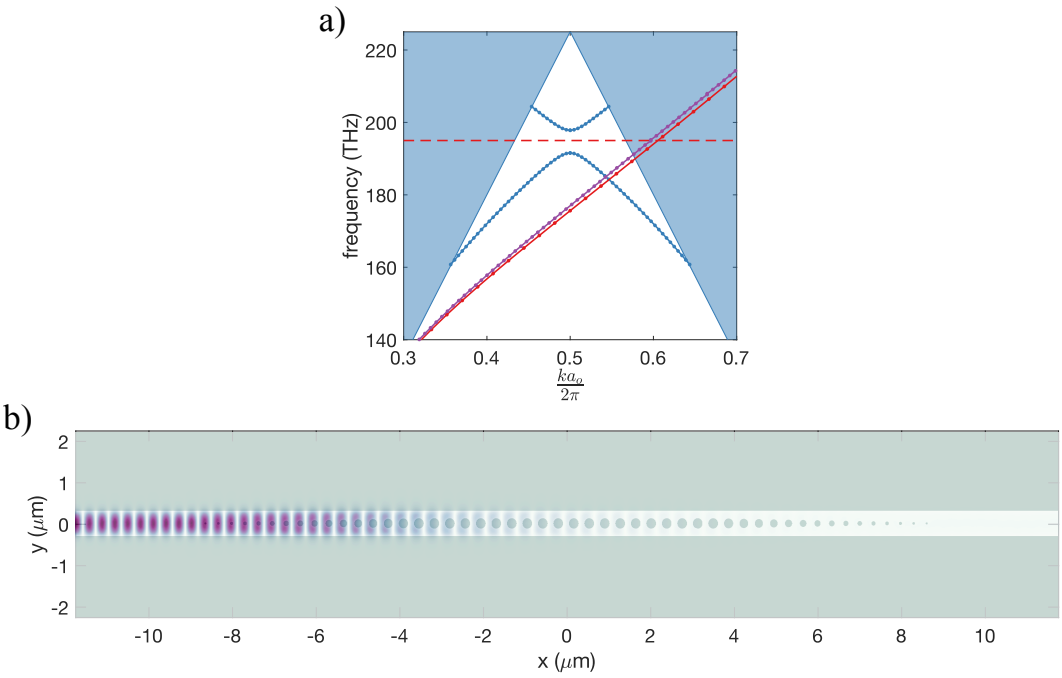

Figure 4.3: Hybrid αSi-$^{167}Er^{3+}$:Y_2SiO_5 photonic crystal mirror simulation. a) Band diagram $\omega(k)$ of photonic crystal and waveguide, simulated using the harmonic mode solver MPB [57]. Connected blue circles: modes of a photonic crystal comprised of periodic elliptical air holes with semi-major axis $r_{1,\circ} = 125$ nm, semi-minor axis $r_{2,\circ} = 115$ nm, period $a_\circ = 370$ nm, in a waveguide $h = 310$ nm, $w = 605$ nm ($r_{2,\circ}$ is parallel to the long axis of the waveguide). Blue areas are the light cone where extended modes propagating in bulk Y_2SiO_5 exist, delineated by the light line in Y_2SiO_5 $\omega = \frac{c}{n_{YSO}}k$[1]. The red dashed line shows the design resonance frequency $\nu_\circ = 195$ THz. The solid red line shows the dispersion of the waveguide ($h = 310$ nm, $w = 605$ nm) with no air holes. Connected purple dots show one mode of a photonic crystal created by the last hole in the taper (see (b) and main text for details). b) 2D slice at $z = h/2 = 155$ nm from a 3D COMSOL simulation of a photonic crystal mirror with 20 regular-sized holes and 15 taper holes on either side. The taper hole dimensions are determined by linear interpolation between $a_\circ$, $r_{1,\circ}$, $r_{2,\circ}$ and $a_f = 310$ nm, $r_{1,f} = r_{2,f} = 25$ nm. The purple mode in (a) is for a photonic crystal with the latter parameters. Purple-white color gradient shows the out of plane electric field component E_z. Solid green (white) background shows air (αSi) at $z = h/2 = 155$ nm.

over the $h = 310$ nm design. As detailed in Section 3.2, high AFC efficiency requires an ensemble cooperativity $C > 1$ ($C' = 1$), which is greater than cooperativities achieved so far for nanophotonic resonators coupled to $^{167}Er^{3+}$:Y_2SiO_5. C depends linearly on both the cavity quality factor Q and β_{mode} (see Equation 3.16). Any increase in β_{mode} achieved in fabricated thinner or slot mode devices was offset by an equal or greater decrease in measured Q. The reason for this is that the photonic

crystal mirror designs for either thinner or slot waveguides were more sensitive to fabrication errors than those for the $h = 310$ nm waveguide.

Fabrication

The fabrication process for the hybrid αSi-$^{167}Er^{3+}$:Y_2SiO_5 resonators, outlined in Figure 4.4, was similar to the process described in References [77, 79]. A Y_2SiO_5 boule with nominal $^{167}Er^{3+}$ doping of 200 ppm was custom-grown by Scientific Materials (FLIR) and diced and polished by Brand Laser Optics & Mfg. The crystal was grown using the Czochralski method, with $^{167}Er^{3+}$ incorporated in the melt. The $^{167}Er^{3+}$ concentration was measured to be 135 ppm using secondary ion mass spectrometry. Each Y_2SiO_5 piece had dimensions (8.5 mm $\times$ 7.5 mm $\times$ 0.5 mm) along the ($b \times D_2 \times D_1$) crystal axes. 310 nm of amorphous silicon (αSi) was deposited using plasma-enhanced chemical vapor deposition (PECVD) using 5% SiH_4 in Ar at 200 °C (Fig. 4.4i). 10 nm of Ti was evaporated as a charge conduction layer for electron beam lithography. A negative resist was spun onto the Y_2SiO_5 chip (300 nm of flowable oxide diluted in MIBK) and patterned using electron beam lithography using a 100 kV, 300 pA beam (Fig. 4.4ii). The fluid oxide was developed using tetramethylammonium hydroxide (TMAH). The pattern was transferred to the αSi using inductively coupled plasma reactive ion etching (ICP-RIE) with SF_6/C_4F_8 chemistry (Fig. 4.4iii). The fluid oxide was removed with dilute HF. Scanning electron micrographs of fabricated resonators are shown in Figure 4.8.

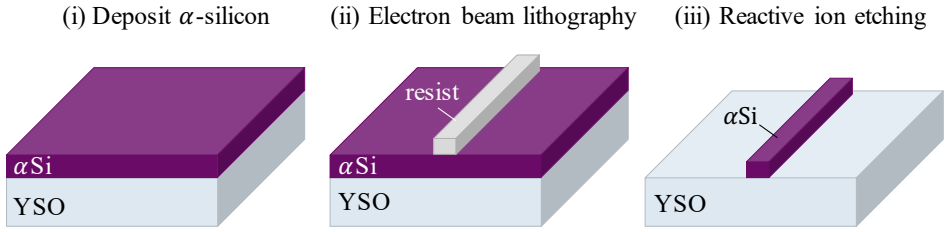

Figure 4.4: Hybrid αSi-$^{167}Er^{3+}$:Y_2SiO_5 resonator fabrication. Details in main text.

4.3 On-Chip Electrodes for DC Stark Shift Control

On chip electrodes were integrated with the hybrid αSi-$^{167}Er^{3+}$:Y_2SiO_5 resonator to enable dynamic control of the AFC output pulses. This section describes the design and fabrication of on-chip electrodes used in the experiments in Chapter 6. The electrodes were designed and fabricted by Mi Lei and myself.

Design

For the control sequences in Chapter 6, two different electric field distributions were desired: (1) A constant distribution $E_y(x) = E_y$ as in a parallel plate capacitor, (2) A linearly varying distribution $E_y(x) = xE_{y,\circ}$ as in a quadrupole electrode configuration. Electrodes in both parallel [7, 73] and quadrupole [5, 64, 72] configurations have been used previously in rare earth ion storage experiments using protocols such as AFC-CRIB [64], GEM [5, 72] or SEMM [7]. The four-electrode design used in this work was chosen to meet the following criteria: (1) Electric field applied over 100 μm length of resonator. (2) Operate in one "parallel" configuration with high homogeneity of field. (3) Operate in a second "quadrupole" configuration with a field that approximates a linear gradient. (4) Provide a high electric field E_y with low applied potential ΔV.

The electrode design is shown in Figure 4.5a. Four circles ($r = 35$ μm) provide an electric field with a linear gradient in the quadrupole configuration, while the four rectangles (20 μm $\times$ 60 μm) connected to the circles create a more homogeneous field in the parallel configuration. The center-to-center distance between the circles are $d_y = 90\mu$m and $d_x = 150\mu$m. Each of the 4 electrodes can be biased individually using wires that are not shown in the figure. Figures 4.5b-f show results from a 3D COMSOL Electrostatics simulation. Figures 4.5c and 4.5d show the potential V in the parallel and quadrupole configurations. Fig. 4.5b shows the electric field distribution for the two cases. The dashed lines show the ideal homogeneous and linear gradient electric field distributions.

Figures 4.5e and 4.5f show the proportion of ions that experience each electric field $\rho_{\text{ions}}(E_y) \sim (\frac{\mathrm{d}E_y}{\mathrm{d}x})^{-1}$ in the two configurations. $\rho_{\text{ions}}(E_y)$ is a probability distribution from which the electric field which each ion experiences is sampled, normalized such that $\int_{-\infty}^{\infty} \mathrm{d}E\, \rho_{\text{ions}}(E) = 1$. This assumes a uniform distribution of ions along the x axis, which is a reasonable assumption for uniformly doped $^{167}Er^{3+}$:Y_2SiO_5 crystals. The goal in the parallel configuration is to apply one electric field to all ions, which is represented by a delta function in Fig. 4.5e (dashed line). The goal in the quadrupole configuration is to apply a different frequency to each ion, as represented by the uniform distribution in Fig. 4.5f (dashed line).

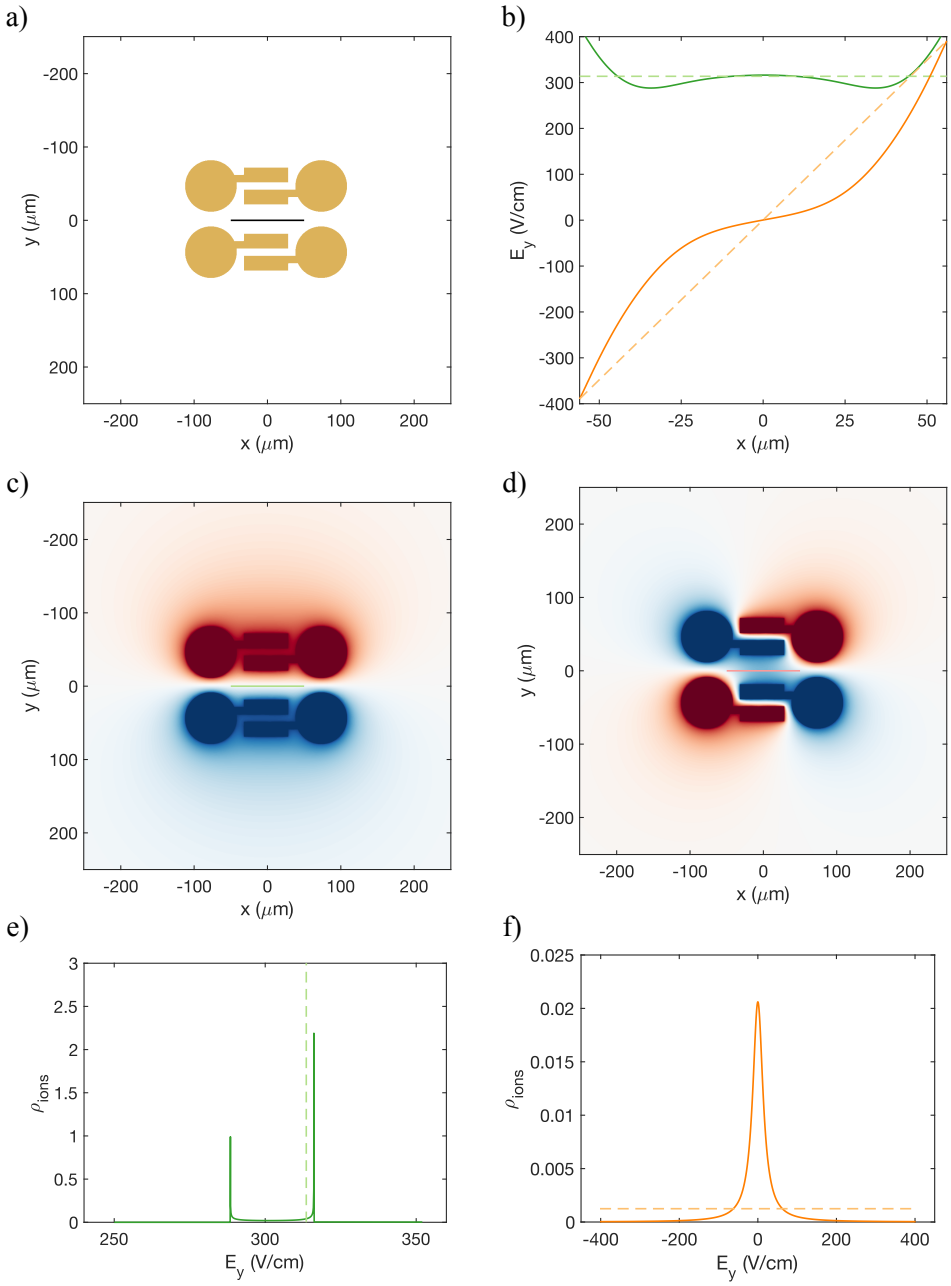

Figure 4.5: Simulations of on-chip electrodes. a) Gold electrodes on Y_2SiO_5. Black line denotes position of αSi-$^{167}Er^{3+}$:Y_2SiO_5 resonator ($y = 0, z = 0, -50\,\mu\text{m} < x < 50\,\mu\text{m}$). b) Simulated electric field distribution at $y = 0, z = 0$ (solid lines) and ideal electric field distribution (dashed lines) for the two biasing configurations: parallel (green) and quadrupole (orange). The bias applied to each electrode is $\pm 1V$. c) Parallel biasing configuration: potential V in red-white-blue gradient. Green line indicates position of resonator. d) Quadrupole biasing configuration: potential $-1 < V < 1$ in red-white-blue gradient. Orange line indicates position of resonator. e) and f) Proportion of ions experiencing every electric field value $\rho_{\text{ions}}(E_y)$ in the parallel (e) and quadrupole (f) configurations. $\rho_{\text{ions}}(E_y)$ from simulated field profile in (b) (solid lines) and ideal (dashed lines).

The TM optical mode of the resonator only penetrates a few hundred nanometers ($1/e \sim 150$ nm), while the $1/e$ point of the electric field in the z direction is tens of microns. Therefore the electric field does not change significantly in the z direction, so only values at $z = 0$ are shown. Likewise, there was no significant variation in electric field in the y direction over the 605 nm width of the optical resonator. However, the optical mode is expected to penetrate significantly into the photonic crystal mirrors as seen in Figure 4.3b. The electric field $E_y(x)$ was therefore simulated for $-56\,\mu\text{m} < x < 56\,\mu\text{m}$ for Figures 4.5b,e and f. The value of 6 μm as an effective penetration depth of the optical mode was decided empirically as discussed in Section 6.4.

Other electrode geometries are possible. Figure 4.6 compares the electric field distributions for the final design (from Fig. 4.5), a similar design without the rectangular electrodes, and a third design without rectangular electrodes where the circular electrodes are evenly spaced at $d_x = d_y = 150\,\mu$m. The latter design meets criteria (1-3), but the electric field magnitude achieved is 4 times lower than the final design. Bringing the electrodes closer together, as in the second design, increases the maximum field achieved, but leads to large inhomogeneity in the parallel configuration (see Fig. 4.6a). Figure 4.6b also shows that adding the rectangular electrodes does not significantly affect the quadrupole configuration electric field profile.

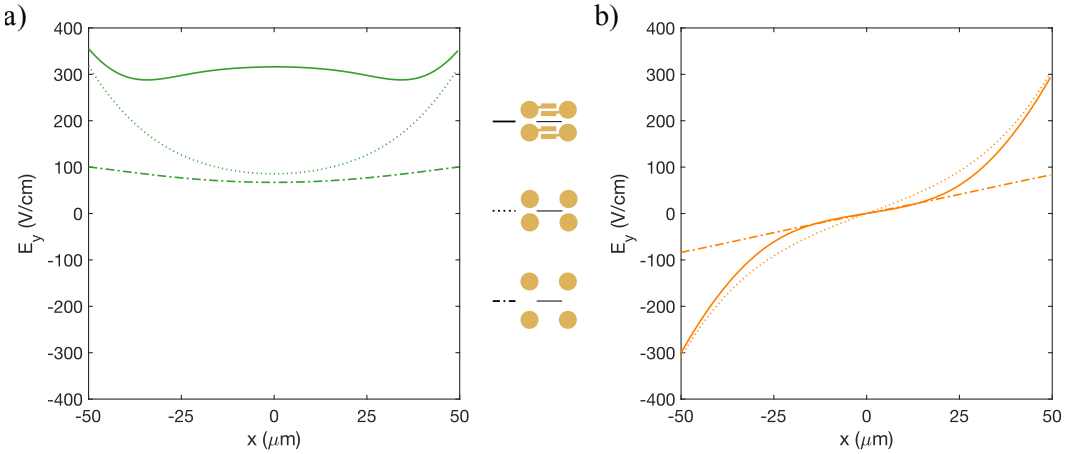

Figure 4.6: Various electrode designs. Electric field profile at $y = 0, z = 0$ for the parallel (a) and quadrupole (b) biasing configurations of three electrode designs. Details in main text.

Fabrication

On-chip electrodes were added after the hybrid αSi-$^{167}Er^{3+}$:Y_2SiO_5 resonators were fabricated. Figure 4.7 shows the fabrication process for the electrodes. A $\sim$ 450 nm

layer of positive resist (PMMA) was spun on the Y_2SiO_5 chip with αSi resonators already patterned. Aligned electron beam lithography was used to pattern the electrodes, with a 100 kV, 100 nA beam (Fig. 4.7i). Alignment was made possible by an array of 20 μm $\times$ 20 μm gold markers, which were patterned before the resonators using the same procedure as in Fig. 4.7. Both the resonator pattern and electrode pattern were aligned to the same marker grid. After developing the PMMA resist using an MIBK-IPA mixture, a 10 nm Ti adhesion layer was evaporated onto the chip, followed by a 100 nm gold film (Fig. 4.7ii). The chip was soaked in acetone to dissolve the PMMA and lift off the excess gold film, leaving behind the patterned electrodes (Fig. 4.7iii). Appendix B describes the fabrication steps for the on-chip electrodes in more detail.

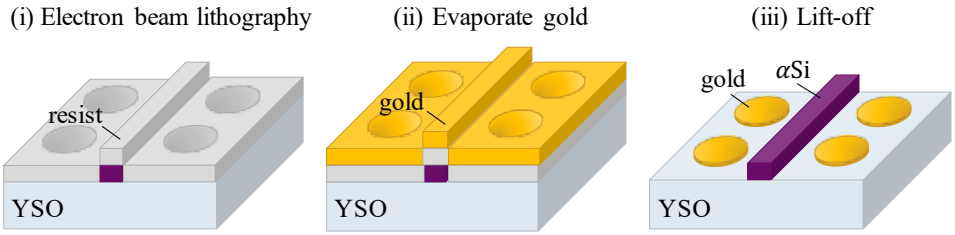

Figure 4.7: Fabrication of on-chip electrodes. Details in main text.

Figure 4.8 shows a completed hybrid αSi-$^{167}Er^{3+}$:Y_2SiO_5 device with a closeup of a photonic crystal mirror and a grating coupler. Up to 81 such devices were patterned on the same D_1-cut Y_2SiO_5 chip, with resonators aligned either to the b or D_2 crystal axes. 10 μm wires, shown in Fig. 4.8a, connected the electrodes to 300 μm $\times$ 300 μm contact pads, which were connected via aluminium wire bonds to SMP connectors on a custom-made PCB board (see Appendix D).

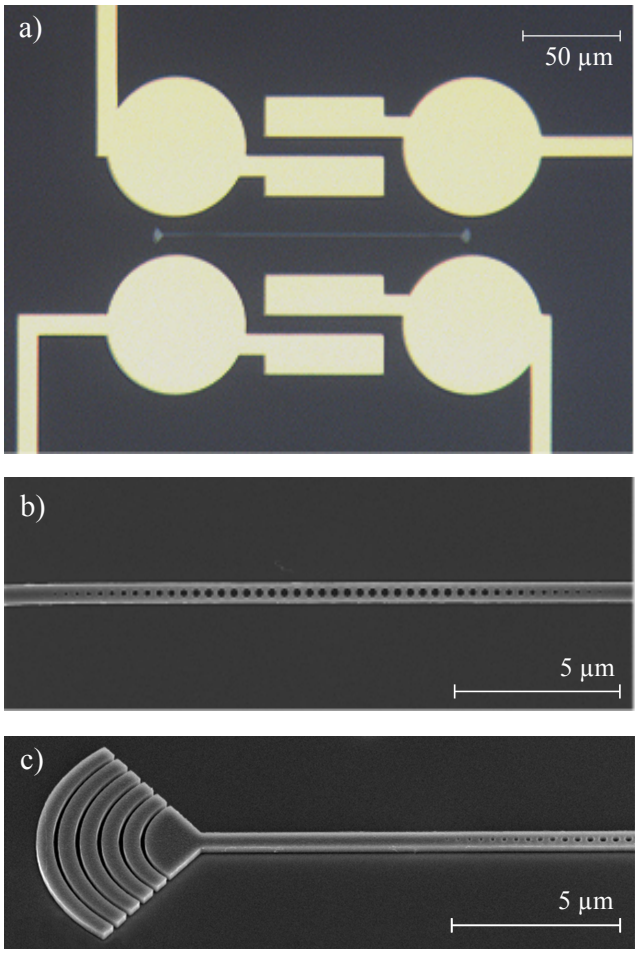

Figure 4.8: Hybrid αSi-$^{167}Er^{3+}$:Y_2SiO_5 resonator with electrodes. a) Optical micrograph of a hybrid αSi-$^{167}Er^{3+}$:Y_2SiO_5 with electrodes. b) Scanning electron micrograph of an αSi photonic crystal mirror, shown here on a sapphire substrate ($n_{\text{Sapphire}} = n_{\text{YSO}} = 1.8$). c) Scanning electron micrograph of an αSi grating coupler on sapphire. Imaged at a 40° angle.

Chapter 5

QUANTUM STORAGE IN AN $^{167}Er^{3+}$:Y_2SiO_5 NANOBEAM

In this chapter, we demonstrate on-chip quantum storage of telecommunication light at the single photon level. The results were first presented in Reference [30], and this chapter is an expanded version of that manuscript. We used a nanophotonic crystal resonator milled directly in $^{167}Er^{3+}$ doped Y_2SiO_5 ($^{167}Er^{3+}$:Y_2SiO_5) to couple to an ensemble of erbium ions and realize quantum storage using the AFC protocol [4]. The resonator, which was introduced in Section 4.1, increased the absorption of light by the ion ensemble, allowing on-chip implementation of the memory protocol [3]. By working in a dilution refrigerator and using permanent magnets to apply a field of 380 mT, we accessed a regime in which the ions have optical coherence times of $\sim 150\,\mu$s and long-lived spin states to allow spectral tailoring. For a storage time of 165 ns, we achieved an efficiency of 0.2%, with lower efficiencies for longer storage times, up to 10 μs. We demonstrated storage of multiple temporal modes and measured a high fidelity of storage, exceeding the classical limit. We then identified the limits on the storage efficiency and proposed avenues for overcoming them to achieve an efficient $^{167}Er^{3+}$:Y_2SiO_5 quantum memory for light. Appendix C describes experimental setup used for measurements in this chapter.

5.1 Coupling Between an Ensemble of Ions and a Cavity

The coupling between an ensemble of absorbers and a cavity can be characterized by measuring the reflectance curve of the cavity-ion system. Following Reference [36], we fit the reflectance curve to the following model:

$$R = \alpha_1 \left| (1-\alpha_f) + \alpha_f e^{i\theta_f} - \frac{i\kappa_{\text{in}}}{\omega - \omega_{\text{cavity}} + i\frac{\kappa}{2} + W(\omega, g_{\text{total}}, \Delta_{\text{ions}}, \omega_{\text{ions}})} \right|^2 + \alpha_2 \quad (5.1)$$

where $\alpha_{1,2}$ are amplitude and background fit parameters, $\alpha_f e^{i\theta_f}$ accounts for Fano interference (both α_f and θ_f are fit parameters), κ is the total cavity energy decay rate, κ_{in} is the coupling rate through the input/output port, and ω_{cavity} is the cavity resonance frequency. $W(\omega, g_{\text{total}}, \Delta_{\text{ions}}, \omega_{\text{ions}})$ is the absorption rate of the cavity field by the ensemble of ions, $W \sim \sum_i \frac{g_i^2}{\omega - \omega_i}$, where g_i is the coupling between one ion and the cavity [3, 36]. We approximated the irregular shape of the inhomogeneously

and hyperfine broadened optical transition as a Gaussian, and used the expression for W from Reference [36]:

$$W = i\frac{\sqrt{\pi \log 2}\, g_{\text{total}}^2}{\Delta_{\text{ions}}/2}\left[1 - \text{erf}\left(-\frac{i\sqrt{\log 2}(\omega - \omega_{\text{ions}})}{\Delta_{\text{ions}}/2}\right)\right] \times \exp\left[-\log 2\left(\frac{\omega - \omega_{\text{ions}}}{\Delta_{\text{ions}}/2}\right)^2\right], \tag{5.2}$$

where Δ_{ions} is the ensemble transition's linewidth, ω_{ions} its the center, and $g_{\text{total}}^2 = \sum_i g_i^2$. Finally, the ensemble cooperativity was computed using Equation 3.10, where $\Gamma_{\text{ions}} = |W(0)|$ [79].

Figure 5.1 shows the reflection spectrum of the nanobeam cavity, which has a measured loaded quality factor of 7×10^3. The cavity was tuned onto resonance with the 1539 nm transition of the $^{167}Er^{3+}$ ions by freezing nitrogen gas onto the nanobeam at cryogenic temperatures [82]. The coupling of the ensemble of ions to the cavity is seen as a peak in the cavity reflection dip. The inset shows a close-up of the ion-cavity coupling (in black). The ensemble cooperativity was estimated from a fit to this curve to be 0.1.

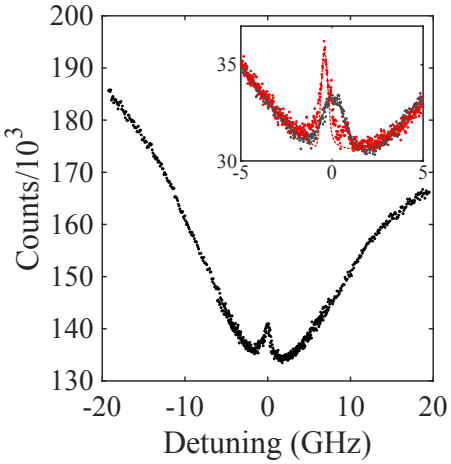

Figure 5.1: Reflection spectrum of nanobeam resonator when tuned on resonance to the 1539 nm $^{167}Er^{3+}$:Y_2SiO_5 transition (adapted from Ref. [30]). Detuning is measured from 194816 GHz ± 2 GHz. Inset shows a close-up of ion coupling before (black) and after (red) partial hyperfine initialization. Circles are data points; solid black and dashed red lines are fits to theory (see main text for details).

For high efficiency storage using ions coupled to a cavity, the ensemble cooperativity should equal one (see Section 3.2). An increased ensemble cooperativity of 0.3 (inset of Fig. 5.1, in red), was obtained using a partial hyperfine initialization procedure

(see Section 2.3). To extract the cooperativity of coupling between a resonator and an ensemble of $^{167}Er^{3+}$ ions, each cavity reflection spectrum shown in the inset of Fig. 5.1 was fit using Equation 5.1. $\kappa = 27.3$ GHz and $\frac{\kappa_{in}}{\kappa} = 0.21$ were measured from reflectance curves where the cavity was detuned from the $^{167}Er^{3+}$ transition.

For the case with no initialization, the fit yielded: $\omega_{cavity} - \omega_{ions} = 2\pi \times 2.5$ GHz, $g_{total} = 2\pi \times 0.79$ GHz, $\Delta_{ions} = 2\pi \times 1.4$ GHz, $C = 0.1$.

For the case with initialization, the fit yielded: $\omega_{cavity} - \omega_{ions} = 2\pi \times 1.5$ GHz, $g_{total} = 2\pi \times 0.70$ GHz, $\Delta_{ions} = 2\pi \times 0.36$ GHz, $C = 0.3$.

5.2 Atomic Frequency Comb Storage

The nanobeam device was used to demonstrate quantum optical storage using the AFC protocol [4]. In this protocol, a pulse of light that is absorbed by an atomic frequency comb with an inter-tooth spacing of Δ is stored for $t = \frac{1}{\Delta}$. Frequency selective optical pumping was used to create a comb within the inhomogeneous linewidth, as shown in Fig. 5.2a. Figure 5.2b shows a schematic of the protocol. First, a long pulse with strong frequency modulated sidebands was used for partial hyperfine initialization (see Section 2.3). The next 15 pulses, repeated $n_{pump} = 20$ times, created the comb: the laser frequency was swept through 15 values, separated by $\Delta = 6.1$ MHz, to optically pump away ions and create 15 spectral transparencies. The following $n_{input} = 60$ pulses were zero-detuning weak coherent states which were stored in the frequency comb. The full experiment was repeated $\sim 10^4$ times. As shown in Fig. 5.2c, 60 ns wide pulses with an average photon number of $\bar{n} = 0.60 \pm 0.09$ were stored for 165 ns with an efficiency of 0.2%. The storage efficiency was limited by the ensemble cooperativity of the device (see Section 3.2).

Coherent pulses could be stored in the device for up to 10 μs, although with a lower efficiency of 10^{-5}, as shown in Fig. 5.3. Here, as for all storage times longer than 165 ns, we used an accumulated AFC method [34] to create the comb (see Section 3.1). As shown in the inset of Fig. 5.3, weak pairs of pulses separated by $t_{storage} = 10$ μs were repeatedly sent into the cavity. The Fourier transform of each pulse pair is a frequency comb, which imprinted onto the $^{167}Er^{3+}$:Y_2SiO_5 inhomogeneous line to create the AFC. This procedure utilized laser frequency stabilization during comb creation, which enabled the creation of fine-toothed AFCs required for longer storage. For the 165 ns storage, where a coarser AFC is practical, the procedure shown in Fig. 5.2b with no laser frequency stabilization led to higher efficiencies by creating a more consistent comb over the entire bandwidth. This is

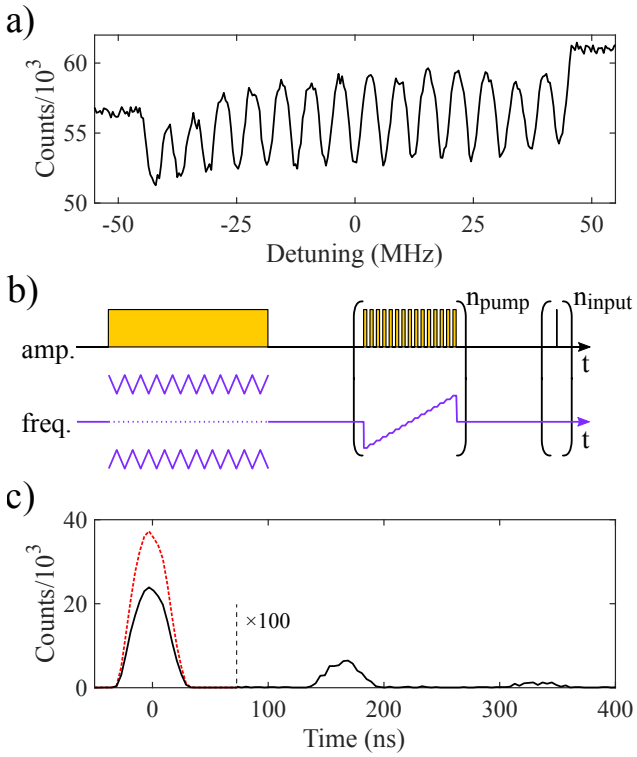

Figure 5.2: AFC experiment in the nanobeam cavity (adapted from Ref. [30]). (a) A section of the resonator reflection spectrum, showing an atomic frequency comb in the center of the inhomogeneously broadened $^{167}Er^{3+}$:Y_2SiO_5 transition. Detuning is measured from 194814.2 GHz ± 0.1 GHz. The apparent slope of the comb is due to its center frequency not being precisely aligned to the cavity resonance, leading to a dispersive shape. (b) Schematic of AFC pulse sequence showing amplitude (yellow) and frequency (purple) modulation of the laser (pulses not to scale, see main text for detail). (c) AFC storage: the input pulse (red dashed line) was partially absorbed by the comb; an output pulse was emitted at time $t = 1/\Delta = 165$ ns (black line, ×100). The black line also shows the partially reflected input pulse ($t = 0$) and a smaller second output pulse at $t = 330$ ns.

because the accumulated AFC has a sinc function envelope. The storage efficiency at 10μs was limited by residual laser frequency jitter and by superhyperfine coupling to the yttrium ions in Y_2SiO_5. Superhyperfine coupling limits the narrowest spectral feature to $\sim$ 2 MHz at this field (see Section 2.4). Since this exceeds the period of the comb needed for this storage time ($\Delta = 1/t_{\text{storage}} = 0.1$ MHz), the resulting AFC will have a lower contrast, leading to lower storage efficiency.

The AFC protocol is capable of storing multiple temporal modes [4]. Ten coherent pulses were stored in this device, as shown in Fig. 5.4. The AFC in Figure 5.2a has a bandwidth of $\sim$ 90 MHz (see Fig. 5.2a) which can accommodate storage

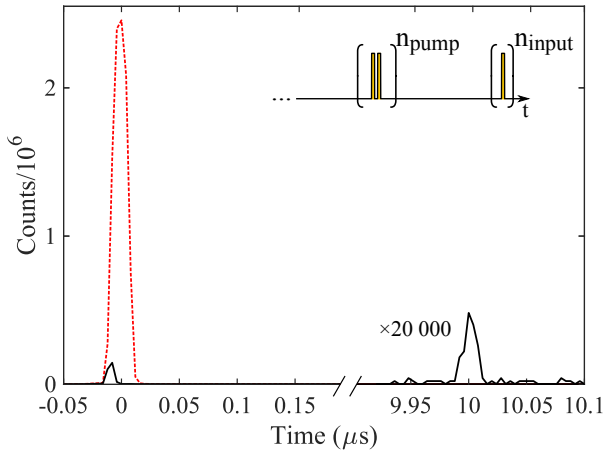

Figure 5.3: AFC storage for 10 μs in the nanobeam resonator (adapted from Ref. [30]). Red dashed line shows the input pulse. Black line shows the partially reflected input pulse and the output pulse (×20 000). The reflected input pulse appears small due to detector saturation. Inset shows a schematic of the pulse sequence following hyperfine initialization. Pairs of comb preparation pulses 10 μs apart were repeated n_{pump} = 10 000 times, followed by input pulses 20 ns wide, repeated n_{input} = 10 times.

in multiple frequency modes [97]. Multiplexing in time or frequency can significantly improve entanglement generation rates in quantum repeater networks [96]. An inhomogeneous linewidth of 150 MHz limits the bandwidth of storage in this system. Although there exist methods to increase this linewidth [18, 105], the bandwidth cannot be increased much further before being limited by overlapping optical transitions from other hyperfine levels.

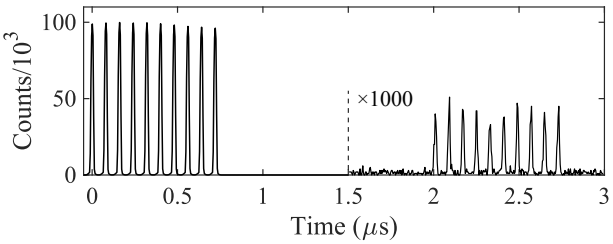

Figure 5.4: Multimode storage in the nanobeam resonator (adapted from Ref. [30]): ten 20 ns wide input pulses (reflection off cavity shown) and the corresponding 10 output pulses (×1000) from a Δ = 500 kHz AFC.

5.3 Coherent Storage of Time-Bin Qubits

In quantum storage protocols, the phase of the stored state must be preserved. A double AFC was used as an interferometer in order to characterize the coherence of the storage process [34]. Two overlapping AFCs with tooth spacing Δ_1, Δ_2 and with frequency detuning δ_1, δ_2, were created, as shown in Figure 5.5. The two combs lead to two output pulses for every input pulse, at times $\frac{1}{\Delta_1}, \frac{1}{\Delta_2}$. The two AFCs were created by alternately burning away population between the teeth of each comb. Low power burn pulses were used and the relative burn powers and number of repeats (n_{pump}) were calibrated such that the amplitudes of the two output pulses were maximized and equal to one another. The discrepancy between the data and the fit is in part due to photon counting uncertainty ($\sqrt{N_{counts}} \sim 350$), and in part due to superhyperfine side-hole and anti-hole structure (see Section 2.4).

For a given input pulse, the relative phase between the two output pulses ϕ_{rel} is given by:

$$\phi_{rel} = 2\pi \left(\frac{\delta_2}{\Delta_2} - \frac{\delta_1}{\Delta_1} \right), \tag{5.3}$$

where δ_1 (δ_2) is the detuning of the first (second) comb, measured relative to the frequency of the input pulse [4].

Next, we consider the case where a time bin qubit is stored by the double AFC. The input state is a superposition of weak coherent states $|\psi_{in}\rangle = \frac{1}{\sqrt{2}} (|\text{early}\rangle + |\text{late}\rangle)$, where the $|\text{early}\rangle$ pulse is absorbed at time t_{early}, and the $|\text{late}\rangle$ pulse is absorbed at time t_{late}. When absorbed by the double AFC, this input will be mapped to a total of four output pulses at times $(\frac{1}{\Delta_1} + t_{early})$, $(\frac{1}{\Delta_1} + t_{late})$, $(\frac{1}{\Delta_2} + t_{early})$, $(\frac{1}{\Delta_2} + t_{late})$. By appropriately selecting the time interval between the early and late input pulses, two of the four output pulses were made to overlap $(\frac{1}{\Delta_1} + t_{late} = \frac{1}{\Delta_2} + t_{early})$. Depending on ϕ_{rel}, these pulses either constructively or destructively interfered, as shown in the inset of Fig. 5.6. The double AFC therefore leads to a phase-dependent output amplitude, much like an interferometer.

Using an input state with mean photon number $\bar{n} = 0.6 \pm 0.09$ and sweeping ϕ_{rel} via the detuning δ_2, the interference fringe shown in Fig. 5.6 was obtained (see caption for details). The measured visibility of $91.2\% \pm 3.4\%$ demonstrates the high degree of coherence of this on-chip storage process. The visibility was limited by the 12 counts in the total destructive interference case $\left(\delta_2 = \frac{\Delta_2}{2} \rightarrow \phi_{rel} = \pi\right)$. These were due in part to imperfect cancellation of the two overlapping output pulses,

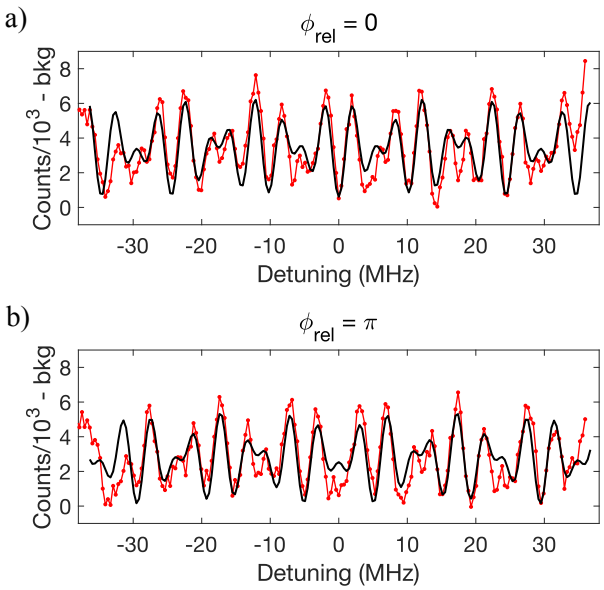

Figure 5.5: Double atomic frequency comb, measured by scanning the resonator reflection spectrum. Red circles with connecting lines represent counts with the minimum value subtracted. Black lines are fits to a sum of cosine functions: each of the two combs with finesse $F \sim 2$ is approximated by a cosine function. For both (a) and (b), $\Delta_1 = 5.0$ MHz, $\delta_1 = 0$ MHz, and $\Delta_2 = 3.4$ MHz. (a) $\delta_2 = 0 \rightarrow \phi_{\text{rel}} = 0$, (b) $\delta_2 = 0 \rightarrow \phi_{\text{rel}} = \pi$.

resulting from the slightly different efficiencies of storage in the two AFCs, and in part to a dark count rate of 18.5 Hz, leading to a baseline of 7 counts. The dark-count-subtracted visibility is 97.0% ± 3.6%.

[1]This value is corrected from Reference [30]

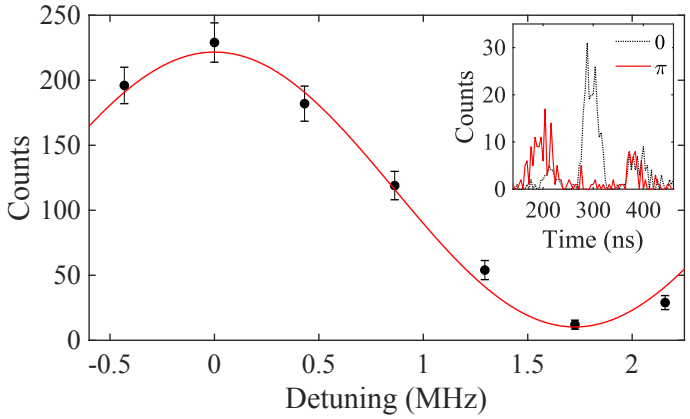

Figure 5.6: Coherent storage in the nanobeam resonator (adapted from Ref. [30]). Visbility curve was acquired using a double comb experiment with $\Delta_1 = 5.0$ MHz [1], $\Delta_2 = 3.4$ MHz, $\delta_1 = 0$ MHz. The detuning of the second comb was swept from $\delta_2 = -0.2$ MHz to $\delta_2 = 2.2$ MHz, and the intensity of the two central overlapping output pulses was measured. Black circles show the sum of counts in the overlapping pulse region with $\sqrt{N_{\text{counts}}}$ uncertainty bars. Red line shows a least squares fit to a sinusoid. Inset shows the four output pulses (middle two overlapping) in the case of the maximally constructive (dashed black line) and maximally destructive (solid red line) interference.

5.4 Estimating a Lower Bound on Storage Fidelity

In the absence of a single photon source, a lower bound on the storage fidelity of a single photon input state can be found using weak coherent states and decoy state analysis [68, 97]. Using this method, we estimated a lower bound for the fidelity of storing single photon time bin states, $F^{(n=1)} \geq 93.7\% \pm 2.4\%$, which exceeds the classical limit of $F = 2/3$.

In the decoy state method, a time bin state ψ with a mean photon number $\bar{n}$ is stored using the AFC protocol, and the fidelity $F_\psi^{(\bar{n})}$ of storage is measured as

$$F_\psi^{(\bar{n})} = \frac{N_\psi}{N_\psi + N_{\phi\perp\psi}}, \tag{5.4}$$

where N_ψ ($N_{\phi\perp\psi}$) is the number of photons measured in the output time bin corresponding to ψ ($\phi \perp \psi$), and $\phi \perp \psi$ denotes the state orthogonal to ψ. The gain of the output, $Q_\psi^{(\bar{n})}$ is also estimated using,

$$Q_\psi^{(\bar{n})} = N_\psi + N_{\phi\perp\psi}. \tag{5.5}$$

$F_{\psi}^{(\bar{n})}$ and $Q_{\psi}^{(\bar{n})}$ are measured for mean photon numbers $\bar{n}_1$ and $\bar{n}_2$, where $\bar{n}_1 < \bar{n}_2$, and $\bar{n}_2 < 1$.

The lower bound on the fidelity of storing a one-photon input state $F_{\psi}^{(n=1,L)}$ is then computed using:

$$F_{\psi}^{(n=1,L)} = 1 - \frac{E_{\psi}^{(\bar{n}_1)} Q^{(\bar{n}_1)} \exp \bar{n}_1 - E^{(0)} Y^{(0)}}{Y^{(n=1,L)} \bar{n}_1}, \tag{5.6}$$

where

$$E_{\psi}^{(\bar{n})} = 1 - F_{\psi}^{(\bar{n})} \tag{5.7}$$

is the error rate of storing a state ψ with mean photon number $\bar{n}$, and

$$Y^{(n=1,L)} = \max\left\{ Y^{(0)}, \frac{\bar{n}_2}{\bar{n}_2\bar{n}_1 - \bar{n}_1^2} \left(Q^{(\bar{n}_1)} e^{\bar{n}_1} - Q^{(\bar{n}_2)} e^{\bar{n}_2} \frac{\bar{n}_1^2}{\bar{n}_2^2} - \frac{\bar{n}_2^2 - \bar{n}_1^2}{\bar{n}_2^2} Y^{(0)} \right) \right\} \tag{5.8}$$

is the lower bound on the detection yield for the storage of a single photon state (see Reference [68]). $Y^{(0)} = Q^{(n=0)}$ is the yield when the input state is vacuum, equal to the dark counts in both output time bins. The superscripts denote photon number and whether the value is a lower bound (L). $E^{(0)} = E^{(n=0)}$ is the vacuum error rate, which is 0.5 by definition [68].

In order to obtain an average fidelity bound for all possible time bin states, the fidelities for storing time bin states $|\text{early}\rangle$, $|\text{late}\rangle$, $|+\rangle = \frac{|\text{early}\rangle + |\text{late}\rangle}{\sqrt{2}}$ and $|-\rangle = \frac{|\text{early}\rangle - |\text{late}\rangle}{\sqrt{2}}$ were measured for input photon numbers $\bar{n}_1 = 0.30$ and $\bar{n}_2 = 0.60$. The input pulses defining the $|\text{early}\rangle$ and $|\text{late}\rangle$ basis were 60 ns wide and 90 ns apart. A double AFC was used for measurements of all states with the memory times associated with the two combs being $t_1 = 200$ ns and $t_2 = 290$ ns [2], such that $t_2 - t_1 = 90$ ns. Figure 5.7 shows the input time bins centered at $t_{\text{early}} = 0$ ns and $t_{\text{late}} = 90$ ns, and the output time bins centered at 200 ns, 290 ns, and 380 ns. Of the three output time bins, the first and third were used for measuring F_{early} and F_{late}, while the second time bin was used for measuring F_+ and F_-, as shown in Figure 5.7.

Following Equation 5.6, $F_{+}^{(n=1,L)}$ was computed using:

$$F_{+}^{(n=1,L)} = 1 - \frac{E_{+}^{(\bar{n}_1)} Q_{+/-}^{(\bar{n}_1)} \exp \bar{n}_1 - E^{(0)} Y_{+/-}^{(0)}}{Y_{+/-}^{(n=1,L)} \bar{n}_1}, \tag{5.9}$$

[2] The t_1 and t_2 values are corrected from Reference [30]

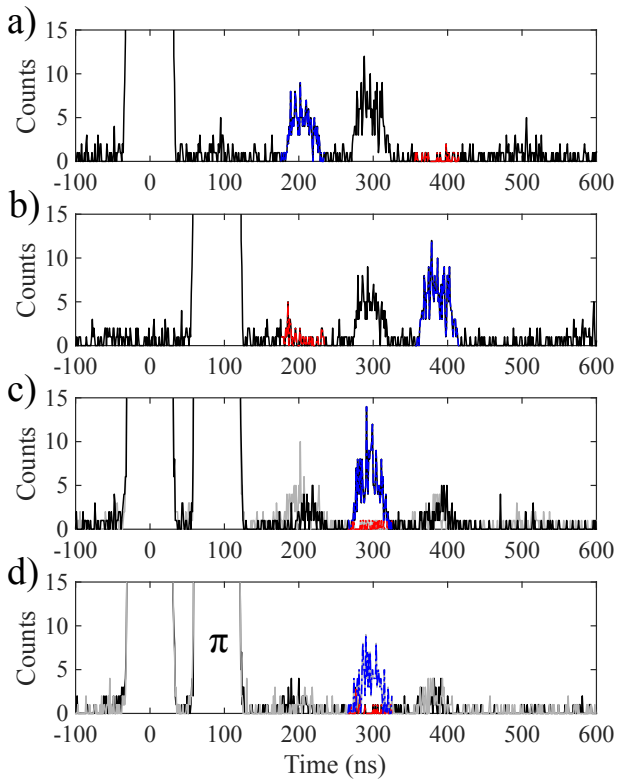

Figure 5.7: Part of the raw data used in the fidelity measurement. $\bar{n} = 0.6$ input (left, cut off) and output pulses from double comb. Input pulses are time bin states a) early, b) late, c) +, d) −. In all figures, blue (red) dash-dot line represents the 60 ns time bins counted as N_ψ ($N_{\phi\perp\psi}$). Time resolution is 1 ns. The same data set, shown in a) and b), was used for both the early and late fidelity calculations, since absolute time is irrelevant. In this data set, a small pulse 100 ns after the read pulse can be seen. The origin of this pulse was unclear, but it disappeared in the absence of the double comb. In c) and d), the black curve represents data taken with comb detunings $\delta_1 = \delta_2 = 0$ ($\phi_{\text{rel}} = 0$), while the gray curve represents data taken with $\delta_1 = 0$, $\delta_2 = \frac{\Delta_2}{2}$ ($\phi_{\text{rel}} = \pi$).

with similar equations for the other three states. $Q^{(\bar{n}_1)}_{+/-}$, $Y^{(0)}_{+/-}$, and $Y^{(n=1,L)}_{+/-}$ are averaged over the $|+\rangle$ and $|-\rangle$ fidelity measurements.

The lower bound on the fidelity of storing an arbitrary single photon state, $F^{(n=1,L)}_{\text{average}} = 93.7\% \pm 2.4\%$, was then computed as follows:

$$F^{(n=1,L)}_{\text{average}} = \frac{1}{3}\left(\frac{F^{(n=1,L)}_{\text{early}} + F^{(n=1,L)}_{\text{late}}}{2}\right) + \frac{2}{3}\left(\frac{F^{(n=1,L)}_{+} + F^{(n=1,L)}_{-}}{2}\right). \tag{5.10}$$

Table 5.1 summarizes the measured fidelity values for storing weak coherent states,

as well as the estimated single photon storage fidelities used in Equation 5.10. The uncertainties are calculated based on $\sqrt{N_{\text{photon}}}$ standard deviation on all N_ψ values due to Poissonian statistics of photon counting and the uncertainty, estimated to be 15%, of the mean input photon numbers, $\bar{n}$.

Input photon number	$\frac{1}{2}\left(F_{\text{early}}^{(\bar{n})} + F_{\text{late}}^{(\bar{n})}\right)$	$\frac{1}{2}\left(F_{+}^{(\bar{n})} + F_{-}^{(\bar{n})}\right)$
$\bar{n} = 0.60 \pm 0.09$	89.04% ± 1.34%	91.90% ± 1.32%
$\bar{n} = 0.30 \pm 0.05$	82.59% ± 1.80%	90.75% ± 1.84%
$n = 0$	50%	50%
	$\frac{1}{2}\left(F_{\text{early}}^{(n=1,L)} + F_{\text{late}}^{(n=1,L)}\right)$	$\frac{1}{2}\left(F_{+}^{(n=1,L)} + F_{-}^{(n=1,L)}\right)$
$n = 1$	89.85% ± 1.97%	95.59% ± 3.37%

Table 5.1: Storage fidelities in the nanobeam device.

Similar to the visibility curve discussed in Section 5.3, the measured fidelity was limited in part by dark counts and in part by the double comb protocol being an imperfect interferometer. The dark counts limited fidelity bound was estimated to be $\sim 96.5\%$.

5.5 Overcoming AFC Efficiency Limitation

While the storage presented here was limited in efficiency, a nanophotonic cavity coupled to $^{167}Er^{3+}$ ions in Y_2SiO_5 promises to be an efficient quantum storage system. The main limitations to the storage efficiency in this work were a low ensemble cooperativity of 0.3 and loss from the optical nanobeam cavity. The cooperativity can be increased using higher $^{167}Er^{3+}$ doping and better hyperfine initialization, which would require increasing the applied magnetic field [86] or changing its angle. A higher intrinsic quality factor resonator would serve to both increase cooperativity and decrease cavity loss. For example, using a Y_2SiO_5 crystal with 200 ppm $^{167}Er^{3+}$ doping, optimal hyperfine initialization, and a resonator with an intrinsic quality factor of 2×10^6, the theoretical efficiency of the AFC quantum storage is 90%. Mature silicon nanofabrication technology can be leveraged to achieve this goal by using a silicon resonator evanescently coupled to $^{167}Er^{3+}$ ions in Y_2SiO_5 [35, 79]. With this efficiency level and a storage time of 10 μs, the device would outperform a delay line composed of standard telecommunication fiber [29], an important benchmark on the way to achieving a quantum memory suitable for scalable quantum networks.

With the optical AFC protocol alone, it will be difficult to achieve efficient storage

for this duration due to superhyperfine coupling. However, the AFC spin-wave protocol, where the stored information is reversibly transferred from the optical to the hyperfine manifold [4], would enable storage longer than 10 μs without the same requirements for narrow spectral features, as well as enabling on-demand recall.

Following the analysis above, the subsequent set of devices, which are used in the next chapter (Chapter 6), used a higher doping of $^{167}Er^{3+}$ions, and resonators based on amorphous silicon waveguides on $^{167}Er^{3+}$:Y_2SiO_5. The storage of efficiency of those devices was also limited. Section 6.6 discusses a path to making devices with higher storage efficiency using the AFC protocol in more detail.

5.6 Nanobeam Device Temperature

Due to poor thermal conduction at low temperatures in insulating materials such as Y_2SiO_5 and the small cross section of the nanobeam, the device was warmer than its $\sim$ 25 mK surroundings when optical pulses were coupled in. The device temperature was estimated via the $^{167}Er^{3+}$ electron spin temperature [61], which was computed from the ratio between the lower and upper electron spin populations in the optical ground manifold using $\frac{N_{|\uparrow\rangle}}{N_{|\downarrow\rangle}} = e^{-\frac{\hbar\omega}{k_B T}}$.

Under an applied field of 380 mT parallel to D_1, the electron spin in the optical ground state was frozen for any temperature under $\sim$ 500 mK, enabling the long hyperfine lifetimes required for AFC storage. To be sensitive to lower temperatures, the electron spin population measurements were performed with a lower magnetic field of 110 mT (parallel to the D_1 axis of the crystal), leading to an electron Zeeman splitting of $\omega = 2\pi \times 23$ GHz, where the upper electron spin state had detectable population down to $\sim$ 250 mK. Because the Zeeman splitting was still considerably greater than the hyperfine splitting, one can consider two electron spin states, $|\downarrow\rangle$ and $|\uparrow\rangle$, each split into eight by the hyperfine interaction. The population in the two electron spin states was measured via the electron-spin-preserving optical transitions $|\downarrow\rangle$ to $|\downarrow\rangle$ and $|\uparrow\rangle$ to $|\uparrow\rangle$. The nanobeam was tuned such that these transitions were both resonant with the cavity, and photoluminescence (PL) was collected as a function of frequency, as shown in Fig. 5.8a. $N_{|\uparrow\rangle}/N_{|\downarrow\rangle}$ was extracted from the area ratio of the two transitions. Figure 5.8b shows the electron spin temperatures computed from these ratios for different dilution refrigerator temperatures. The inset in Fig. 5.8b shows the electron spin temperature measured under input power conditions identical to two experiments: 317 mK ± 49 mK for the T_2 measurement in the nanobeam (Fig. 2.3) and 413 mK ± 24 mK for the 165 ns storage experiment

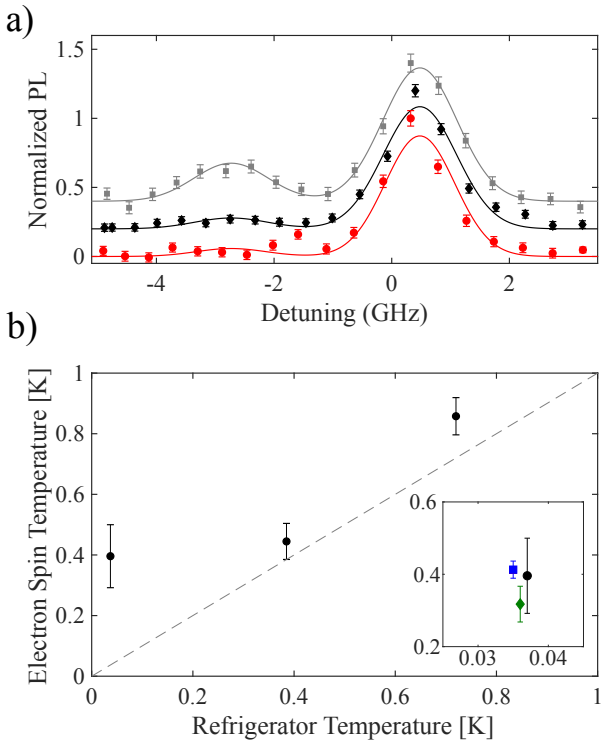

Figure 5.8: Nanobeam device temperature measurement (adapted from Ref. [30]). a) Photoluminescence (PL) from the nanobeam device as a function of detuning at three refrigerator temperatures: 720 mK (gray squares), 385 mK (black diamonds), 37 mK (red circles). Detuning was measured from 194810 ± 0.1 GHz. PL was collected after a 500 μs resonant pulse at 0.3 pW (estimated power in nanobeam). Background counts were subtracted, and each curve was normalized and offset for clarity. Solid lines are fits to a sum of two Gaussians with equal widths and center frequencies 3.2 GHz apart. The $|\downarrow\rangle$ to $|\downarrow\rangle$ transition is at the higher frequency. b) Electron spin temperatures (EST) computed from the PL data in (a), as a function of refrigerator temperature. Dashed gray line indicates where the two temperatures are equal. The inset shows a closeup of the EST measurement at 37 mK (black circle), the EST estimated during the T_2 measurement (green diamond), and the 165 ns storage experiment (blue square). To estimate the latter two temperatures, the same pattern of laser pulses as in the actual experiments was sent to the nanobeam, at 0.3 nW and 0.02 nW, respectively, and PL was collected after the pulses. Error bars are propagated standard deviations from photon counting ($\sqrt{N_{\text{counts}}}$). In all measurements, the laser frequency was slowly modulated within each optical transition to prevent hyperfine holeburning.

in Fig. 5.2. Assuming the electron spin was in thermal equilibrium with the device, we therefore estimated the temperature of our device during experiments to be ~400 mK.

Chapter 6

DYNAMIC ON-CHIP CONTROL OF STORED LIGHT USING THE DC STARK SHIFT

In this chapter, we use on-chip electrodes to realize a new multifunctional device which can not only store light, but also modify its frequency and bandwidth. The ability to adjust the temporal profile or frequency of stored light can be useful when quantum memories act as interfaces between multiple emitters, as in a quantum repeater network. We demonstrate dynamic control of memory time in a digital fashion with storage times from 50 ns to 400 ns. By shifting the frequency of the $^{167}Er^{3+}$ ions during emission, we change the frequency of stored light by ±20 MHz relative to the input frequency. Using a quadrupole electrode configuration, the bandwidth of stored light is increased by over a factor of three, from 5.7 MHz (input) to 18 MHz (output).

The quantum memory protocol used in this chapter is atomic frequency comb with added dynamic control. The dynamic control is enabled by the optical DC Stark shift. When a rare earth ion in a crystal interacts with a DC electric field $\vec{E}$, the optical transition frequency changes according to:

$$\delta f = -\frac{1}{h}\,\vec{\delta\mu}\cdot\hat{L}\cdot\vec{E}, \tag{6.1}$$

where $\hat{L}$ is the local field correction tensor and $\vec{\delta\mu} = \vec{\mu}_e - \vec{\mu}_g$ is the difference between the electric permanent dipole moments in the optical excited state ($\vec{\mu}_e$) and optical ground state ($\vec{\mu}_g$) [69]. For a non-centrosymmetric site such as the yttrium sites in Y_2SiO_5 for which Er^{3+} ions substitute, the above linear stark shift term dominates, although a quadratic Stark shift term also exists.

A DC Stark shift enables dynamic control of light stored in an AFC by allowing changes to the optical transition frequency of each ion in the excited Dicke state [4]. Modifying Equation 3.3 from Section 3.1, we can see the effect of this dynamic control:

$$|\Psi\rangle = \sum_{j=1}^{N} c_j\, e^{i\left(\omega_j + 2\pi\,\delta f_j(t)\right)t}\, e^{-ik\vec{r}_j}\,\left|0\ldots1_j\ldots0_N\right\rangle. \tag{6.2}$$

The Stark shift of each ion $\delta f_j(t)$ can be varied over time by applying a slowly varying electric field, where slow is defined relative to optical frequencies. In this section, we use the electrodes described in Section 4.3 to control the frequencies of $^{167}Er^{3+}$:Y_2SiO_5 ions. The DC Stark shift can be the same for all ions, as when electrodes are biased in a parallel configuration, or different for every ion, as when electrodes are biased in a quadrupole configuration.

Section 6.1 discusses the Stark shift in $^{167}Er^{3+}$:Y_2SiO_5. Sections 6.2-6.4 show three different ways in which Stark shift control can be used to improve and add functionality to an atomic frequency comb storage protocol. Section 6.5 includes some supporting experiments for this chapter. Lastly, Section 6.6 describes strategies for improving the efficiency of storage in the devices used in this chapter.

For all experiments conducted in this chapter, the temperature of the mixing chamber plate to which the sample was attached was $\sim$ 70 mK. A magnetic field of 0.98 T parallel to the D_1 axis of the Y_2SiO_5 crystal was applied with a solenoid superconducting electromagnet. Any magnetic field along the crystal b axis was cancelled using a set of trim-coils on either side of the solenoid. For more details of the experimental setup, see Appendix D. All experiments are performed on crystallographic site 2 of $^{167}Er^{3+}$:Y_2SiO_5, which has a zero field optical transition frequency at 194756 GHz ($\lambda_\circ$ = 1538.85 nm).

6.1 DC Stark Shift in $^{167}Er^{3+}$:Y_2SiO_5

The DC Stark shift described in Equation 6.1 is dependent on the orientation of the applied field relative to $\vec{\delta\mu}$ [42]. Without knowing $\vec{\delta\mu}$ or $\hat{L}$, it is possible to empirically characterize the Stark shift induced by an electric field applied in a particular direction using the stark shift parameter $s_{\hat{n}}$, where $\hat{n}$ specifies the direction:

$$\delta f = s_{\hat{n}} E_{\hat{n}}. \tag{6.3}$$

As introduced in Section 2.1 there are four subclasses of $^{167}Er^{3+}$:Y_2SiO_5 sites with different orientations for each crystallographic site. Focusing on site 2, this means that there are four different orientations for $\vec{\delta\mu}$. Therefore, in an ensemble of $^{167}Er^{3+}$:Y_2SiO_5 ions, four different Stark shifts will be observed for an electric field applied in an arbitrary direction. When the applied electric field is parallel or perpendicular to the b axis, the Stark shifts of the four subclasses are pair-wise degenerate, such that there are only two equal and opposite DC Stark shifts $\delta f_\pm$ =

$\pm sE$. In this thesis, all electric fields are applied either parallel or perpendicular to the b axis, so from here on, I will refer to two $^{167}Er^{3+}$ subclasses for simplicity.

The Stark shift for $^{167}Er^{3+}$:Y_2SiO_5 was estimated using holeburning spectroscopy in an ensemble of ions coupled to a hybrid αSi-$^{167}Er^{3+}$:Y_2SiO_5 resonator, for electric fields parallel to the crystal b and D_2 axes. For this measurement, on-chip parallel plate electrodes on either side of the resonator were used to apply a homogeneous electric field to all ions. These electrodes were comprised of two gold rectangles on either side of the resonator (not the electrode geometry described in Section 4.3). The rectangular electrodes were much longer than the resonator (300 μm). The distance between the electrodes was 90 μm (b measurement) or 20 μm (D_2 measurement).

To measure the Stark shift, a spectral hole was first burned in the $^{167}Er^{3+}$:Y_2SiO_5 ensemble using a long laser pulse. After a wait time of 10 ms, the hole and surrounding inhomogeneous line were scanned in frequency space using the laser piezo drive. A constant electric field was applied during the scan. Figure 6.1a shows the scans of the spectral hole as a function of the electric field applied parallel to the b axis of Y_2SiO_5. As the field increases, the spectral hole splits into two holes corresponding to the two subclasses.

Figure 6.1b shows the central frequency of each hole as a function of applied electric field for fields oriented parallel to the b and D_2 crystal axes. By fitting $\delta f_{\pm} = \pm s_x E_x$, where x is a crystal axis direction, to the centers of the holes, the Stark shift parameter was estimated to be $s_b = 15.0 \pm 0.9$ kHz/(V/cm) for electric fields applied parallel to the b axis, and $s_{D_2} = 3.0 \pm 0.3$ kHz/(V/cm) for electric fields applied parallel to the D_2 axis. Two separate devices were used in these measurements. The error bars are 95% confidence intervals from the line fit to the data, and do no take into account any misalignment of the resonator/electrode pattern to the crystal axes, which we estimate to be $\lesssim 5°$. The misalignment of the electrodes to the resonator is limited by the precision of the electron beam aligned write and is less than $0.1°$. The measured DC Stark shift is also dependent on our calibration of the electric field applied to the ions. For this calibration, the average electric field applied along the resonator for a given bias on the electrodes was simulated in COMSOL as in Chapter 4.3. The bias applied to the electrodes by the function generator was measured assuming a high impedance load, because the electrodes act as open circuits for DC signals.

For the experiments described in the rest of this chapter, we used a hybrid αSi-$^{167}Er^{3+}$:Y_2SiO_5 resonator with the electrodes described in Section 4.3. The elec-

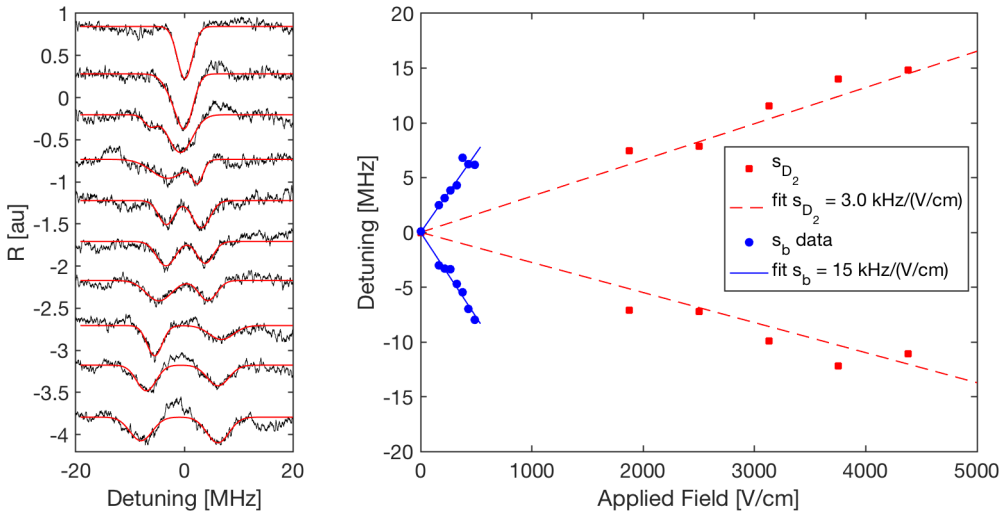

(a) (b)

Figure 6.1: Stark shift measurement for electric fields aligned to b and D_2 axes in $^{167}Er^{3+}$:Y_2SiO_5. (a) Holeburning spectra with different electric field applied along the crystal b axis. Red lines are double Gaussian fits to the holes. (b) Linear fit to the centers of spectral holes as a function of applied electric field along the D_2 (red) and b (blue) axes.

trodes and resonator were aligned such that the applied electric field $E_y(x)$ was parallel to the b-axis of the Y_2SiO_5 crystal. Using a similar procedure to the hole-burning experiment described above, with the electrodes being biased in a parallel (homogeneous field) configuration, the Stark shift parameter in this device was measured to be $s_b = 11.6 \pm 0.2$ kHz/(V/cm). There is a difference of $\sim 30\%$ between this s_b value and the value measured with the parallel electrodes ($s_b = 15$ kHz/(V/cm)). As this device was on a different Y_2SiO_5 substrate than the parallel plate device used to measure the Stark shift s_b above, it is possible that the difference in these two values is due to a difference in alignment of electrodes to crystal axes.

6.2 Dynamic Control of Storage Time

An electric field can be used to control the storage time of an atomic frequency comb memory by preventing emission during an AFC rephasing event using electric-field-induced dephasing, then reversing the electric field to emit on a subsequent AFC rephasing. Similar protocols have been used in rare-earth ion doped crystals, using optical [64] and spin [7] transitions.

The pulse sequence used to achieve dynamic control of AFC storage is shown in Figure 6.2. Not shown in the figure is the hyperfine initialization, which is performed

before every experiment (see Section 2.3). First, an AFC with periodicity Δ is created using spectral holeburning (see Section 3.1). The comb burning step is repeated n_{comb} times. A sketch of the comb is shown above the pulse sequence. After waiting tens of milliseconds until photoluminescence from comb creation is mostly gone, an input pulse is sent into the resonator, as shown by the red square pulse. Shown in light red are possible emissions corresponding to rephasing events of the AFC at times $t = \frac{m}{\Delta}$, where m is an integer. Without electric field control, the largest emission, which we consider the output of the memory, would be at $t = \frac{1}{\Delta}$ ($m = 1$). The figure shows instead an emission at $t = \frac{3}{\Delta}$ ($m = 3$) in red. The choice of time bin in which emission occurs is enabled by two equal and opposite electric field pulses, one before $t = \frac{1}{\Delta}$, and one immediately before the desired emission.

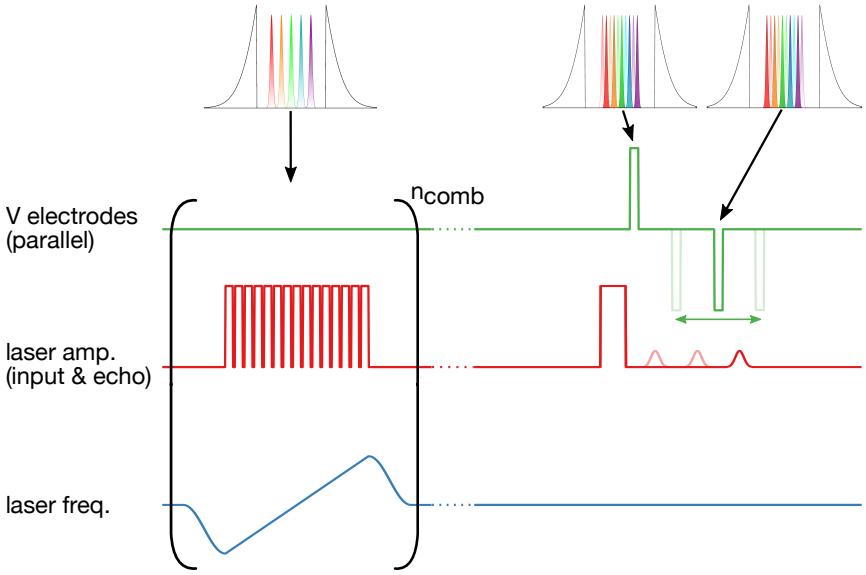

Figure 6.2: Schematic representation of a digital storage time AFC experiment (pulse sequence not to scale). The x-axis represents time. Sequence is described in main text.

The sketches of the comb indicate the effect of the two electrical pulses. Here the electrodes are biased in a parallel configuration, so we can assume all $^{167}Er^{3+}$ions experience roughly the same electric field. There are two subclasses of $^{167}Er^{3+}$ ions which experience an equal and opposite frequency shift when an electric field is applied: $\delta f_{\pm} = \pm s \cdot E$ (see Section 6.1). The combs above the electrical pulses in Fig. 6.2 illustrate the subclass splitting. During the an electric pulse, the phase accumulated by the two subclasses of ions in the rotating frame is $\phi_{\pm} = 2\pi t_{\text{pulse}} \delta f_{\pm} = \pm 2\pi \delta t_{\text{pulse}} sE$. For the first electrical pulse, the "killing" pulse, the values of δt_{pulse} and E are chosen such that the difference in phase accumulated

by the two subclasses of ions is $\delta\phi = \phi_+ - \phi_- = \pi$. A π phase shift between two ensembles of excited ions in a spectral comb leads to a suppression of emission at the time of AFC rephasing [30, 34]. This condition continues until the phase difference is eliminated, preventing emission for any AFC rephasing event. The second pulse, the "reviving pulse" is equal in time, but opposite in electric field, such that the new accumulated phase difference $\delta\phi = -\pi$ cancels out the first. The first AFC rephasing to follow the reviving electrical pulse will therefore lead to the emission of stored light. By choosing the location in time of the second pulse, the memory time can therefore be dynamically set to be any integer multiple of $\frac{1}{\Delta}$.

As shown in Figure 6.3, digitally controlled AFC storage was demonstrated using the protocol described in Fig. 6.2. Figure 6.3a shows the atomic frequency comb with periodicity $\Delta = 20$ MHz (measured 19.7 ± 0.1 MHz), which will lead to a rephasing event every $t = \frac{1}{\Delta} = 50$ ns. The teeth of the comb are each fit to a Gaussian function. The amplitude and background of each tooth is fit individually, while the tooth width γ and period Δ are parameters common to all fits. The finesse of the comb $F = \frac{\Delta}{\gamma}$ is estimated from the fit to be $F = 7.22 \pm 0.49$ ($\gamma = 2.7$ MHz). This is likely an underestimate of the true finesse value due to a scan power that was too large. When scanning the comb, population can be removed from the tops of the teeth, leading to an artificially small finesse measurement. For example, the dotted gray line in Fig. 6.3a shows the same comb but with a finesse of $F = 12.2$ ($\gamma = 1.6$ MHz, discussion on Fig. 6.3c explains the choice of 12.2).

Figure 6.3b shows the partly reflected input and the output for various values of m. We consider the largest output pulse on each line (in blue) to be the memory output. The first electric pulse was a 10 ns long pulse with amplitude 2.0 kV/cm centered at 25 ns. The second electric pulse was 10 ns long with an opposite amplitude of -2.0 kV/cm, and its center position was varied as $t_{\text{pulse}\,2} = 25\text{ ns} + (m-1) \times 50\text{ ns}$ to allow the emission at $t = \frac{m}{\Delta}$. For the $m = 1$ case, there were no electric pulses applied. As this figure shows, the memory time can be dynamically controlled in a digital fashion, $t_{\text{memory}} = \frac{m}{\Delta}$ by choosing the position of the second electric pulse.

The presence of multiple smaller pulses following the first and largest output pulse is a feature of the high finesse and low efficiency of the memory. Following Reference [3], and using the notation from Section 3.2, the amplitude of the first output pulse from an AFC memory is:

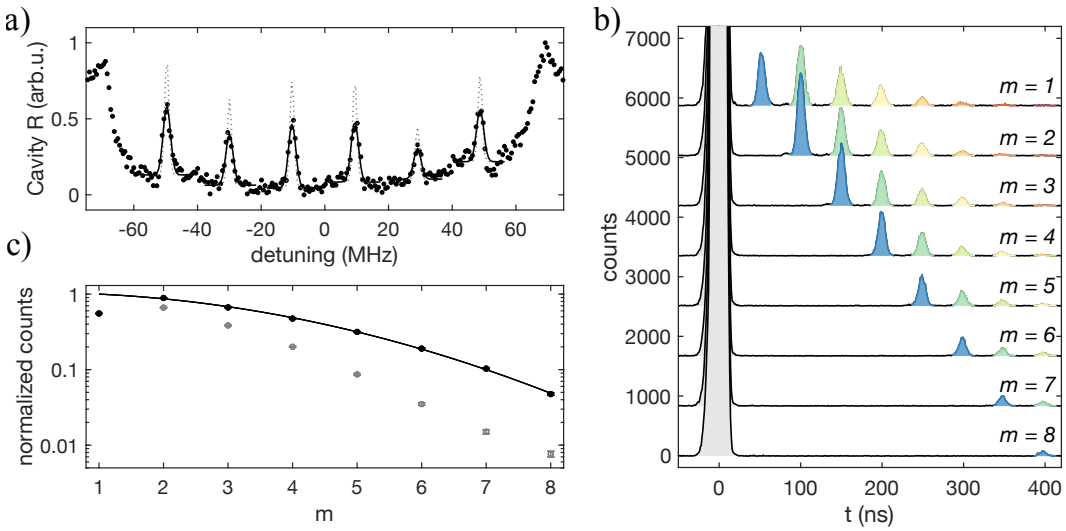

Figure 6.3: Digitally controlled storage time in hybrid αSi-$^{167}Er^{3+}$:Y_2SiO_5 resonator. (a) Atomic frequency comb used in this experiment. The comb is created as in the first part of Fig. 6.2, then scanned by slowly varying the frequency of the laser using the piezo drive. Circles are data points, solid black lines are Gaussian fits ($\Delta = 19.7$ MHz, $\gamma = 2.7$ MHz). Dotted gray line shows curves with the same fit parameters, except for a narrower tooth width, $\gamma = 1.6$ MHz. Detuning is measured from 194822 GHz. (b) Storage and emission of light at different times $t_{\text{memory}} = \frac{m}{\Delta}$. Partly reflected input pulse is shown in grey; memory output is shown in blue. Subsequent emissions (green to red) are discussed in the main text. (c) Energy emitted in output pulse for each value of m. Black data points represent the total counts in the $t = \frac{m}{\Delta}$ time bin when all previous emissions are suppressed (blue output pulses in (b)). Grey data points represent total counts in the $t = \frac{m}{\Delta}$ time bin when previous emissions are not suppressed (blue-red pulses on line "$m = 1$" in (b)). Error bars represent $\sqrt{N_{\text{counts}}}$. Solid line is the theoretical dephasing function for a comb with Gaussian teeth, fitting only to the comb finesse.

$$\mathcal{E}_{\text{out}}\left(t = \frac{1}{\Delta}\right) = -\frac{\kappa_{\text{in}}}{\kappa}\frac{4C'}{(1+C')^2}\exp\left(-\frac{\pi^2}{4\ln 2}\frac{1}{F^2}\right)\mathcal{E}_{\text{in}}\left(t=0\right). \tag{6.4}$$

Any subsequent emission will depend on both the input pulse amplitude and the amplitude of preceding emissions. For example, the amplitude of the second emission is [31]:

$$\begin{aligned}\mathcal{E}_{\text{out}}\left(t = \frac{2}{\Delta}\right) = &-\frac{\kappa_{\text{in}}}{\kappa}\frac{4C'}{(1+C')^2}\exp\left(-\frac{\pi^2}{4\ln 2}\frac{2^2}{F^2}\right)\mathcal{E}_{\text{in}}\left(t=0\right)\\ &+\frac{\kappa_{\text{in}}}{\kappa}\frac{8C'^2}{(1+C')^3}\exp\left(-\frac{\pi^2}{4\ln 2}\frac{2}{F^2}\right)\mathcal{E}_{\text{in}}\left(t=0\right).\end{aligned} \tag{6.5}$$

The first term in Eq. 6.5 corresponds to the rephasing of the input at $t = 0$. This term is similar to Eq. 6.4 for the first emission, with the exception of the exponential dephasing term, which now has a factor of 2^2 because the time between input in rephasing is twice as long. The second term in Eq. 6.5 corresponds to light that is absorbed at $t = 0$, emitted and reabsorbed during the first rephasing at $t = \frac{1}{\Delta}$, then emitted again at $t = \frac{2}{\Delta}$ [31]. Because of the opposite sign between the two terms, the second emission becomes smaller as the first emission becomes larger. In the case of an impedance matched memory ($C' \rightarrow 1$) and a high finesse ($F \rightarrow \infty$), the two terms are equal and opposite and the emission at $t = \frac{2}{\Delta}$ is suppressed entirely. This holds also for subsequent emissions at $t = \frac{m}{\Delta}$. Therefore, for a highly efficient, impedance matched quantum memory, only one emission at $t = \frac{1}{\Delta}$ is present. Using electric pulses, this single emission can be moved to any position $t = \frac{m}{\Delta}$.

If all previous emissions are efficiently suppressed by electric-field induced dephasing, the efficiency of the m^{th} emission is limited by the comb finesse, as indicated by the dephasing term in Equation 6.6 [64]:

$$\eta_{\mathrm{AFC},m}\left(t = \frac{m}{\Delta}\right) = \frac{\kappa_{\mathrm{in}}}{\kappa}\frac{4C'}{(1+C')^2}\exp\left(-\frac{\pi^2}{2\ln 2}\frac{m^2}{F^2}\right). \tag{6.6}$$

Figure 6.3c shows the energy emitted in the m^{th} time bin for $t_{\mathrm{memory}} = \frac{m}{\Delta}$. This corresponds to the total counts in the blue pulses in each curve in Fig. 6.3b. The data is fit using the dephasing term from Eq. 6.6: $\exp\left(-\frac{\pi^2}{2\ln 2}\frac{m^2}{F^2}\right)$, since the impedance matching prefactor will be identical given the same resonator and spectral comb. The $m = 1$ data point is excluded from the fit. This data point is believed to be smaller than expected due to the $\sim$ 100 ns dead time of the SNSPD detector after the input pulse. A comb finesse of $F = 12.2 \pm 0.2$ ($\gamma = 1.6$ MHz) is extracted from this fit. With this finesse, the $1/e$ point for digital storage time is 200 ns ($m = 4$). To improve on this storage time, the finesse must be increased while keeping the comb period Δ the same, meaning a decrease in tooth width γ. This is not possible for this current material due to superhyperfine broadening (see Section 2.4). The grey data points in Fig. 6.3c show the total counts in the m^{th} time bin when the previous output pulses are not suppressed using electric pulses. This data is included to clearly indicate that the m^{th} pulse is larger if previous emissions are suppressed.

Calibrating Electric Pulses

The measured Stark shift can be used to determine the amplitude and length of electric field pulses needed to kill and revive emission in this protocol: $E_{\mathrm{kill}} = \frac{\phi_{\mathrm{kill}}}{4\pi s \delta t_{\mathrm{pulse}}} =$

$\frac{1}{4s\delta t_{\text{pulse}}}$. In this device, the Stark shift was measured to be 11.6 kHz/(V/cm), so for a 20 ns pulse, the $E_{\text{kill}} = (-E_{\text{revive}}) = 1.1$ kV/cm. To confirm this, a calibration curve was obtained, as shown in Figure 6.4. To acquire this curve, an AFC was created, and an electrical pulse with a fixed time of 20 ns but varying amplitude was placed between the optical input pulse and the first AFC rephasing at $t = \frac{1}{\Delta}$. The sum of counts in the output time bin at $t = \frac{1}{\Delta}$ was measured. As the electric field amplitude is varied, the relative phase shift between the subclasses $\delta\phi$ changes, leading to a sinusoidal variation in the output pulse. The minimum output counts were found to be at 4.3 Vpp, corresponding to 0.96 kV/cm. The discrepancy between this value and the expected value of 1.1 kV/cm is thought to be due to imperfect pulse-width control and frequency dependent power transmission through the transmission chain from the function generator to electrodes. Note that for a field of 2×0.96 kV/cm, corresponding to a phase difference of 2π, the output emission is again maximized, although the amplitude is lower than the zero-field case. This is because of spatial inhomogeneity in the electric field, which means not all ions can experience a $\pm\pi$ phase shift for the same electric pulse. A similar calibration was performed for the 10 ns pulses used in Figure 6.3.

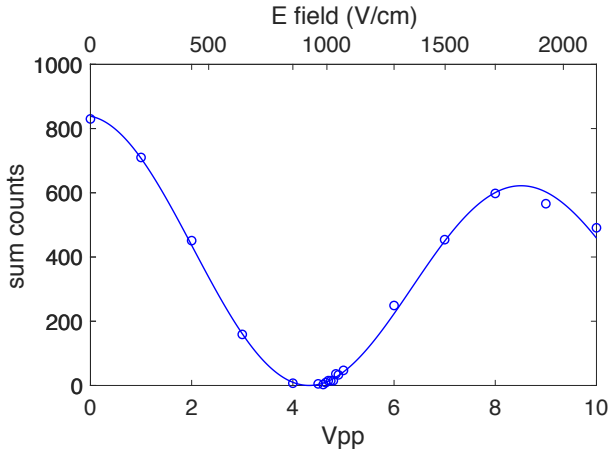

Figure 6.4: Calibrating the amplitude of "killing" or "reviving" pulses in a parallel configuration of the quadrupole/parallel electrodes. Pulses are rectangular with width 20 ns, inserted between the input and first emission of an AFC experiment. Data points are sum counts in a time bin centered at $t = \frac{1}{\Delta}$. Solid line is a fit to a cosine function multiplied by an exponential decay.

6.3 Frequency Shifting

With DC Stark shift control, the frequency of light stored in an AFC can be dynamically modified during emission. This is achieved using the same αSi-$^{167}Er^{3+}$:Y_2SiO_5

device with electrodes (see Section 4.3), and biasing the electrodes in the parallel configuration, such that the atomic frequency comb is shifted in frequency during the emission of a pulse. This requires that one of the two inequivalent $^{167}Er^{3+}$ subclasses (see Section 6.1) be eliminated from the spectral window, leaving only ions which experience a positive start shift, $\delta f_+ = +s_b E$. The choice of subclass with positive versus negative Stark shift is arbitrary.

Figure 6.5 shows a schematic of the frequency shift protocol. A two-part comb burning procedure is used to eliminate one of the two subclasses of $^{167}Er^{3+}$ ions. With the first burning step, a normal AFC containing both subclasses is created, shown in the sketch above the pulse sequence. The center frequency of this comb is defined as $f_{\text{comb}} = 0$. For the second burning step, the two subclasses are split using a parallel electric field. Specifically, an electric field is chosen such that $\delta f_\pm = \pm\Delta/4$, where Δ is the period of the comb. The frequency offset between the two subclasses is therefore $\Delta/2$, which allows optimal burning of just one subclass as it leads to the maximum splitting between the teeth of two combs with period Δ. The second burn step uses the same laser pulses as for the first comb, but this time centered around $f_{\text{comb}} = \Delta/4$, which allows ions with a positive shift $\delta f_+ = +sE$ to remain, and burns away ions with a negative shift $\delta f_- = -sE$. When the electric field is turned off, what remains is an AFC centered at $f_{\text{comb}} = 0$ with only one subclass. As shown in the sketch above the pulse sequence, this comb has half the amplitude of a normal AFC, since it contains half the ions.

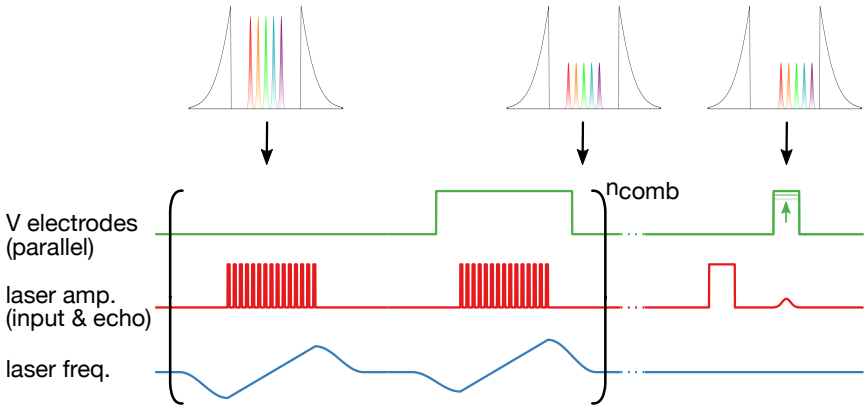

Figure 6.5: Schematic representation of a frequency shifting AFC experiment (pulse sequence not to scale). The x-axis represents time. Sequence is described in main text.

After waiting for tens of milliseconds for any photoluminescence from the comb burning to be gone, a read pulse is sent in with frequency $f_{\text{input}} = f_{\text{comb}} = 0$, as

shown on the right side of Fig. 6.5. The rephasing of the AFC causes an emission at $t = \frac{1}{\Delta}$. During this emission, an electric field pulse with amplitude E_{pulse} applied in the parallel configuration will lead to a uniform shift of all ion frequencies, as shown in the comb schematic above the pulse sequence. The ions will emit at a frequency $f_{\text{output}} = f_{\text{comb}} = +s \cdot E_{\text{pulse}}$.

Figure 6.6 shows frequency shifting of light stored with an AFC. The AFC had a width of 72.5 MHz, a finesse of $F \sim 2$, and a period $\Delta = 5$ MHz, leading to a storage time of $t = \frac{1}{\Delta} = 200$ ns. To detect the frequency shift of the output, a heterodyne measurement is used. The AFC output pulse was beat with a local oscillator with $\Delta f_{\text{heterodyne}} = 100$ MHz and measured, then a Fourier transform was performed on the data and 100 MHz was subtracted from the x-axis (see Appendix D).

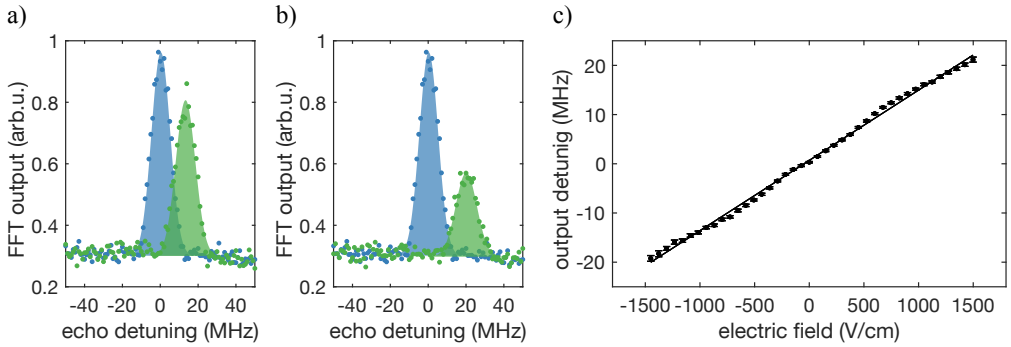

Figure 6.6: AFC storage with frequency shift in hybrid αSi-$^{167}Er^{3+}$:Y_2SiO_5 resonator. (a-b) Two examples of AFC output pulses without (blue) and with (green) a frequency shift. Filled in area is a Gaussian fit to the data; circles represent data points. (a) A frequency shift of 13 MHz. (b) A frequency shift of 20 MHz. (c) The frequency of AFC emission as a function of electric field applied during emission. Circles are the centers of the Gaussian fits shown in (a-b), error bars are 95% confidence intervals for those fits. The solid line is a linear fit to the data, yielding a slope of $m = 14.3$ kHz/(V/cm).

Figures 6.6a-b show an AFC output pulse with and without frequency shifting. Figure 6.6c shows the trend of output frequency versus E_{pulse}. The solid line is a linear fit to the data. The slope of $m = 14.3$ kHz/(V/cm) does not exactly match the 11.6 kHz/(V/cm) DC Stark shift estimated in this device. The source of error is likely our calibration of the electric field (x-axis in Fig. 6.6c). In this experiment, the electric pulses were distorted, meaning they were not constant over the entire output pulse. The cause of this distortion is known: the DC coupled power splitter we used between the function generator and electrodes, combined with the impedance mismatch between the source and electrodes, led to many reflections of the electric

pulses. This was an issue for the frequency splitting experiment only.

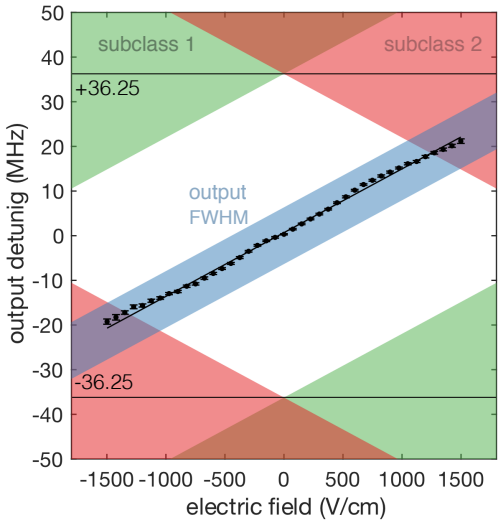

Figure 6.7: Frequency shift versus applied field in the experiment from Fig. 6.6. This figure explains one of the reasons for a decreased output amplitude at high fields. In addition to the curve from Fig. 6.6c, there are four sets of bands. The central blue band shows the expected frequency shift of the output pulse (or, equivalently, the ions which absorbed the input pulse). The extent of this band represents the FWHM of the input and output pulses. The green bands sloping upward represent ions outside of the comb width of 72.5 MHz, which have not been initialized into a comb. The red bands sloping downwards are ions of the second subclass, which also have not been initialized into a comb. These ions experience the opposite frequency shift $\delta f_{-} = -m \cdot E_{\text{pulse}}$. At the highest fields (positive or negative), the comb ions that absorbed the input pulse are overlapping with background ions of the second subclass. This would lead to partial absorption of the output pulse by the second subclass of ions, and therefore a decreased storage efficiency.

The decrease in output amplitude with frequency shift that is evident in Figures 6.6a-b is still under investigation. We believe there are three reasons for the decrease in efficiency with increasing frequency shift: (1) imperfect removal of the second subclass of ions from the comb, (2) overlap with the ions of the second subclass on either side of the comb (see Fig. 6.7), and (3) electric pulses varying in time (due to distortion) leading to a time-varying frequency shift. Simulations (method discussed in Section 6.4) confirmed that both (1) and (2) lead to a decrease in AFC output pulse for a nonzero frequency shift. All of these limitations are surmountable. Frequency shifting experiments with improved subclass elimination and larger comb bandwidths would elucidate if there are any other effects leading to a decreased output amplitude with frequency shift.

6.4 Bandwidth Broadening

The DC Stark shift enables dynamic control over the bandwidth of stored pulses. The bandwidth of emitted pulses is proportional to the bandwidth of ions storing the excitation, which can be modified using an electric field that varies across the ion ensemble.

Figure 6.8 shows a schematic of a bandwidth broadening experiment. In the first part of the sequence, a normal AFC is created (see Section 3.1). Next, after waiting tens of milliseconds, an input pulse is sent into the device and an AFC rephasing leads to an output pulse at $t = \frac{1}{\Delta}$. Electric pulses are applied during the input and output optical pulses, and also during the wait time, with the electrodes biased in a quadrupole configuration (see Section 4.3). The electric pulse during the input optical pulse slightly broadens the distribution of ions comprising the comb, as shown in the sketch above the pulse sequence. With quadrupole biasing, each ion along the resonator's ~ 100 μm length experiences a different electric field, which causes the ion distribution to broaden. The second electric pulse is used to optimize the electric field rephasing for this protocol, which will be explained in more detail shortly. During the optical output pulse, the third and most important electric pulse broadens the comb. The higher the amplitude of this electric pulse, the broader the ion distribution during emission. When the broadened ions emit the output pulse, the optical pulse will be broader in frequency, and therefore narrower in the time domain, as indicated in the optical trace of the pulse sequence.

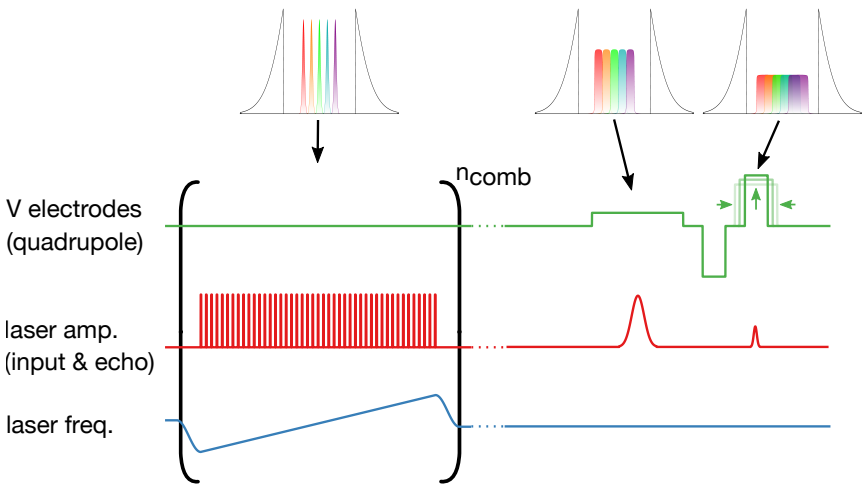

Figure 6.8: Schematic representation of bandwidth broadening AFC experiment (pulse sequence not to scale). The x-axis represents time. Sequence is described in main text.

The reason there are three electric pulses is to ensure proper rephasing of the ensemble. To explain this, we will go through the case where there is only one electric pulse, two electric pulses, and finally three electric pulses.

1. One electric pulse: To broaden the ion distribution during emission, only the electric pulse at $t = \frac{1}{\Delta}$ is needed. However, if there is only one electric pulse, the erbium ensemble would not successfully rephase at $t = \frac{1}{\Delta}$ and the emission would be suppressed, since the electric field gradient leads each ion in the ensemble to accumulate a different phase.

2. Two electric pulses: To compensate for the dephasing caused by the electric field gradient, an electric pulse with an equal and opposite area could be used during absorption, at $t = 0$. Then the phase accumulated by each ion due to the electric field during the pulse at $t = 0$, would be cancelled out by the phase accumulated during the second electric pulse at $t = \frac{1}{\Delta}$. There is one complication with this method: when an optical pulse is emitted by an AFC, the temporal profile of the output pulse is identical to the input. AFC storage is therefore called a first-in-first-out protocol [101]. Conversely, rephasing that happens as a result of two equal and opposite gradient electric fields leads to a reversal of the temporal profile of the stored pulse. Protocols that use only reversal of electric field gradients such as CRIB, are therefore first-in-last-out protocols [51]. Since, in the current situation, we require both electric field gradient and AFC rephasing to occur at the same time, this leads to a loss of efficiency, as the temporal profile of the stored pulse cannot be both reversed and not reversed anywhere except at its center.

3. Three pulses: To solve this problem, we need the rephasing due to the electric field gradient to occur such that the output pulse profile is first-in-first-out. This can be done by using three electric pulses with equal area, with the middle pulse having an opposite sign from the other two. Hosseini et al. explain this condition well in Fig. 2 of Reference [51]. The rephasing of the AFC and the rephasing due to the electric field gradient are still not perfectly matched in this case, as explained in the discussion on Figure 6.10, but the output pulse amplitude should be larger than in the two pulse case.

To predict the bandwidth broadening for a given electric field, a simple model can be used as given by Equation 6.7:

$$w_{\text{output}} \approx w_{\text{input}} + 2\alpha s \left| E^{\max}_{\text{output}} - E^{\max}_{\text{input}} \right|, \tag{6.7}$$

where w_{input} (w_{output}) is the FWHM in frequency of the input (output) pulse, s is the Stark shift parameter, α is an empirically determined parameter, and $E^{\max}_{\text{input}}$ ($E^{\max}_{\text{output}}$) is the maximum electric field applied during input (output) optical pulses. This is valid for w_{input} smaller than the bandwidth of the AFC. For an approximately linear electric field gradient, the gradient applied during the input pulse would be $\frac{\mathrm{d}E}{\mathrm{d}x} \approx \frac{2E^{\max}_{\text{input}}}{L}$, where L is the length of the resonator. The intuition behind this equation is as follows: w_{input} is the bandwidth of both the input pulse and of the group of ions that is excited by this pulse. When the input is absorbed, there is a gradient induced broadening $\sim 2sE^{\max}_{\text{input}}$ at every frequency point in the comb. When the output pulse is emitted, there is an extra broadening of $\sim 2s \left| E^{\max}_{\text{output}} - E^{\max}_{\text{input}} \right|$ at every point. The factor of α accounts for the nontrivial way in which the local broadening leads to a broadening across the entire excited ion distribution, which depends on the spatial field distribution $E_y(x)$, the structure of the AFC, and the frequency profile of the input pulse.

Figure 6.9 shows a bandwidth changing experiment. The 90-tooth AFC had a width of 143.7 MHz, a finesse of $F \sim 2$, and a period of $\Delta = 1.6$ MHz, leading to a storage time of $t = \frac{1}{\Delta} = 630$ ns. Figure 6.9a shows AFC storage with no bandwidth broadening (top) and maximum achieved broadening (bottom). The broadening in frequency space leads to a narrowing of the output pulse in time. From fits of the output pulses to Gaussians, the temporal FWHMs (Δt) of input and output pulses are extracted and converted to bandwidth or frequency FWHMs (Δf) using: $\Delta f = \frac{4\log 2}{2\pi}(\Delta t)^{-1}$. This relationship follows from the fact that the Fourier transform of a Gaussian pulse in the time domain is a Gaussian in the frequency domain with $2\pi\sigma_f = \sigma_t^{-1}$, and FWHM $= 2\sqrt{\log 2}\sigma$ for a Gaussian pulse with standard deviation σ, $f(t) = e^{-\frac{t^2}{2\sigma^2}}$. Note that the FWHM defined here is for the squared amplitude of the optical pulse $|f(t)|^2$, which is proportional to the number of counts. Figure 6.9b shows the trend of output bandwidth as a function of $E^{\max}_{\text{output}}$. The simple linear model described in Equation 6.7 does not completely capture the effect of the electric field gradient on the output bandwidth. To confirm that the trend observed in the data is expected for this AFC, input pulse, and electric field distribution $E_y(x)$, a simulation of the experiment was performed by numerically integrating the time-evolution equations of the atoms and cavity, as described in the next section. The simulation data reproduces the trend in FWHM vs. field,

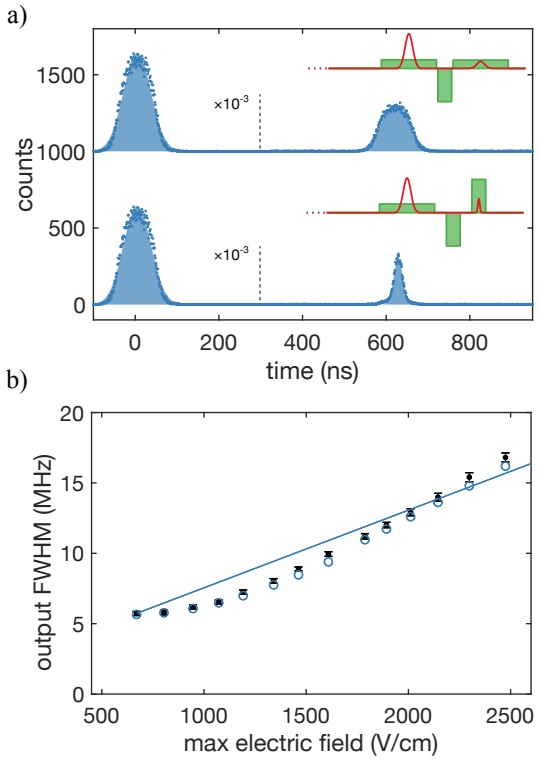

Figure 6.9: AFC storage with bandwidth broadening in αSi-$^{167}Er^{3+}$:Y_2SiO_5 hybrid resonator. (a) Two AFC experiments with electric field gradient pulses. The partially reflected input pulse with FWHM 77.4 ns (5.7 MHz FWHM in the frequency domain) is shown in both traces at $t = 0$, demagnified by a factor of 10^3. The output pulse is at $t = 630$ ns. Circles are photon counts, colored area is a Gaussian fit from which widths are extracted. The top trace shows the case without bandwidth broadening: $E^{max}_{output} = E^{max}_{input} = 0.67$ kV/cm, where the width of the output is 77.1 ± 2.0 ns (5.7 ± 0.1 MHz). The bottom trace shows the maximum bandwidth broadening,$E^{max}_{output} = 4E^{max}_{input} = 2.8$ kV/cm, where the width of the output is 24.3 ± 0.5 ns (18.1 ± 0.4 MHz). Insets show a schematic of the pulse sequences. (b) Bandwidth of pulses as a function of the E^{max}_{output}. In all cases, $E^{max}_{input} = 0.67$ kV/cm. Filled circles are FWHM data, error bars are 95% confidence intervals from Gaussian fits. Solid line is a fit to Equation 6.7, from which $\alpha = 0.24$ is extracted ($s = 11.6$ kHz/(V/cm)). Unfilled circles are QLE simulation data (see main text for details).

although it underestimates the broadening slightly. This discrepancy is thought to be due to the way we modelled the extend of the optical mode along the length of the resonator. In the real device, the optical mode penetrates the photonic crystal and exponentially decays (see Figure 4.3b), whereas in the simulation, we assume a cutoff at an effective optical mode penetration depth of 6 μm beyond the smallest taper hole. This affects the electric field profile experienced by the ions in the simulation (see Figures 4.5b and 4.5f), which in turn affects the predicted broadening. The

effective optical penetration depth of $x_{\text{eff}} = 6\ \mu$m was found by coarsely sweeping x_{eff} in 1 μm increments in this simulation, and choosing the value x_{eff} for which the simulation best matched the data.

Figure 6.10 shows the same output pulses as Figure 6.9a, but overlaid for comparison. Although the widths of the pulses are different, their heights are the same. This means that the energy of the output (proportional to the area of the pulse) is lower when the bandwidth is broadened. Also shown is an output pulse from the same AFC in the case where no electric pulses are used. The amplitude in the no-field case is the same as in the equal field case ($E^{\text{max}}_{\text{output}} = E^{\text{max}}_{\text{input}}$), which indicates that the presence of electric pulses is not causing some dephasing or loss. Rather, the energy of the broadened output pulse is lower because the AFC rephasing and rephasing due to the electric field gradient do not occur on the same timescale. The AFC rephasing always happens over the timescale determined by the input pulse, while the rephasing due to the electric field happens over a timescale that is inversely proportional to the strength of the applied field. Fig. 6.10 also shows an output pulse where only the first two electric pulses are used ($E^{\text{max}}_{\text{output}} = 0$). In this case, we expect the dephasing induced by the first two electric pulses to prevent the emission of an output. The presence of some counts at $t = \frac{1}{\Delta}$ indicates that the electric field gradient experienced by the ions is not ideal. To characterize this, we next look at the ability of a single gradient electric field pulse to prevent an AFC emission in this device.

Figure 6.11 shows the effect of a single electric gradient pulse placed between the input and output of an AFC with period $\Delta = 5$ MHz. This is the same as having only the second pulse in the sequence above. The figure shows the logarithm of the summed counts in the output time bin at $t = \frac{1}{\Delta}$. Because the electric field gradient induces dephasing between the ions, the AFC output should be suppressed. A decay that can be fit with two timescales is observed. We believe this is due to the non-linear electric field variation across the resonator (see Section 4.3), which results in some ions experiencing a high gradient, and some ions experiencing a low gradient. Increasing E^{max} beyond 2.8 kV/(V/cm), or designing electrodes with a more linear field profile $E_y(x)$ should lead to a better suppression of emission.

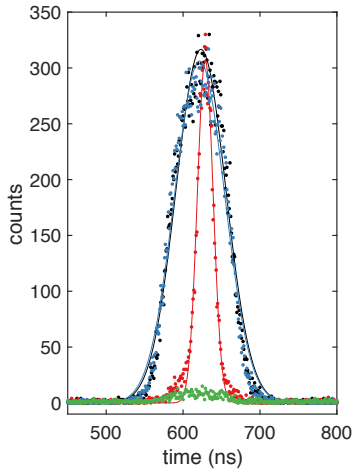

Figure 6.10: Bandwidth experiment efficiency. Output pulses from the experiment in Fig. 6.9 in the case where: no electric field is applied (black), $E^{\max}_{\text{output}} = E^{\max}_{\text{input}}$ (blue), $E^{\max}_{\text{output}} = 4E^{\max}_{\text{input}}$ (red), and where $E^{\max}_{\text{output}} = 0$ (green). Circles represent counts, solid lines are Gaussian fits.

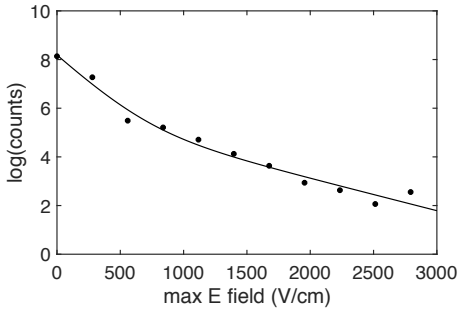

Figure 6.11: Quadrupole field induced dephasing. With electrodes biased in quadrupole configuration, rectangular electric field pulses with width 100 ns were inserted between the input and first emission of an AFC experiment. Data points are sum counts in a time bin centered at $t = \frac{1}{\Delta} = 200$ ns. Solid line is a fit to a double exponential decay. The fast decay rate was 3.6 larger than the slow rate. Note: this data was taken using a different device on the same chip.

Simulation of the Cavity-Ion Ensemble Time Evolution

Simulations of the cavity-ion system were performed to confirm qualitative observations in Section 6.3 and trends in the data in Section 6.4. The code was adapted from one created by Jonathan M. Kindem. These simulations involved numerically solving the following equations of motion for the cavity field a and a number n of ions represented semi-classically as field operators b [36]:

$$\dot{b}_i(t) = -\left(\frac{\gamma}{2} + i\Delta\omega_i(t)\right) b_i(t) - ga(t), \tag{6.8}$$

$$\dot{a}(t) = -\left(\frac{\kappa}{2} + i\Delta\omega_a\right) a(t) + \sum_{i=1}^{n} g b_i(t) - \sqrt{\kappa_{\text{in}}} a_{\text{in}}(t), \tag{6.9}$$

where γ is the ion excitation decay rate, g is the ion-cavity coupling, κ is the total cavity energy decay rate, κ_{in} is the coupling rate of the input field to the cavity (i.e. decay rate through one mirror), and $\Delta\omega_a$ is the cavity detuning (the equations are solved in the rotating frame). $\Delta\omega_i(t)$ is the detuning of each ion, which can vary in time as a function of applied electric field at the location of the ion, $\Delta\omega_i(t) = \Delta\omega_{i,0} \pm sE(x_i, t)$, where $\Delta\omega_{i,0}$ is the detuning of each ion in the absence of an applied electric field (arising from inhomogeneous broadening) and the $\pm$ sign depends on which subclass the ion is in (see Section 6.1).

The cavity field is coupled to external fields as described by input-output formalism. The reflected field a_{r} is related to the cavity field by:

$$a_{\text{r}} = a_{\text{in}} + \sqrt{\kappa_{\text{in}}} a. \tag{6.10}$$

The initial conditions are $a(0) = 0$, $b_i(0) = 0$. $a_{\text{in}}(t)$ describes the time-varying input pulse and $|a_{\text{out}}|^2$=$|a_{\text{r}}|^2$ represents the measured output intensity.

For the simulation, a system of $n + 1$ differential equations (Equations 6.8 and 6.9) are numerically solved using $NDSolve$ in Mathematica. To keep the number of equations to a reasonable size, the number of ions simulated $n \sim 10^4$ is significantly smaller than the true number of ions coupled to the cavity $\sim 10^7$. To accurately represent the absorbing power of the ions, g in the simulation is chosen such that $g_{\text{total}}^2 = ng^2$, where g_{total} is measured from the cavity reflectance curve. The time-independent frequency distribution of the ions (frequency comb with 1 or 2 subclasses) is described as a continuous distribution, and n values of $\Delta\omega_{i,0}$ are sampled from it. For a parallel electrode experiment, a time dependent scalar $\pm sE(x_i, t)$ is added to all ion detunings. For a quadrupole electrode experiment, $E(x_i, t)$ is sampled from a probability distribution $\rho_{\text{ions}}(E_y)$ (see Section 4.3) and varied in amplitude and time to represent each electric pulse.

6.5 Cavity-Ion Coupling and AFC Efficiency in a Hybrid αSi-Y_2SiO_5 Device

In this section, we describe cavity-ion coupling and the AFC storage efficiency in hybrid αSi-$^{167}Er^{3+}$:Y_2SiO_5 devices. As discussed in Section 3.2, the coupling

rate between the cavity and the ensemble of ions in large part determines the AFC storage efficiency in a device. Figure 6.12 shows the measured ion-cavity coupling for the device used in this chapter. The cavity was tuned onto resonance with the 1539 nm transition of the $^{167}Er^{3+}$ ions by freezing nitrogen gas onto the nanobeam at cryogenic temperatures [82]. In our setup, it was difficult to control the rate of gas deposition, so usually the cavity would end up too far to the red (high wavelength) after nitrogen gas tuning. To get the cavity back on resonance, we evaporated some of the nitrogen by heating up the cavity for short periods of time (a few seconds) with high laser power on the order of 100 mW.

Using Equation 5.1, the data in Fig. 6.12 was fit to a model and an ensemble cooperativity was extracted. An estimated $\frac{\kappa_{in}}{\kappa}$ of 0.3 was used in the fit, and the following values were extracted from the fit: $\kappa = 2\pi \times 7.3$ GHz (corresponding to a quality factor of $27{\times}10^3$) along with a $g_{total} = 2\pi{\times}0.64$ GHz, ion distribution FWHM $= 2\pi \times 1.05$ GHz, cooperativity $C = 0.32$. Using partial hyperfine initialization as described in Section 5.2, this cooperativity was improved by a factor of ~ 4 before AFCs were created in each experiment.

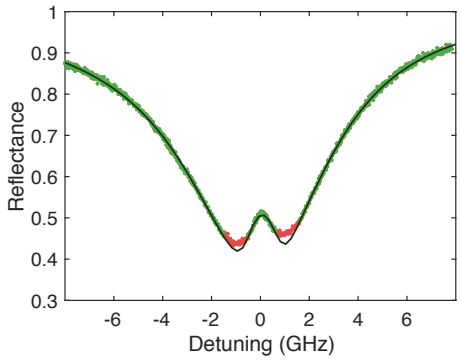

Figure 6.12: Cavity-ion coupling in the hybrid αSi-$^{167}Er^{3+}$:Y_2SiO_5 device. Green and red circles are normalized cavity reflectance data. Solid black line is a fit to green data points. Detuning was measured from 194822 GHz.

Figure 6.13 shows the results of partial hyperfine initialization on a different device (with a lower quality factor) on the same chip. The measured quality factor of the device was 18×10^3, and from the fit, the cooperativity without initialization was found to be $C = 0.13$, and the cooperativity with initialization was found to be $C = 0.53$.

We can use Equations 3.8 and 3.9 to predict the AFC storage efficiency in the device used for the experiments described in this chapter. With a pre-AFC cooperativity

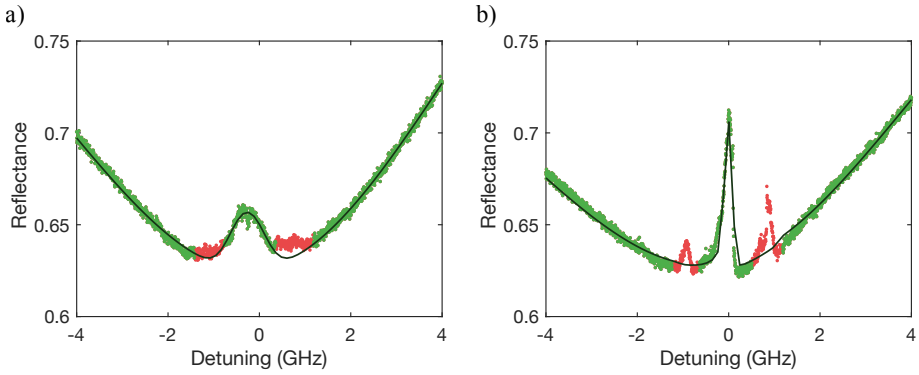

Figure 6.13: Cavity-ion coupling in another hybrid device. Green and red circles are normalized cavity reflectance data. Solid black line is a fit to green data points. (a) Close-up scan of cavity-ion coupling. (b) Cavity-ion coupling after initialization into a few hyperfine states by burning a trench to the right of the main $\Delta m_I = 0$ peak. Detuning is measured from 194822 GHz.

of $0.32 \times 4 = 1.28$ (including a factor of 4 from hyperfine initialization), assuming a comb finesse of $F = 2$, $\frac{\kappa_{\text{in}}}{\kappa}$ of 0.3, and assuming perfect comb initialization, the expected AFC storage efficiency is 1.4%. The efficiency varies with comb finesse, and will therefore vary with the choice of AFC storage time. This is because the comb tooth width is fixed to $\gamma \sim 1$ MHz by superhyperfine broadening, so the comb finesse $F = \Delta/\gamma$ is not independent of comb period Δ.

Figure 6.14 shows an AFC experiment with a relatively short storage time of 200 ns and a storage efficiency of 0.25%. The efficiency of storage was estimated from the ratio between the output and input pulse areas. The input pulse area was first divided by two to account for the fact that half the energy of the input pulse is far off-resonant. This is because a phase EOM is used to control the input frequency, and only the positive sideband is resonant with the cavity and ions. The measured efficiency was lower than the predicted value, likely due to an overestimate of the $\frac{\kappa_{\text{in}}}{\kappa}$ factor or due to imperfect comb initialization, leading to a background of absorbing ions.

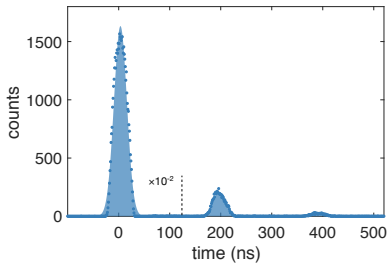

Figure 6.14: AFC efficiency in the hybrid device. Data points are counts, colored areas are fits to Gaussian functions. At $t = 0$ is a reflected input pulse, measured off resonance at 194695.3 GHz. At $t = \frac{1}{\Delta} = 200$ ns is an AFC output pulse. The pulse and AFC were both centered at 194822.0 GHz. The storage efficiency of the AFC is 0.25% (see main text).

6.6 Improving Efficiency in Hybrid Resonators

To increase the efficiency of AFC storage in these devices, the most important device parameters are the quality factor $Q = \frac{\omega}{\kappa_{\text{total}}}$ and the intrinsic quality factor $Q_i = \frac{\omega}{\kappa_i}$, where we define κ_i to be loss into any channel other than the input/output channel. The quality factors are related by:

$$Q = Q_i(1 - \frac{\kappa_{\text{in}}}{\kappa}) \tag{6.11}$$

where κ_{in} is the coupling rate through the input/output mirror and $\frac{\kappa_{\text{in}}}{\kappa}$ is the parameter introduced in Section 3.2 for characterizing how one-sided a cavity is. To make the Q smaller while keeping Q_i the same, one has to make one mirror of the cavity (the input/output mirror) less reflective.

It is essential for the intrinsic quality factor Q_i to be as high as possible, because loss will always reduce the storage efficiency. The total Q of the cavity, on the other hand, has an optimum value. This is because of the impedance matching condition, which demands that the effective cooperativity of the AFC must be $C' = 1$, where $C' \sim \frac{C}{F}$, C is the ensemble cooperativity before comb burning and F is the finesse of the comb.

From Section 3.2, we rewrite Equation 3.16:

$$C \approx \frac{2\sqrt{\pi \log 2}\rho_{\text{ions}}|\mu|^2\beta_{\text{mode}}Q}{\hbar\epsilon_{\text{YSO}}\Delta_{\text{ions}}}.$$

Using $\rho_{\text{ions}} = 135$ ppm, the dipole moment from Reference [74], and the measured inhomogeneous linewidth of $\Delta_{\text{ions}} = 150$ MHz, we can compute the expected

cooperativity using Equation 3.16 for different values of Q and β_{mode}. Then using Equations 3.8 and 3.9, we can compute the theoretical efficiency of AFC storage.

Figure 6.15 shows the predicted AFC efficiencies as a function of intrinsic quality factor, given a finesse of $F = 5$, two values of β_{mode}, and several total quality factors Q. There are a few features to note. First, the efficiency is limited to 76% by the dephasing term (Eq. 3.2), which is only a function of finesse. With superhyperfine broadening limiting the width of teeth to $\gamma \gtrsim 1$ MHz, a higher finesse means a shorter memory time, since $t_{\text{optical storage}} = \frac{1}{\Delta} = \frac{1}{F\gamma}$. Therefore, for a finesse of $F = 5$, the memory time is limited to $t_{\text{optical storage}} \lesssim 200$ ns. Taking into account that two optical π pulses need to fit within the span of $t_{\text{optical storage}}$ in order to implement AFC with spin-wave (see Section 3.1), we cannot make $t_{\text{optical storage}}$ much shorter. Therefore, it seems that $F = 5$ is an upper limit to the comb finesse for spin-wave AFC storage in $^{167}Er^{3+}$:Y_2SiO_5.

Another feature to note is that in Fig. 6.15b, the highest efficiency is achieved for a quality factor of $Q = 40 \times 10^3$, and increasing the quality factor to $Q = 100 \times 10^3$ actually decreases the efficiency. A higher total quality factor is not necessarily better, because of the impedance matching condition, which requires the ensemble cooperativity be 1. On the other hand, the *intrinsic* quality factor should be as high as possible to minimize loss. Finally, by comparing Fig. 6.15a and Fig. 6.15b, it is evident that the requirements for β_{mode} and Q are related by $C \sim \beta_{\text{mode}} \times Q$: with a higher β_{mode} value, a lower Q yields the optimal efficiency.

If we focus on using these types of devices for demonstrations in the near term, Figure 6.15 shows the resonator parameters required to achieve a storage efficiency of 50%. For resonators with the same fraction of optical mode in $^{167}Er^{3+}$:Y_2SiO_5 as those presented in this work ($\beta_{\text{mode}} = 0.1$), the quality factor required would be $Q = 100 \times 10^3$, with an intrinsic quality factor of $Q_i = 500 \times 10^3$. If resonators with $\beta_{\text{mode}} = 0.25$ are used instead, the requirements for the quality factor are slightly lower: $Q = 40 \times 10^3$, with an intrinsic quality factor of $Q_i = 220 \times 10^3$.

One possibility to overcome this superhyperfine limit on efficiency is to find an applied magnetic field for which both the optical ground and excited states are at ZEFOZ points, in order to eliminate superhyperfine coupling. ZEFOZ points are predicted to exist for the hyperfine levels in this material [75, 85]. However, it is not clear whether a magnetic field can be found such that hyperfine levels in both the optical ground and excited states are first-order insensitive to magnetic fields. Additionally, under the new magnetic field, hyperfine levels in the ground state

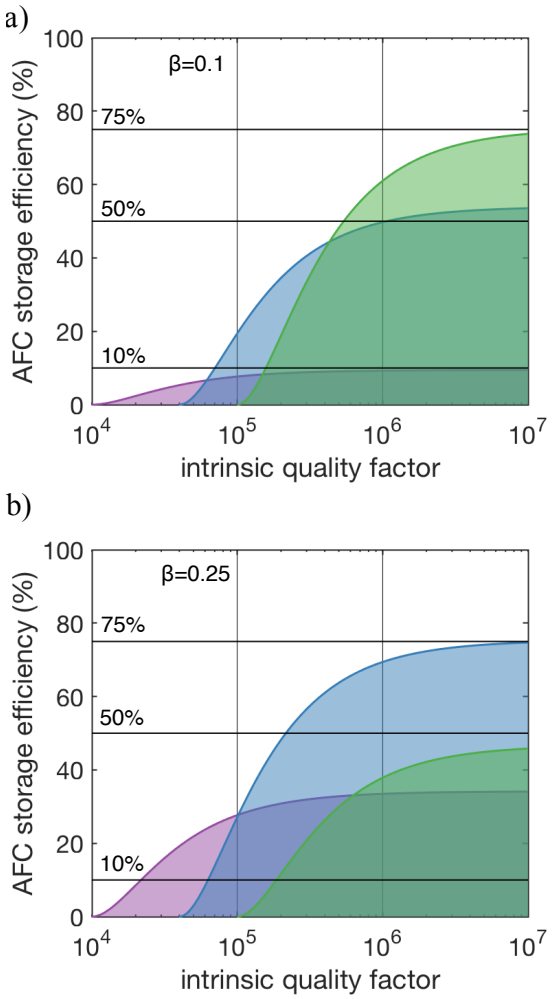

Figure 6.15: Predicted AFC storage efficiency for hybrid αSi-$^{167}Er^{3+}$:Y_2SiO_5 resonators ($F = 5$). a) AFC efficiency versus intrisic quality factor of device Q_i for different total quality factors: $Q = 10 \times 10^3$ (purple), $Q = 40 \times 10^3$ (blue), $Q = 100 \times 10^3$ (green). The fraction of the optical mode in the $^{167}Er^{3+}$:Y_2SiO_5 is assumed to be $\beta_{\text{mode}} = 0.1$. b) AFC efficiency versus intrisic quality factor Q_i with $\beta_{\text{mode}} = 0.25$. Colors represent the same Q values as in (a). The Q values were chosen such that at least one Q value led to the optimal efficiency in each subfigure.

would still need to be long-lived to enable spectral holeburning. Another possibility is to look for a different host material for $^{167}Er^{3+}$ ions, one which does not have nuclear spins and therefore no superhyperfine coupling. If we assume one of these two solutions, then we can increase the finesse value beyond $F = 5$. We can see from the dephasing term (Eq. 3.2) that a finesse larger than $F = 8$ would be necessary for storage efficiencies exceeding 90%.

Assuming a solution for the superhyperfine-coupling limit to comb burning, Figure 6.16 shows the predicted efficiencies for hybrid resonators using a comb finesse of

$F = 15$. Note that the quality factors are larger than those in Figure 6.15, because an increase in finesse must be met with an increase in ensemble cooperativity such that $C' \sim \frac{C}{F} \sim 1$. With this finesse, a storage efficiency of greater than 90% can be achieved, for example with $\beta_{\text{mode}} = 0.25$, $Q = 100 \times 10^3$, and $Q_i = 3 \times 10^6$.

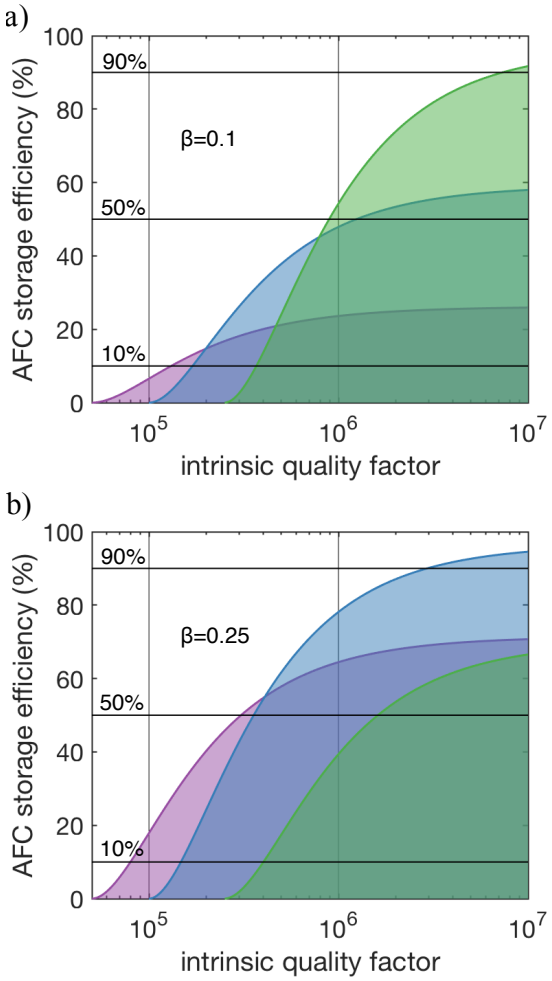

Figure 6.16: Predicted AFC storage efficiency for hybrid αSi-$^{167}Er^{3+}$:Y_2SiO_5 resonators ($F = 15$). a) AFC efficiency versus intrisic quality factor of device Q_i for different total quality factors: $Q = 50 \times 10^3$ (purple), $Q = 100 \times 10^3$ (blue), $Q = 250 \times 10^3$ (green). The fraction of the optical mode in the $^{167}Er^{3+}$:Y_2SiO_5 is assumed to be $\beta_{\text{mode}} = 0.1$. b) AFC efficiency versus intrisic quality factor Q_i with $\beta_{\text{mode}} = 0.25$. Colors represent the same Q values as in (a). The Q values were chosen such that at least one Q value led to the optimal efficiency in each subfigure.

We finally look at the effect of increasing the $^{167}Er^{3+}$ ion concentration. As expected from Equation 3.16, the ion concentration increases the cooperativity. Therefore, increasing the concentration can make a lower quality factor device more efficient. For example, Figure 6.17 shows the predicted efficiency for a resonator with

$Q = 10 \times 10^3$. If the concentration is increased to $\rho_{\text{ions}} = 1000$ ppm, a 50% efficient mirror can be achieved for intrinsic quality factors as low as 60×10^3, which can be easily achieved. However, it is not known whether good coherence properties will be possible in such a highly doped sample, due to $^{167}Er^{3+}$ -$^{167}Er^{3+}$ interactions. Further, this calculation does not take into account any additional inhomogeneous broadening that occurs when the doping concentration is increased (see Reference [18]). Any increase in inhomogeneous broadening would offset the effect of increased concentration on cooperativity due to the $\frac{\rho_{\text{ions}}}{\Delta_{\text{inhom}}}$ term in Equation 3.16.

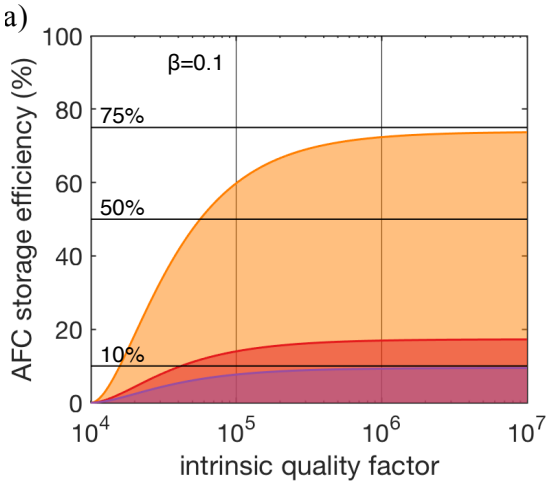

Figure 6.17: Predicted AFC storage efficiency vs. $^{167}Er^{3+}$doping for hybrid αSi-$^{167}Er^{3+}$:Y_2SiO_5 resonators ($F = 5$). a) AFC efficiency versus intrisic quality factor of device Q_i for different $^{167}Er^{3+}$ion concentrations: $\rho_{\text{ions}} = 135$ ppm (purple), $\rho_{\text{ions}} = 200$ ppm (red), $\rho_{\text{ions}} = 1000$ ppm (orange). The fraction of the optical mode in the $^{167}Er^{3+}$:Y_2SiO_5 is assumed to be $\beta_{\text{mode}} = 0.1$, and the quality factor is $Q = 10 \times 10^3$.

Chapter 7

CONCLUSION

7.1 Summary

In this work, we demonstrated on-chip quantum storage of telecommunication wavelength light in two types of on-chip devices.

In a nanobeam photonic crystal resonator milled directly in $^{167}Er^{3+}$:Y_2SiO_5, we showed storage of coherent states at the quantum level using the AFC protocol. Using a double AFC procedure and decoy state analysis, we measured a storage fidelity for single photon states of at least 93.7% ± 2.4%. Storage of multiple temporal modes was demonstrated. The longest storage time achieved was 10 μs, limited by superhyperfince coupling. Storage time in this experiment was fixed by the AFC period Δ, and could not be dynamically changed.

In a hybrid αSi-$^{167}Er^{3+}$:Y_2SiO_5 resonator, we again used the AFC protocol to store light. Four on-chip electrodes, which could be biased in either a quadrupole or a parallel configuration, surrounded the resonator, and provided dynamic control of the ion ensemble through the DC Stark shift. This control was used to dynamically change the memory time $t_{\text{memory}} = \frac{m}{\Delta}$ from $\frac{1}{\Delta} = 50$ ns to $\frac{8}{\Delta} = 400$ ns. By shifting the frequency of the $^{167}Er^{3+}$ ions during emission, we changed the frequency of stored light by ±20 MHz relative to the input frequency. Then, using a quadrupole electrode configuration to broaden the $^{167}Er^{3+}$ ion distribution, the bandwidth of stored light was changed from 5.7 MHz (input) to up to 18 MHz (output).

On the way to these results, we performed spectroscopy on $^{167}Er^{3+}$:Y_2SiO_5 in new parameter regimes, estimated the linear Stark shift parameter in this material (in 2 directions), and analyzed the effects of superhyperfine coupling on storage using the AFC protocol. Despite careful analysis of the AFC storage efficiency in a cavity and efforts in device design and fabrication, the storage efficiency in both of these devices was less than 1%. We outlined a path forward for improving the storage efficiency in these types of devices.

7.2 Future Directions

Toward an Efficient and Long-Lived Quantum Memory

Technical progress is needed to make a more efficient on-chip cavity quantum memory in $^{167}Er^{3+}$:Y_2SiO_5. The storage efficiency in this work for short memory times was $\sim 0.3\%$, while the efficiency most commonly used for simulating realistic near term quantum networks is 90%. The efficiency in this work was mainly limited by a low ensemble cooperativity and loss from the cavity as described by the parameter $\frac{\kappa_{\text{in}}}{\kappa_{\text{total}}}$. Resonators with higher intrinsic quality factors are required. For a hybrid resonator design, the fraction of the mode in the Y_2SiO_5, β_{mode} can also be improved from its current value of 0.1. The cooperativity could also be improved by increasing the $^{167}Er^{3+}$concentration. However, there is a limit to how far the concentration can be beneficially increased.

In addition to the above considerations, it must be mentioned that the total efficiency of storage includes the coupling into and out of the cavity. The one-way coupling efficiency in this work was $\sim 20-50\%$ depending on the type of coupler used. Once the intrinsic memory efficiency is significantly improved, the coupling efficiency should also be increased. For example, tapered fibers [54] could be used to obtain coupling efficiencies exceeding 95% [43, 100].

The memory time must also be increased. For a quantum memory to start to be useful in long distance quantum repeater networks, storage time of $\gtrsim$ 1 ms is necessary [87, 109]. Superhyperfine coupling in this material limits efficient storage on the optical transition using the AFC protocol to $\lesssim$ 200 ns. Spin-wave AFC could extend the memory time to the hyperfine coherence time, which was measured to be longer than 1 s [86]. However, it appears that superhyperfine coupling will also limit the efficiency of storage using a spin-wave AFC protocol, as detailed in Section 6.6. The effect that superhyperfine splitting has on storage using hyperfine levels will also need to be studied. In the sole demonstration of AFC with spin-wave in a rare earth ion with an unpaired electron ($^{171}Yb^{3+}$:Y_2SiO_5), the authors used ZEFOZ transitions for which superhyperfine coupling is strongly suppressed [14]. ZEFOZ hyperfine transitions have been predicted to exist in $^{167}Er^{3+}$:Y_2SiO_5 [75, 85], and could be leveraged for a spin-wave AFC in this material.

$^{167}Er^{3+}$:Y_2SiO_5

$^{167}Er^{3+}$:Y_2SiO_5 has attracted some excitement due to its highly coherent telecommunication wavelength optical transition [19] and highly coherent hyperfine transitions

at microwave frequency [86]. In addition to work using $^{167}Er^{3+}$:Y_2SiO_5 for on-chip quantum memories, there have been recent proposals for using $^{167}Er^{3+}$:Y_2SiO_5 for other quantum applications. Asadi et al. proposed a quantum repeater networks with nodes comprised of two single $^{167}Er^{3+}$:Y_2SiO_5 ions coupled to a cavity [8]. Rakonjac et al. presented measurements of long hyperfine coherence times near zero field [85] and the same group proposed using $^{167}Er^{3+}$:Y_2SiO_5 ions for a microwave quantum memory [107].

Due to the low symmetry of Y_2SiO_5 and due to the high nuclear spin number of $^{167}Er^{3+}$, characterizing the hyperfine levels in this material is not a trivial task. There are twelve 2nd-rank tensors (g, A, and Q, for 2 cystallographic sites, for optical ground and excited states) describing the Zeeman and hyperfine states in $^{167}Er^{3+}$:Y_2SiO_5. Value for some of these tensors have been known since the 2000's [27, 44, 99], and Horvath et al. recently measured the hyperfine tensors in the excited state of site 1 [50]. The excited state hyperfine tensors A and Q for crystallographic site 2 have yet to be measured. Measuring these tensors would be beneficial to continuing the work described in this thesis. For example, knowing the level structure of both excited and ground state manifolds would allow a better understanding of hyperfine initialization and spectral side-structure during comb burning.

For AFC quantum memories, $^{167}Er^{3+}$:Y_2SiO_5 is a good material because it holeburns well at low temperature and moderate field, and because of its long optical and hyperfine coherence times. Additionally, the permanent dipole moment of the ground and excited states in $^{167}Er^{3+}$:Y_2SiO_5 result in a linear DC Stark shift, which was leveraged for dynamic control in this work. However, the strength of the $^4I_{\frac{15}{2}}$ to $^4I_{\frac{13}{2}}$ transition in $^{167}Er^{3+}$:Y_2SiO_5, characterized by an oscillator strength of 2×10^{-7} [74], is weak even when compared to other rare earth ion doped materials. The superhyperfine coupling of the $^{167}Er^{3+}$ electron spin to yttrium nuclei in this material also presents serious complications for AFC quantum storage. By limiting the width of the teeth of the atomic frequency comb, superhyperfine splitting limits the efficiency of storage for all but the shortest storage times.

If the goal is to create an efficient quantum memory at telecom wavelengths using rare earth ions, erbium is the only choice. However, it is possible that erbium ions could have better properties in a crystal other than Y_2SiO_5. Such a crystal would ideally have no nuclear spin. Studies of new erbium-doped materials such as the recent work by Phenicie et al. would be beneficial in this regard [83].

BIBLIOGRAPHY

[1] Y_2SiO_5 ($Y_2[SiO_4]O$ *ht*) crystal structure: Datasheet from "pauling file multinaries edition – 2012" in SpringerMaterials, 2016. URL https://materials.springer.com/isp/crystallographic/docs/sd_1801962. Copyright 2016 Springer-Verlag Berlin Heidelberg & Material Phases Data System (MPDS), Switzerland & National Institute for Materials Science (NIMS), Japan.

[2] I. D. Abella, N. A. Kurnit, and S. R. Hartmann. Photon echoes. *Phys. Rev.*, 141:391–406, Jan 1966. doi: 10.1103/PhysRev.141.391. URL https://link.aps.org/doi/10.1103/PhysRev.141.391.

[3] M. Afzelius and C. Simon. Impedance-matched cavity quantum memory. *Phys. Rev. A*, 82:022310, Aug 2010. doi: 10.1103/PhysRevA.82.022310. URL https://link.aps.org/doi/10.1103/PhysRevA.82.022310.

[4] M. Afzelius, C. Simon, H. de Riedmatten, and N. Gisin. Multimode quantum memory based on atomic frequency combs. *Phys. Rev. A*, 79:052329, May 2009. doi: 10.1103/PhysRevA.79.052329. URL https://link.aps.org/doi/10.1103/PhysRevA.79.052329.

[5] A. L. Alexander, J. J. Longdell, M. J. Sellars, and N. B. Manson. Photon echoes produced by switching electric fields. *Phys. Rev. Lett.*, 96:043602, Feb 2006. doi: 10.1103/PhysRevLett.96.043602. URL https://link.aps.org/doi/10.1103/PhysRevLett.96.043602.

[6] V. R. Almeida, Q. Xu, C. A. Barrios, and M. Lipson. Guiding and confining light in void nanostructure. *Opt. Lett.*, 29(11):1209–1211, Jun 2004. doi: 10.1364/OL.29.001209. URL http://ol.osa.org/abstract.cfm?URI=ol-29-11-1209.

[7] A. Arcangeli, A. Ferrier, and P. Goldner. Stark echo modulation for quantum memories. *Phys. Rev. A*, 93:062303, Jun 2016. doi: 10.1103/PhysRevA.93.062303. URL https://link.aps.org/doi/10.1103/PhysRevA.93.062303.

[8] F. K. Asadi, S. C. Wein, and C. Simon. Long-distance quantum communication with single ^{167}Er ions, 2020. URL https://arxiv.org/abs/2004.02998. Preprint.

[9] M. F. Askarani, M. G. Puigibert, T. Lutz, V. B. Verma, M. D. Shaw, S. W. Nam, N. Sinclair, D. Oblak, and W. Tittel. Storage and reemission of heralded telecommunication-wavelength photons using a crystal waveguide. *Phys. Rev. Applied*, 11:054056, May 2019. doi: 10.

1103/PhysRevApplied.11.054056. URL https://link.aps.org/doi/10.1103/PhysRevApplied.11.054056.

[10] X.-H. Bao, A. Reingruber, P. Dietrich, J. Rui, A. Dück, T. Strassel, L. Li, N.-L. Liu, B. Zhao, and J.-W. Pan. Efficient and long-lived quantum memory with cold atoms inside a ring cavity. *Nat. Phys.*, 8(7):517–521, 2012. ISSN 1745-2481. doi: 10.1038/nphys2324. URL https://doi.org/10.1038/nphys2324.

[11] J. G. Bartholomew. *Investigation of the scalability of rare-earth-ion quantum hardware*. PhD thesis, Australian National University. Laser Physics Centre, 2014. URL http://hdl.handle.net/1885/150124.

[12] J. G. Bartholomew, K. de Oliveira Lima, A. Ferrier, and P. Goldner. Optical line width broadening mechanisms at the 10 kHz Level in Eu^{3+}:Y_2O_3 nanoparticles. *Nano Lett.*, 17(2):778–787, 2017. doi: 10.1021/acs.nanolett.6b03949. URL https://doi.org/10.1021/acs.nanolett.6b03949.

[13] C. H. Bennett and G. Brassard. Quantum cryptography: Public key distribution and coin tossing. *Theor. Comput. Sci.*, 560:7 – 11, 2014. ISSN 0304-3975. doi: https://doi.org/10.1016/j.tcs.2014.05.025. URL http://www.sciencedirect.com/science/article/pii/S0304397514004241. Theoretical Aspects of Quantum Cryptography – celebrating 30 years of BB84.

[14] M. K. Bhaskar, R. Riedinger, B. Machielse, D. S. Levonian, C. T. Nguyen, E. N. Knall, H. Park, D. Englund, M. Lončar, D. D. Sukachev, and M. D. Lukin. Experimental demonstration of memory-enhanced quantum communication. *Nature*, 580(7801):60–64, 2020. ISSN 1476-4687. doi: 10.1038/s41586-020-2103-5. URL https://doi.org/10.1038/s41586-020-2103-5.

[15] M. Bonarota, J.-L. L. Gouët, and T. Chanelière. Highly multimode storage in a crystal. *New J. Phys.*, 13(1):013013, Jan 2011. doi: 10.1088/1367-2630/13/1/013013. URL https://doi.org/10.1088/1367-2630/13/1/013013.

[16] T. Böttger, Y. Sun, C. W. Thiel, and R. L. Cone. Spectroscopy and dynamics of Er^{3+}:Y_2SiO_5 at 1.5μm. *Phys. Rev. B*, 74:075107, Aug 2006. doi: 10.1103/PhysRevB.74.075107. URL https://link.aps.org/doi/10.1103/PhysRevB.74.075107.

[17] T. Böttger, C. W. Thiel, Y. Sun, and R. L. Cone. Optical decoherence and spectral diffusion at 1.5 μm in Er^{3+}:Y_2SiO_5 versus magnetic field, temperature, and Er^{3+} concentration. *Phys. Rev. B*, 73:075101, Feb 2006. doi: 10.1103/PhysRevB.73.075101. URL https://link.aps.org/doi/10.1103/PhysRevB.73.075101.

[18] T. Böttger, C. W. Thiel, R. L. Cone, and Y. Sun. Controlled compositional disorder in Er^{3+}:Y_2SiO_5 provides a wide-bandwidth spectral hole burning material at 1.5 μm. *Phys. Rev. B*, 77:155125, Apr 2008. doi: 10.1103/PhysRevB.77.155125. URL https://link.aps.org/doi/10.1103/PhysRevB.77.155125.

[19] T. Böttger, C. W. Thiel, R. L. Cone, and Y. Sun. Effects of magnetic field orientation on optical decoherence in Er^{3+}:Y_2SiO_5. *Phys. Rev. B*, 79:115104, Mar 2009. doi: 10.1103/PhysRevB.79.115104. URL https://link.aps.org/doi/10.1103/PhysRevB.79.115104.

[20] S. Bratzik, S. Abruzzo, H. Kampermann, and D. Bruß. Quantum repeaters and quantum key distribution: The impact of entanglement distillation on the secret key rate. *Phys. Rev. A*, 87:062335, Jun 2013. doi: 10.1103/PhysRevA.87.062335. URL https://link.aps.org/doi/10.1103/PhysRevA.87.062335.

[21] G. Brennen, E. Giacobino, and C. Simon. Focus on quantum memory. *New J. Phys.*, 17(5):050201, May 2015. doi: 10.1088/1367-2630/17/5/050201. URL https://doi.org/10.1088%2F1367-2630%2F17%2F5%2F050201.

[22] H.-J. Briegel, W. Dür, J. I. Cirac, and P. Zoller. Quantum repeaters: The role of imperfect local operations in quantum communication. *Phys. Rev. Lett.*, 81:5932–5935, Dec 1998. doi: 10.1103/PhysRevLett.81.5932. URL https://link.aps.org/doi/10.1103/PhysRevLett.81.5932.

[23] M. Businger, A. Tiranov, K. T. Kaczmarek, S. Welinski, Z. Zhang, A. Ferrier, P. Goldner, and M. Afzelius. Optical spin-wave storage in a solid-state hybridized electron-nuclear spin ensemble. *Phys. Rev. Lett.*, 124:053606, Feb 2020. doi: 10.1103/PhysRevLett.124.053606. URL https://link.aps.org/doi/10.1103/PhysRevLett.124.053606.

[24] B. Car, L. Veissier, A. Louchet-Chauvet, J.-L. Le Gouët, and T. Chanelière. Selective optical addressing of nuclear spins through superhyperfine interaction in rare-earth doped solids. *Phys. Rev. Lett.*, 120:197401, May 2018. doi: 10.1103/PhysRevLett.120.197401. URL https://link.aps.org/doi/10.1103/PhysRevLett.120.197401.

[25] B. Car, L. Veissier, A. Louchet-Chauvet, J.-L. Le Gouët, and T. Chanelière. Optical study of the anisotropic erbium spin flip-flop dynamics. *Phys. Rev. B*, 100:165107, Oct 2019. doi: 10.1103/PhysRevB.100.165107. URL https://link.aps.org/doi/10.1103/PhysRevB.100.165107.

[26] J.-P. Chen, C. Zhang, Y. Liu, C. Jiang, W. Zhang, X.-L. Hu, J.-Y. Guan, Z.-W. Yu, H. Xu, J. Lin, M.-J. Li, H. Chen, H. Li, L. You, Z. Wang, X.-B. Wang, Q. Zhang, and J.-W. Pan. Sending-or-not-sending with independent lasers: Secure twin-field quantum key distribution over 509 km. *Phys. Rev.*

Lett., 124:070501, Feb 2020. doi: 10.1103/PhysRevLett.124.070501. URL https://link.aps.org/doi/10.1103/PhysRevLett.124.070501.

[27] Y.-H. Chen, X. Fernandez-Gonzalvo, S. P. Horvath, J. V. Rakonjac, and J. J. Longdell. Hyperfine interactions of Er^{3+} ions in Y_2SiO_5: Electron paramagnetic resonance in a tunable microwave cavity. *Phys. Rev. B*, 97: 024419, Jan 2018. doi: 10.1103/PhysRevB.97.024419. URL https://link.aps.org/doi/10.1103/PhysRevB.97.024419.

[28] W. Y. Ching, L. Ouyang, and Y.-N. Xu. Electronic and optical properties of Y_2SiO_5 and $Y_2Si_2O_7$ with comparisons to α-SiO_2 and Y_2O_3. *Phys. Rev. B*, 67:245108, Jun 2003. doi: 10.1103/PhysRevB.67.245108. URL https://link.aps.org/doi/10.1103/PhysRevB.67.245108.

[29] Y.-W. Cho, G. T. Campbell, J. L. Everett, J. Bernu, D. B. Higginbottom, M. T. Cao, J. Geng, N. P. Robins, P. K. Lam, and B. C. Buchler. Highly efficient optical quantum memory with long coherence time in cold atoms. *Optica*, 3(1): 100–107, Jan 2016. doi: 10.1364/OPTICA.3.000100. URL http://www.osapublishing.org/optica/abstract.cfm?URI=optica-3-1-100.

[30] I. Craiciu, M. Lei, J. Rochman, J. M. Kindem, J. G. Bartholomew, E. Miyazono, T. Zhong, N. Sinclair, and A. Faraon. Nanophotonic quantum storage at telecommunication wavelength. *Phys. Rev. Applied*, 12:024062, Aug 2019. doi: 10.1103/PhysRevApplied.12.024062. URL https://link.aps.org/doi/10.1103/PhysRevApplied.12.024062.

[31] I. Craiciu, M. Lei, J. Rochman, and A. Faraon. On-chip telecommunication wavelength quantum memory with DC stark shift control, 2021. Manuscript to be submitted.

[32] J. Dajczgewand, J.-L. L. Gouët, A. Louchet-Chauvet, and T. Chanelière. Large efficiency at telecom wavelength for optical quantum memories. *Opt. Lett.*, 39(9):2711–2714, May 2014. doi: 10.1364/OL.39.002711. URL http://ol.osa.org/abstract.cfm?URI=ol-39-9-2711.

[33] V. Damon, M. Bonarota, A. Louchet-Chauvet, T. Chanelière, and J.-L. L. Gouët. Revival of silenced echo and quantum memory for light. *New J. Phys.*, 13(9):093031, Sep 2011. doi: 10.1088/1367-2630/13/9/093031. URL https://doi.org/10.1088%2F1367-2630%2F13%2F9%2F093031.

[34] H. de Riedmatten, M. Afzelius, M. U. Staudt, C. Simon, and N. Gisin. A solid-state light-matter interface at the single-photon level. *Nature*, 456 (7223):773–777, Dec. 2008. doi: 10.1038/nature07607.

[35] A. M. Dibos, M. Raha, C. M. Phenicie, and J. D. Thompson. Atomic source of single photons in the telecom band. *Phys. Rev. Lett.*, 120:243601, Jun 2018. doi: 10.1103/PhysRevLett.120.243601. URL https://link.aps.org/doi/10.1103/PhysRevLett.120.243601.

[36] I. Diniz, S. Portolan, R. Ferreira, J. M. Gérard, P. Bertet, and A. Auffèves. Strongly coupling a cavity to inhomogeneous ensembles of emitters: Potential for long-lived solid-state quantum memories. *Phys. Rev. A*, 84:063810, Dec 2011. doi: 10.1103/PhysRevA.84.063810. URL https://link.aps.org/doi/10.1103/PhysRevA.84.063810.

[37] J. L. Doualan, C. Labbe, P. L. Boulanger, J. Margerie, R. Moncorge, and H. Timonen. Energy levels of the laser active Er^{3+}ion in each of the two crystallographic sites of yttrium orthosilicate. *J. Phys. Condens. Matter*, 7 (26):5111–5126, jun 1995. doi: 10.1088/0953-8984/7/26/017. URL https://doi.org/10.1088/0953-8984/7/26/017.

[38] R. W. P. Drever, J. L. Hall, F. V. Kowalski, J. Hough, G. M. Ford, A. J. Munley, and H. Ward. Laser phase and frequency stabilization using an optical resonator. *Appl. Phys. B*, 31:97–105, 1983.

[39] L.-M. Duan, M. D. Lukin, J. I. Cirac, and P. Zoller. Long-distance quantum communication with atomic ensembles and linear optics. *Nature*, 414(6862): 413–418, 2001. ISSN 1476-4687. doi: 10.1038/35106500. URL https://doi.org/10.1038/35106500.

[40] W. Dür, H.-J. Briegel, J. I. Cirac, and P. Zoller. Quantum repeaters based on entanglement purification. *Phys. Rev. A*, 59:169–181, Jan 1999. doi: 10.1103/PhysRevA.59.169. URL https://link.aps.org/doi/10.1103/PhysRevA.59.169.

[41] M. Fleischhauer and M. D. Lukin. Dark-state polaritons in electromagnetically induced transparency. *Phys. Rev. Lett.*, 84:5094–5097, May 2000. doi: 10.1103/PhysRevLett.84.5094. URL https://link.aps.org/doi/10.1103/PhysRevLett.84.5094.

[42] F. R. Graf, A. Renn, U. P. Wild, and M. Mitsunaga. Site interference in stark-modulated photon echoes. *Phys. Rev. B*, 55:11225–11229, May 1997. doi: 10.1103/PhysRevB.55.11225. URL https://link.aps.org/doi/10.1103/PhysRevB.55.11225.

[43] S. Gröblacher, J. T. Hill, A. H. Safavi-Naeini, J. Chan, and O. Painter. Highly efficient coupling from an optical fiber to a nanoscale silicon optomechanical cavity. *Appl. Phys. Lett.*, 103(18):181104, 2013. doi: 10.1063/1.4826924. URL https://doi.org/10.1063/1.4826924.

[44] O. Guillot-Noël, P. Goldner, Y. L. Du, E. Baldit, P. Monnier, and K. Bencheikh. Hyperfine interaction of Er^{3+} ions in Y_2SiO_5: An electron paramagnetic resonance spectroscopy study. *Phys. Rev. B*, 74:214409, Dec 2006. doi: 10.1103/PhysRevB.74.214409. URL https://link.aps.org/doi/10.1103/PhysRevB.74.214409.

[45] O. Guillot-Noël, H. Vezin, P. Goldner, F. Beaudoux, J. Vincent, J. Lejay, and I. Lorgeré. Direct observation of rare-earth-host interactions in Er:Y_2SiO_5. *Phys. Rev. B*, 76:180408, Nov 2007. doi: 10.1103/PhysRevB.76.180408. URL https://link.aps.org/doi/10.1103/PhysRevB.76.180408.

[46] S. R. Hastings-Simon, B. Lauritzen, M. U. Staudt, J. L. M. van Mechelen, C. Simon, H. de Riedmatten, M. Afzelius, and N. Gisin. Zeeman-level lifetimes in Er^{3+}:Y_2SiO_5. *Phys. Rev. B*, 78:085410, Aug 2008. doi: 10.1103/PhysRevB.78.085410. URL https://link.aps.org/doi/10.1103/PhysRevB.78.085410.

[47] M. P. Hedges, J. J. Longdell, Y. Li, and M. J. Sellars. Efficient quantum memory for light. *Nature*, 465(7301):1052–1056, 2010. ISSN 1476-4687. doi: 10.1038/nature09081. URL https://doi.org/10.1038/nature09081.

[48] G. Heinze, C. Hubrich, and T. Halfmann. Stopped light and image storage by electromagnetically induced transparency up to the regime of one minute. *Phys. Rev. Lett.*, 111:033601, Jul 2013. doi: 10.1103/PhysRevLett.111.033601. URL https://link.aps.org/doi/10.1103/PhysRevLett.111.033601.

[49] K. Heshami, D. G. England, P. C. Humphreys, P. J. Bustard, V. M. Acosta, J. Nunn, and B. J. Sussman. Quantum memories: Emerging applications and recent advances. *J. Mod. Opt.*, 63(20):2005–2028, 2016. doi: 10.1080/09500340.2016.1148212. URL https://doi.org/10.1080/09500340.2016.1148212.

[50] S. P. Horvath, J. V. Rakonjac, Y.-H. Chen, J. J. Longdell, P. Goldner, J.-P. R. Wells, and M. F. Reid. Extending phenomenological crystal-field methods to C_1 point-group symmetry: Characterization of the optically excited hyperfine structure of $^{167}Er^{3+}$:Y_2SiO_5. *Phys. Rev. Lett.*, 123:057401, Jul 2019. doi: 10.1103/PhysRevLett.123.057401. URL https://link.aps.org/doi/10.1103/PhysRevLett.123.057401.

[51] M. Hosseini, B. M. Sparkes, G. Hétet, J. J. Longdell, P. K. Lam, and B. C. Buchler. Coherent optical pulse sequencer for quantum applications. *Nature*, 461(7261):241–245, 2009. doi: 10.1038/nature08325. URL https://doi.org/10.1038/nature08325.

[52] M. Hosseini, B. M. Sparkes, G. Campbell, P. K. Lam, and B. C. Buchler. High efficiency coherent optical memory with warm rubidium vapour. *Nat. Commun.*, 2(1):174, 2011. ISSN 2041-1723. doi: 10.1038/ncomms1175. URL https://doi.org/10.1038/ncomms1175.

[53] Y.-F. Hsiao, P.-J. Tsai, H.-S. Chen, S.-X. Lin, C.-C. Hung, C.-H. Lee, Y.-H. Chen, Y.-F. Chen, I. A. Yu, and Y.-C. Chen. Highly efficient coherent optical memory based on electromagnetically induced transparency. *Phys. Rev.*

Lett., 120:183602, May 2018. doi: 10.1103/PhysRevLett.120.183602. URL https://link.aps.org/doi/10.1103/PhysRevLett.120.183602.

[54] Y. Q. Huan. Efficient coupling of tapered optical fibers to silicon nanophotonic waveguides on rare-earth doped crystals, 2019. URL https://resolver.caltech.edu/CaltechTHESIS:06032019-143215628. Senior Thesis, California Institute of Technology.

[55] J. D. Joannopoulos, S. G. Johnson, J. N. Winn, and R. D. Meade. *Periodic Dielectric Waveguides*, pages 122–134. Princeton University Press, rev - revised, 2 edition, 2008. ISBN 9780691124568. URL http://www.jstor.org/stable/j.ctvcm4gz9.11.

[56] P. Jobez, I. Usmani, N. Timoney, C. Laplane, N. Gisin, and M. Afzelius. Cavity-enhanced storage in an optical spin-wave memory. *New J. Phys.*, 16 (8):083005, aug 2014. doi: 10.1088/1367-2630/16/8/083005. URL https://doi.org/10.1088/1367-2630/16/8/083005.

[57] S. G. Johnson and J. D. Joannopoulos. Block-iterative frequency-domain methods for maxwell's equations in a planewave basis. *Opt. Express*, 8 (3):173–190, Jan 2001. doi: 10.1364/OE.8.000173. URL http://www.opticsexpress.org/abstract.cfm?URI=oe-8-3-173.

[58] H. J. Kimble. The quantum internet. *Nature*, 453:1023–1030, 2008. doi: 10.1038/nature07127.

[59] A. E. Kozhekin, K. Mølmer, and E. Polzik. Quantum memory for light. *Phys. Rev. A*, 62:033809, Aug 2000. doi: 10.1103/PhysRevA.62.033809. URL https://link.aps.org/doi/10.1103/PhysRevA.62.033809.

[60] B. Kraus, W. Tittel, N. Gisin, M. Nilsson, S. Kröll, and J. I. Cirac. Quantum memory for nonstationary light fields based on controlled reversible inhomogeneous broadening. *Phys. Rev. A*, 73:020302, Feb 2006. doi: 10.1103/PhysRevA.73.020302. URL https://link.aps.org/doi/10.1103/PhysRevA.73.020302.

[61] N. Kukharchyk, D. Sholokhov, O. Morozov, S. L. Korableva, A. A. Kalachev, and P. A. Bushev. Optical coherence of ^{166}Er:^{7}LiYF$_4$ crystal below 1 K. *New J. Phys.*, 20(2):023044, feb 2018. doi: 10.1088/1367-2630/aaa7e4. URL https://doi.org/10.1088\%2F1367-2630\%2Faaa7e4.

[62] B. Lauritzen, S. R. Hastings-Simon, H. de Riedmatten, M. Afzelius, and N. Gisin. State preparation by optical pumping in erbium-doped solids using stimulated emission and spin mixing. *Phys. Rev. A*, 78:043402, Oct 2008. doi: 10.1103/PhysRevA.78.043402. URL https://link.aps.org/doi/10.1103/PhysRevA.78.043402.

[63] B. Lauritzen, J. Minář, H. de Riedmatten, M. Afzelius, N. Sangouard, C. Simon, and N. Gisin. Telecommunication-wavelength solid-state memory at the single photon level. *Phys. Rev. Lett.*, 104:080502, Feb 2010. doi: 10.1103/PhysRevLett.104.080502. URL https://link.aps.org/doi/10.1103/PhysRevLett.104.080502.

[64] B. Lauritzen, J. Minář, H. de Riedmatten, M. Afzelius, and N. Gisin. Approaches for a quantum memory at telecommunication wavelengths. *Phys. Rev. A*, 83:012318, Jan 2011. doi: 10.1103/PhysRevA.83.012318. URL https://link.aps.org/doi/10.1103/PhysRevA.83.012318.

[65] S.-K. Liao, W.-Q. Cai, J. Handsteiner, B. Liu, J. Yin, L. Zhang, D. Rauch, M. Fink, J.-G. Ren, W.-Y. Liu, Y. Li, Q. Shen, Y. Cao, F.-Z. Li, J.-F. Wang, Y.-M. Huang, L. Deng, T. Xi, L. Ma, T. Hu, L. Li, N.-L. Liu, F. Koidl, P. Wang, Y.-A. Chen, X.-B. Wang, M. Steindorfer, G. Kirchner, C.-Y. Lu, R. Shu, R. Ursin, T. Scheidl, C.-Z. Peng, J.-Y. Wang, A. Zeilinger, and J.-W. Pan. Satellite-relayed intercontinental quantum network. *Phys. Rev. Lett.*, 120:030501, Jan 2018. doi: 10.1103/PhysRevLett.120.030501. URL https://link.aps.org/doi/10.1103/PhysRevLett.120.030501.

[66] G. Liu and B. Jacquier, editors. *Spectroscopic Properties of Rare Earths in Optical Materials*, pages 1 – 94. Springer-Verlag Berlin Heidelberg, 2005. ISBN 9783642062834. URL https://www.springer.com/gp/book/9783540238867.

[67] G. Liu and B. Jacquier, editors. *Spectroscopic Properties of Rare Earths in Optical Materials*, pages 320 – 378. Springer-Verlag Berlin Heidelberg, 2005. ISBN 9783642062834. URL https://www.springer.com/gp/book/9783540238867.

[68] X. Ma, B. Qi, Y. Zhao, and H.-K. Lo. Practical decoy state for quantum key distribution. *Phys. Rev. A*, 72:012326, Jul 2005. doi: 10.1103/PhysRevA.72.012326. URL https://link.aps.org/doi/10.1103/PhysRevA.72.012326.

[69] R. M. Macfarlane. Optical stark spectroscopy of solids. *J. Lumin.*, 125(1):156 – 174, 2007. ISSN 0022-2313. doi: https://doi.org/10.1016/j.jlumin.2006.08.012. URL http://www.sciencedirect.com/science/article/pii/S0022231306005837. Festschrift in Honor of Academician Alexander A. Kaplyanskii.

[70] Y. M. Maksimov. Properties of modified quantum dynamics. *Sov. Phys. J.*, 19(5):595–598, 1976. ISSN 1573-9228. doi: 10.1007/BF00952558. URL https://doi.org/10.1007/BF00952558.

[71] F. Marsili, V. B. Verma, J. A. Stern, S. Harrington, A. E. Lita, T. Gerrits, I. Vayshenker, B. Baek, M. D. Shaw, R. P. Mirin, and S. W. Nam. Detecting single infrared photons with 93% system efficiency. *Nat. Photonics*, 7(3):

210–214, 2013. ISSN 1749-4893. doi: 10.1038/nphoton.2013.13. URL https://doi.org/10.1038/nphoton.2013.13.

[72] S. Marzban. *Rare-earth ion doped planar waveguides for integrated quantum photonics*. PhD thesis, College of Science, The Australian National University, 2017. URL http://hdl.handle.net/1885/144606.

[73] S. Marzban, J. G. Bartholomew, S. Madden, K. Vu, and M. J. Sellars. Observation of photon echoes from evanescently coupled rare-earth ions in a planar waveguide. *Phys. Rev. Lett.*, 115:013601, Jul 2015. doi: 10.1103/PhysRevLett.115.013601. URL https://link.aps.org/doi/10.1103/PhysRevLett.115.013601.

[74] D. L. McAuslan, J. J. Longdell, and M. J. Sellars. Strong-coupling cavity qed using rare-earth-metal-ion dopants in monolithic resonators: What you can do with a weak oscillator. *Phys. Rev. A*, 80:062307, Dec 2009. doi: 10.1103/PhysRevA.80.062307. URL https://link.aps.org/doi/10.1103/PhysRevA.80.062307.

[75] D. L. McAuslan, J. G. Bartholomew, M. J. Sellars, and J. J. Longdell. Reducing decoherence in optical and spin transitions in rare-earth-metal-ion–doped materials. *Phys. Rev. A*, 85:032339, Mar 2012. doi: 10.1103/PhysRevA.85.032339. URL https://link.aps.org/doi/10.1103/PhysRevA.85.032339.

[76] M. M. Minnegaliev, K. I. Gerasimov, R. V. Urmancheev, and S. A. Moiseev. Quantum memory in the revival of silenced echo scheme in an optical resonator. *Quantum Electron.*, 48(10):894–897, oct 2018. doi: 10.1070/qel16762. URL https://doi.org/10.1070%2Fqel16762.

[77] E. Miyazono. *Nanophotonic Resonators for Optical Quantum Memories based on Rare-Earth-Doped Materials*. PhD thesis, California Institute of Technology, 2017. URL https://resolver.caltech.edu/CaltechTHESIS:03152017-114949088.

[78] E. Miyazono, T. Zhong, I. Craiciu, and A. Kindem, Jonathan M.and Faraon. Coupling of erbium dopants to yttrium orthosilicate photonic crystal cavities for on-chip optical quantum memories. *Appl. Phys. Lett.*, 108(1):011111, 2016. doi: 10.1063/1.4939651. URL https://doi.org/10.1063/1.4939651.

[79] E. Miyazono, I. Craiciu, A. Arbabi, T. Zhong, and A. Faraon. Coupling erbium dopants in yttrium orthosilicate to silicon photonic resonators and waveguides. *Opt. Express*, 25(3):2863–2871, Feb 2017. doi: 10.1364/OE.25.002863. URL http://www.opticsexpress.org/abstract.cfm?URI=oe-25-3-2863.

[80] S. A. Moiseev, S. N. Andrianov, and F. F. Gubaidullin. Efficient multimode quantum memory based on photon echo in an optimal qed cavity. *Phys. Rev. A*, 82:022311, Aug 2010. doi: 10.1103/PhysRevA.82.022311. URL https://link.aps.org/doi/10.1103/PhysRevA.82.022311.

[81] K. Momma and F. Izumi. VESTA3 for three-dimensional visualization of crystal, volumetric and morphology data. *J. Appl. Crystallogr.*, 44(6):1272–1276, Dec 2011. doi: 10.1107/S0021889811038970. URL https://doi.org/10.1107/S0021889811038970.

[82] S. Mosor, J. Hendrickson, B. C. Richards, J. Sweet, G. Khitrova, H. M. Gibbs, T. Yoshie, A. Scherer, O. B. Shchekin, and D. G. Deppe. Scanning a photonic crystal slab nanocavity by condensation of xenon. *Appl. Phys. Lett.*, 87(14):141105, 2005. doi: 10.1063/1.2076435. URL https://doi.org/10.1063/1.2076435.

[83] C. M. Phenicie, P. Stevenson, S. Welinski, B. C. Rose, A. T. Asfaw, R. J. Cava, S. A. Lyon, N. P. de Leon, and J. D. Thompson. Narrow optical line widths in erbium implanted in tio2. *Nano Lett.*, 19(12):8928–8933, 2019. doi: 10.1021/acs.nanolett.9b03831. URL https://doi.org/10.1021/acs.nanolett.9b03831. PMID: 31765161.

[84] M. Raha, S. Chen, C. M. Phenicie, S. Ourari, A. M. Dibos, and J. D. Thompson. Optical quantum nondemolition measurement of a single rare earth ion qubit. *Nat. Commun.*, 11(1):1605, 2020. ISSN 2041-1723. doi: 10.1038/s41467-020-15138-7. URL https://doi.org/10.1038/s41467-020-15138-7.

[85] J. V. Rakonjac, Y.-H. Chen, S. P. Horvath, and J. J. Longdell. Spin echoes in the ground and an optically excited state of $^{167}Er^{3+}$:Y_2SiO_5 at near-zero magnetic fields using raman heterodyne spectroscopy, 2018. URL https://arxiv.org/abs/1802.03862.

[86] M. Rančić, M. P. Hedges, R. L. Ahlefeldt, and M. J. Sellars. Coherence time of over a second in a telecom-compatible quantum memory storage material. *Nat. Phys.*, 14:50–54, 2018. doi: 10.1038/nphys4254.

[87] M. Razavi, M. Piani, and N. Lütkenhaus. Quantum repeaters with imperfect memories: Cost and scalability. *Phys. Rev. A*, 80:032301, Sep 2009. doi: 10.1103/PhysRevA.80.032301. URL https://link.aps.org/doi/10.1103/PhysRevA.80.032301.

[88] J. Ruggiero, J.-L. Le Gouët, C. Simon, and T. Chanelière. Why the two-pulse photon echo is not a good quantum memory protocol. *Phys. Rev. A*, 79:053851, May 2009. doi: 10.1103/PhysRevA.79.053851. URL https://link.aps.org/doi/10.1103/PhysRevA.79.053851.

[89] M. Sabooni, S. T. Kometa, A. Thuresson, S. Kröll, and L. Rippe. Cavity-enhanced storage—preparing for high-efficiency quantum memories. *New J. Phys.*, 15(3):035025, Mar 2013. doi: 10.1088/1367-2630/15/3/035025. URL https://doi.org/10.1088%2F1367-2630%2F15%2F3%2F035025.

[90] E. Saglamyurek, N. Sinclair, J. Jin, J. A. Slater, D. Oblak, F. Bussières, M. George, R. Ricken, W. Sohler, and W. Tittel. Broadband waveguide quantum memory for entangled photons. *Nature*, 469(7331):512–515, 2011. ISSN 1476-4687. doi: 10.1038/nature09719. URL https://doi.org/10.1038/nature09719.

[91] E. Saglamyurek, J. Jin, V. B. Verma, M. D. Shaw, F. Marsili, S. W. Nam, D. Oblak, and W. Tittel. Quantum storage of entangled telecom-wavelength photons in an erbium-doped optical fibre. *Nat. Photonics*, 9:83–87, 2015. doi: 10.1038/nphoton.2014.311.

[92] N. Sangouard, C. Simon, H. de Riedmatten, and N. Gisin. Quantum repeaters based on atomic ensembles and linear optics. *Rev. Mod. Phys.*, 83:33–80, Mar 2011. doi: 10.1103/RevModPhys.83.33. URL https://link.aps.org/doi/10.1103/RevModPhys.83.33.

[93] D. Schraft, M. Hain, N. Lorenz, and T. Halfmann. Stopped light at high storage efficiency in a Pr^{3+}:Y_2SiO_5 crystal. *Phys. Rev. Lett.*, 116:073602, Feb 2016. doi: 10.1103/PhysRevLett.116.073602. URL https://link.aps.org/doi/10.1103/PhysRevLett.116.073602.

[94] A. Seri, A. Lenhard, D. Rieländer, M. Gündoğan, P. M. Ledingham, M. Mazzera, and H. de Riedmatten. Quantum correlations between single telecom photons and a multimode on-demand solid-state quantum memory. *Phys. Rev. X*, 7:021028, May 2017. doi: 10.1103/PhysRevX.7.021028. URL https://link.aps.org/doi/10.1103/PhysRevX.7.021028.

[95] A. Seri, G. Corrielli, D. Lago-Rivera, A. Lenhard, H. de Riedmatten, R. Osellame, and M. Mazzera. Laser-written integrated platform for quantum storage of heralded single photons. *Optica*, 5(8):934–941, Aug 2018. doi: 10.1364/OPTICA.5.000934. URL http://www.osapublishing.org/optica/abstract.cfm?URI=optica-5-8-934.

[96] C. Simon, H. de Riedmatten, M. Afzelius, N. Sangouard, H. Zbinden, and N. Gisin. Quantum repeaters with photon pair sources and multimode memories. *Phys. Rev. Lett.*, 98:190503, May 2007. doi: 10.1103/PhysRevLett.98.190503. URL https://link.aps.org/doi/10.1103/PhysRevLett.98.190503.

[97] N. Sinclair, E. Saglamyurek, H. Mallahzadeh, J. A. Slater, M. George, R. Ricken, M. P. Hedges, D. Oblak, C. Simon, W. Sohler, and W. Tittel. Spectral multiplexing for scalable quantum photonics using an atomic frequency comb quantum memory and feed-forward control. *Phys. Rev.*

Lett., 113:053603, Jul 2014. doi: 10.1103/PhysRevLett.113.053603. URL https://link.aps.org/doi/10.1103/PhysRevLett.113.053603.

[98] N. J. Stone. Table of Nuclear Magnetic Dipole and Electric Quadrupole Moments. Technical report, International Atomic Energy Agency (IAEA), 2014. URL http://inis.iaea.org/search/search.aspx?orig{_}q=RN:45029196.

[99] Y. Sun, T. Böttger, C. W. Thiel, and R. L. Cone. Magnetic g tensors for the $^4I_{15/2}$ and $^4I_{13/2}$ states of Er^{3+}:Y_2SiO_5. *Phys. Rev. B*, 77:085124, Feb 2008. doi: 10.1103/PhysRevB.77.085124. URL https://link.aps.org/doi/10.1103/PhysRevB.77.085124.

[100] T. G. Tiecke, K. P. Nayak, J. D. Thompson, T. Peyronel, N. P. de Leon, V. Vuletić, and M. D. Lukin. Efficient fiber-optical interface for nanophotonic devices. *Optica*, 2(2):70–75, Feb 2015. doi: 10.1364/OPTICA.2.000070. URL http://www.osapublishing.org/optica/abstract.cfm?URI=optica-2-2-70.

[101] I. Usmani, M. Afzelius, H. de Riedmatten, and N. Gisin. Mapping multiple photonic qubits into and out of one solid-state atomic ensemble. *Nat. Commun.*, 1(1):12, 2010. doi: 10.1038/ncomms1010. URL https://doi.org/10.1038/ncomms1010.

[102] R. Valivarthi, M. G. Puigibert, Q. Zhou, G. H. Aguilar, V. B. Verma, F. Marsili, M. D. Shaw, S. W. Nam, D. Oblak, and W. Tittel. Quantum teleportation across a metropolitan fibre network. *Nat. Photonics*, 10(10):676–680, 2016. ISSN 1749-4893. doi: 10.1038/nphoton.2016.180. URL https://doi.org/10.1038/nphoton.2016.180.

[103] Y. Wang, J. Li, S. Zhang, K. Su, Y. Zhou, K. Liao, S. Du, H. Yan, and S.-L. Zhu. Efficient quantum memory for single-photon polarization qubits. *Nat. Photonics*, 13(5):346–351, 2019. ISSN 1749-4893. doi: 10.1038/s41566-019-0368-8. URL https://doi.org/10.1038/s41566-019-0368-8.

[104] S. Wehner, D. Elkouss, and R. Hanson. Quantum internet: A vision for the road ahead. *Science*, 362(6412), 2018. ISSN 0036-8075. doi: 10.1126/science.aam9288. URL https://science.sciencemag.org/content/362/6412/eaam9288.

[105] S. Welinski, C. W. Thiel, J. Dajczgewand, A. Ferrier, R. L. Cone, R. M. Macfarlane, T. Chanelière, A. Louchet-Chauvet, and P. Goldner. Effects of disorder on optical and electron spin linewidths in Er^{3+}, Sc^{3+}:Y_2SiO_5. *Opt. Mater.*, 63:69–75, 2017. doi: 10.1016/j.optmat.2016.09.039.

[106] Y. Wen, P. Zhou, Z. Xu, L. Yuan, M. Wang, S. Wang, L. Chen, and H. Wang. Cavity-enhanced and long-lived optical memories for two orthogonal polarizations in cold atoms. *Opt. Express*, 28(1):360–368, Jan

2020. doi: 10.1364/OE.376962. URL http://www.opticsexpress.org/abstract.cfm?URI=oe-28-1-360.

[107] L. A. Williamson, Y.-H. Chen, and J. J. Longdell. Magneto-optic modulator with unit quantum efficiency. *Phys. Rev. Lett.*, 113:203601, Nov 2014. doi: 10.1103/PhysRevLett.113.203601. URL https://link.aps.org/doi/10.1103/PhysRevLett.113.203601.

[108] W. K. Wootters and W. H. Zurek. A single quantum cannot be cloned. *Nature*, 299(5886):802–803, 1982. ISSN 1476-4687. doi: 10.1038/299802a0. URL https://doi.org/10.1038/299802a0.

[109] Y. Wu, J. Liu, and C. Simon. Near-term performance of quantum repeaters with imperfect ensemble-based quantum memories. *Phys. Rev. A*, 101:042301, Apr 2020. doi: 10.1103/PhysRevA.101.042301. URL https://link.aps.org/doi/10.1103/PhysRevA.101.042301.

[110] Y. Yu, F. Ma, X.-Y. Luo, B. Jing, P.-F. Sun, R.-Z. Fang, C.-W. Yang, H. Liu, M.-Y. Zheng, X.-P. Xie, W.-J. Zhang, L.-X. You, Z. Wang, T.-Y. Chen, Q. Zhang, X.-H. Bao, and J.-W. Pan. Entanglement of two quantum memories via fibres over dozens of kilometres. *Nature*, 578(7794):240–245, 2020. ISSN 1476-4687. doi: 10.1038/s41586-020-1976-7. URL https://doi.org/10.1038/s41586-020-1976-7.

[111] Q. Zhang, F. Xu, Y.-A. Chen, C.-Z. Peng, and J.-W. Pan. Large scale quantum key distribution: Challenges and solutions (invited). *Opt. Express*, 26(18):24260–24273, Sep 2018. doi: 10.1364/OE.26.024260. URL http://www.opticsexpress.org/abstract.cfm?URI=oe-26-18-24260.

[112] M. Zhong, M. P. Hedges, R. L. Ahlefeldt, J. G. Bartholomew, S. E. Beavan, S. M. Wittig, J. J. Longdell, and M. J. Sellars. Optically addressable nuclear spins in a solid with a six-hour coherence time. *Nature*, 517:177–180, 2015. doi: 10.1038/nature14025.

[113] T. Zhong, J. M. Kindem, E. Miyazono, and A. Faraon. Nanophotonic coherent light-matter interfaces based on rare-earth-doped crystals. *Nat. Commun.*, 6:8206, 2015.

[114] T. Zhong, J. Rochman, J. M. Kindem, E. Miyazono, and A. Faraon. High quality factor nanophotonic resonators in bulk rare-earth doped crystals. *Opt. Express*, 24(1):536–544, Jan 2016. doi: 10.1364/OE.24.000536. URL http://www.opticsexpress.org/abstract.cfm?URI=oe-24-1-536.

[115] T. Zhong, J. M. Kindem, J. G. Bartholomew, J. Rochman, I. Craiciu, E. Miyazono, M. Bettinelli, E. Cavalli, V. Verma, S. W. Nam, F. Marsili, M. D. Shaw, A. D. Beyer, and A. Faraon. Nanophotonic rare-earth quantum memory with optically controlled retrieval. *Science*, 2017. ISSN 0036-8075. doi: 10.1126/science.aan5959. URL http://science.sciencemag.org/content/early/2017/09/05/science.aan5959.

Appendix A

SIMULATION OF HYBRID αSi-$^{167}Er^{3+}$:Y_2SiO_5 RESONATORS

This appendix details how to simulate the bandgap and reflectance of an αSi-$^{167}Er^{3+}$:Y_2SiO_5 photonic crystal mirror, as was done in Figure 4.3. The bandgaps (Fig. 4.3a) were computed using the harmonic mode solver MPB [57]. The reflectance of the photonic crystal mirror with tapers (Fig. 4.3b) was simulated in COMSOL Multiphysics.

A.1 Calculating Photonic Crystal Bandgap Using MPB

This is the code used to obtain the photonic crystal mirror bandgaps. The code is in Scheme, compatible with the Scheme user interface of MPB (a Python interface is also available). To find TM modes, we solve for modes with an even symmetry in the y direction.

```
(set-param! resolution 30)      ; pixels/a

(define-param a 0.370)          ; units of um
(define-param d1 0.230)         ; units of um
(define-param d2 0.250)         ; units of um
(define-param h 0.310)          ; units of um
(define-param w 0.605)          ; units of um

(set! d1 (/ d1 a))          ; units of "a"
(set! d2 (/ d2 a))          ; units of "a"
(set! h (/ h a))            ; units of "a"
(set! w (/ w a))            ; units of "a"

(define-param sc-x 1)           ; cell depth
(define-param sc-y 4)           ; cell width
(define-param sc-z 4)           ; cell height

(set! geometry-lattice (make lattice (size sc-x sc-y sc-z)))

(define-param nSi 3.50)
(define-param nYSO 1.8)
(define Si (make dielectric (index nSi)))
(define YSO (make dielectric (index nYSO)))
```

```
(set! geometry (list
        (make block (center 0 0 0) (size infinity w h) (material Si))
        (make ellipsoid (center 0 0 0) (size d1 d2 infinity) (material air))
        (make block (center 0 0 (* 0.25 (+ sc-z h)))
(size infinity infinity (* 0.5 (- sc-z h))) (material YSO))
))

(set! k-points (list (vector3 0.25 0 0)
                     (vector3 0.5 0 0)))

(define-param num-kpoints 53)
(set! k-points (interpolate num-kpoints k-points))
(set-param! num-bands 4)

;TM mode
(run-yeven)
```

To run the above code, save it as a *.ctl* file, then run it from the Terminal using the following command:

```
mpb photonic_crystal_bandgap.ctl | tee "output.out"
grep yevenfreqs: "output.out" |cut -d , -f3,7- |sed 1d > "output.dat"
```

To plot the bands (f vs. k), import the *.dat* file into MATLAB (or any other plotting software). The first column of the data is the wavenumber data in units of $\frac{ka}{2\pi}$, where k is the wavenumber and a is the unit cell dimension along the axis of propagation. The following columns of the data are frequency, in units of $\frac{fa}{c}$, where f is the frequency, and c is the speed of light.

A.2 Calculating Waveguide Band Diagram Using MPB

For the waveguide band diagram, a similar code is used, but the unit cell dimention in the direction of propagation is ∞ instead of a. To run the code and plot the output data, use the same procedure as detailed in the previous section.

```
(set-param! resolution 30)          ; pixels/a

(define-param a 0.370)          ; units of um
(define-param h 0.310)          ; units of um
(define-param w 0.605)          ; units of um
```

```
(set! h (/ h a))            ; units of "a"
(set! w (/ w a))            ; units of "a"

(define-param sc-y 4)           ; cell width
(define-param sc-z 4)           ; cell height

(set! geometry-lattice (make lattice (size no-size sc-y sc-z)))

(define-param nSi 3.50)
(define-param nYSO 1.8)
(define Si (make dielectric (index nSi)))
(define YSO (make dielectric (index nYSO)))

(set! geometry (list
        (make block (center 0 0 0) (size infinity w h) (material Si))
        (make block (center 0 0 (* 0.25 (+ sc-z h)))
(size infinity infinity (* 0.5 (- sc-z h)))  (material YSO))
))

(set! k-points (list (vector3 0 0 0)
                     (vector3 1 0 0)))

(define-param num-kpoints 53)
(set! k-points (interpolate num-kpoints k-points))

(set-param! num-bands 4)

;TM mode
(run-yeven)
```

A.3 Calculating Reflectance of Mirror With Taper Using Comsol

The reflectance of the mirror with tapers was simulated in COMSOL Multiphysics 5.4 using the Electromagnetic Waves, Frequency Domain package. The photonic crystal mirror was simulated in 3D, as shown in Figure A.1. Ports 1 and 2 were *Numeric* ports. A three step Study was used: (1) Boundary Mode Analysis at Port 1, (2) Boundary Mode Analysis at Port 2, and (3) Frequency Domain. For the Boundary Mode Analyses, modes with effective index $n_{\text{eff}} = 2.5$ were found, matching the TM mode in the waveguide (see Fig. 4.2). The Reflectance value was found from the Frequency Domain step.

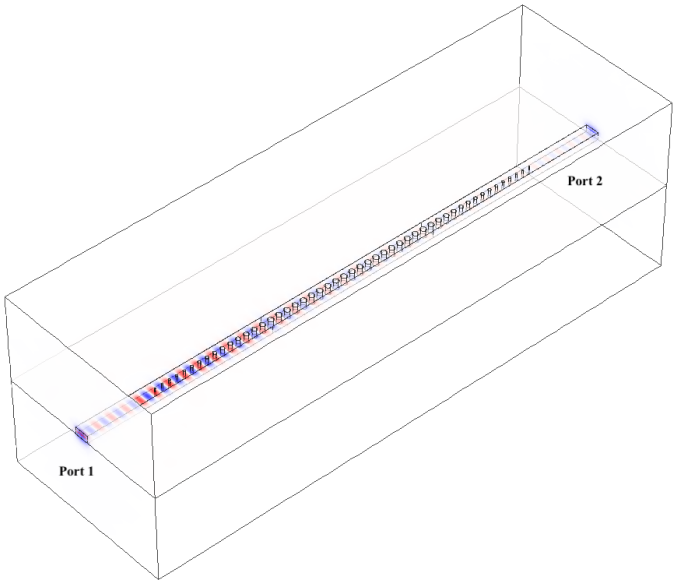

Figure A.1: 3D photonic crystal mirror COMSOL Simulation

Appendix B

FABRICATION PROCESS FOR ELECTRODES

Before electrode fabrication:

- Start with a Y_2SiO_5 chip
- Add 20 μm $\times$ 20 μm gold alignment markers, using the same procedure as for depositing and patterning electrodes, described below.
- Deposit, pattern and etch amorphous silicon resonators, aligned to the gold markers.

Deposit and pattern gold electrodes, as follows:

Clean Y_2SiO_5 substrate:

- Rinse chip with each of the following for 30 s: acetone, IPA, DI water
- Dry chip with N_2, then bake on hot plate at 100 °C for 1 minutes

Spin 950PMMA A5 positive resist:

- Cover $\sim 2/3$ of chip area with resist
- Spin: 2500 rpm/20 acc/60 s
- Bake on hot plate at 180 °C for 1 minute
- Allow chip to cool off for 2 minutes

Spin aquaSAVE antistatic agent on top of resist:

- Cover entire chip area
- Spin: 1500 rpm/10 acc/60 s
- Bake on hot plate at 70 °C for 5 minutes

Aligned electron beam write (Raith EBPG 5200):

- Mount chip onto a holder with movable clips, and use dummy chip to set height
- Pattern electrodes using aligned e-beam write, using gold alignment markers
- Dose: 1000 $\mu C/cm^2$; current: up to 100 nA

Develop resist:

- Dip the chip in DI water momentarily to remove aquaSAVE
- Dip the chip in 3:1 IPA:MIBK solution for 30 s
- Immediately rinse off with a constant stream of IPA for 30 s
- Dry chip with N_2

Deposit gold (Lesker Labline Ebeam Evaporator):

- Mount chip onto a glass slide using Kapton tape and mount slide in evaporator
- Deposit 10 nm Ti (adhesion layer) and 100 nm gold, both at 1 Å/s

Gold lift-off:

- Place chip in acetone for 2 hours
- Rinse chip while submerged with a jet of acetone for 2 minutes
- Rinse in IPA and DI water for 30 s each
- Dry chip with N_2

Appendix C

MEASUREMENT SETUP FOR CHAPTER 5

Here we describe the measurement setup used in Chapter 5. Figure C.1 shows a schematic of the setup. For details on the components used, see Section D.3. Some components used in this experiment differ, and will be noted below.

The $^{167}Er^{3+}$:Y_2SiO_5 chip was mounted on a gold-coated copper plate with indium metal, and the plate was secured atop a stack of attocube xyz nanopositioners. The copper plate was thermally linked using a copper braid to the mixing chamber plate of a BlueFors dilution fridge, which had a temperature of $T \sim 25$ mK.

A fiber-coupled tunable external-cavity diode laser was used to probe the nanobeam device and implement the AFC storage protocol.

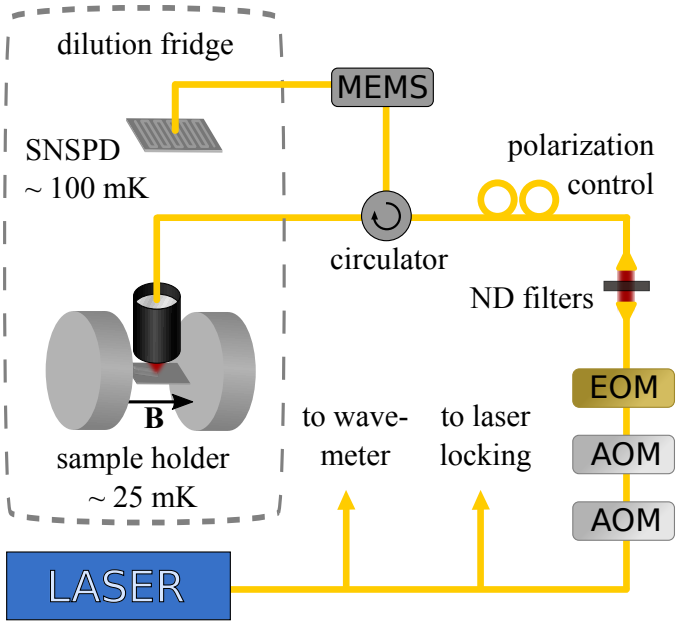

Figure C.1: Measurement setup for Chapter 5 (adapted from Ref. [30]). Details in main text.

One percent of the laser light was directed to a wavemeter for measurement. Another $\sim$ 1% of the light was picked off and sent to a locking setup, in which the laser frequency was stabilized by locking to a home-built fiber cavity using the Pound-Drever-Hall technique [38]. The fiber cavity was made by splicing two ends of a 4×4 fiber-optic 99/1 splitter together. It had a linewidth of 4 MHz and a free spectral

range of 230 MHz. Temperature and vibration stabilization was accomplished by placing the fiber cavity inside a box of sand, and placing that box inside a foam-lined box. Two Newport LB1005 servo controller boxes were used to feed back to the laser current and piezo voltage.

The laser light was directed to the sample through two acousto-optical modulators (AOMs) for pulse shaping. The AOMs were driven by RF sources with variable power. RF switches between the drivers and AOMs were used to block any leakage current from the drivers.

An electro-optic phase modulator (EOM) was used to control the phase of the light or to add strong sidebands for hyperfine initialization. To drive the EOM, one of two RF sources was used: (1) a voltage controlled oscillator (Minicircuits ZX95-1300+) amplified using a JDSU H301-1210 amplifer or (2) the pulsed output of the arbitrary wave generator (AWG). A Minicircuits ZASWA-2-50DR+ switch toggled between the two RF sources as needed. Source (1) was used for hyperfine initialization before comb burning. Source (2) was used for adding a π phased shift to the time bin qubit when needed. Source (2) was also used with a 0 bias at all other times in the experiment (no phase modulation).

Neutral density (ND) filters and polarization paddles provided attenuation and polarization control, respectively. A fiber optic circulator directed light to the $^{167}Er^{3+}$:Y_2SiO_5 crystal located inside a dilution refrigerator. An aspheric lens pair focused light from an optical fiber onto the angled coupler of the resonator. The coupling into the device was optimized by moving the xyz nanopositioners.

Light from the resonator was directed by the circulator onto a superconducting nanowire single photon detector (SNSPD) at $\sim$ 100 mK [71]. Strong initialization pulses were prevented from reaching the SNSPD by a micro electro-mechanical switch (MEMS). A magnetic field $\mathbf{B}$ = 380 mT was applied to the sample, parallel to the D_1 crystal axis, using two cylindrical permanent magnets.

A tuning line (1/4" copper pipe) pointing at the sample was used to spray nitrogen gas onto the resonator to tune its resonance frequency.

A 4-channel AWG with 8 digital markers was used to control and synchronize the AOM drivers, the VCO (EOM), and the MEMS switch. For details and MATLAB code see Reference [77].

Appendix D

MEASUREMENT SETUPS FOR CHAPTER 6

This section describes the measurement setup used in Chapter 6. For almost all measurements in this chapter, the setup shown in Figure D.1 was used. For the frequency shift experiment, a frequency sensitive measurement was required, so the setup was modified to allow for heterodyne detection, as shown in Figure D.3.

D.1 Measurements with SNSPD

Figure D.1 shows a schematic of the setup. For details on the components used, see Section D.3. Figure D.2 shows a picture of the setup.

The setup is very similar to the one described in Appendix C.

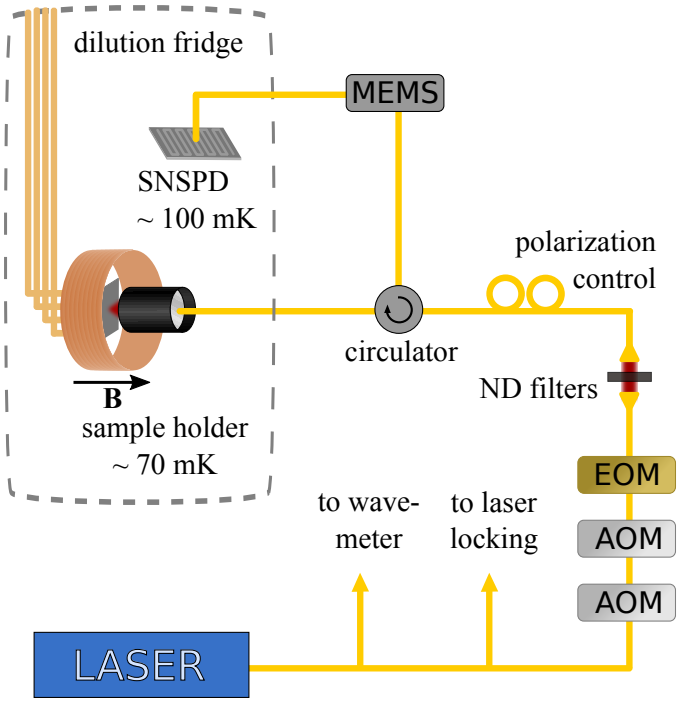

Figure D.1: Measurement setup for Chapter 6 with SNSPD. Details in main text.

The $^{167}Er^{3+}$:Y_2SiO_5 chip was mounted on a copper chuck using PELCO conductive silver paint. A custom PCB board with 4 SMP connectors was secured on top of the chuck. Aluminum wire bonds provided electrical contact between gold contact pads on the chip and the PCB board (see inset of Fig. D.2). The copper chuck was thermally linked to the mixing chamber plate of a BlueFors dilution fridge via a

copper rod screwed into a copper assembly. The temperature of the mixing chamber plate was $70 - 90$ mK.

A fiber-coupled tunable external-cavity diode laser was used to probe the nanobeam device and implement the AFC storage protocol.

One percent of the laser light was directed to a wavemeter for measurement. Another $\sim 1\%$ of the light was picked off and sent to a locking setup, in which the laser frequency was stabilized by locking to a Stable Laser Systems cavity using the Pound-Drever-Hall technique [38]. Details of the locking setup are included in Table D.3.

The laser light was directed to the sample through two acousto-optical modulators (AOMs) for pulse shaping. The AOMs were driven by RF sources with variable power. RF switches between the drivers and AOMs were used to block any leakage current from the drivers.

An electro-optic phase modulator (EOM) was used to add strong sidebands to the laser frequency. An amplified voltage controlled oscillator (HMC-C029) was used to drive the EOM at frequencies between 5 and 8 GHz. Only the negative first order sideband was resonant with $^{167}Er^{3+}$:Y_2SiO_5 transitions. The two first-order sidebands were not equal in size: the negative one was larger and was measured to contain $\sim 50\%$ of the optical energy. The amplitude of the negative sideband was not perfectly constant over the tuning range.

Neutral density (ND) filters and polarization paddles provided attenuation and polarization control, respectively. A fiber optic circulator directed light to the $^{167}Er^{3+}$:Y_2SiO_5 crystal located inside a dilution refrigerator. An aspheric lens pair, mounted on a stack of attocube xyz nanopositioners, focused light from an optical fiber onto the grating coupler of the resonator. The coupling into the device was optimized by moving the xyz nanopositioners.

Light from the resonator was directed by the circulator onto a superconducting nanowire single photon detector (SNSPD) at ~ 100 mK [71]. Strong initialization pulses were prevented from reaching the SNSPD by a micro electro-mechanical switch (MEMS). A magnetic field $\mathbf{B} = 980$ mT was applied to the sample, parallel to the D_1 crystal axis, using a home-build superconducting electromagnet. Trim coils on either side of the electromagnet cancelled out stray magnetic field along the crystal b axis. The stray field was likely caused by misalignment of the solenoid symmetry axis with the crystal D_1 axis, and we estimated it to be on the order of 30

mT before cancellation.

A tuning line (1/4" copper pipe) pointing at the sample was used to spray nitrogen gas onto the resonator to tune its resonance frequency.

A 4-channel AWG with 8 digital markers was used to control and synchronize the AOM drivers, the VCO (EOM), and the MEMS switch. For details and MATLAB code see Reference [77].

A 2-channel waveform generator (10 Vpp) was used to generate the electric pulses for DC Stark shift control. The output of each channel was split in 2 using a Minicircuits ZSC-2-1+ power splitter, for a total of 4 channels. For the frequency shift measurement, a DC coupled power splitter (Minicircuits ZFRSC-2050+) was used instead. Electric pulses were sent to the chip (PCB board with SMP connectors) via a coaxial chain with "0 dB" attenuators at every stage of the dilution fridge.

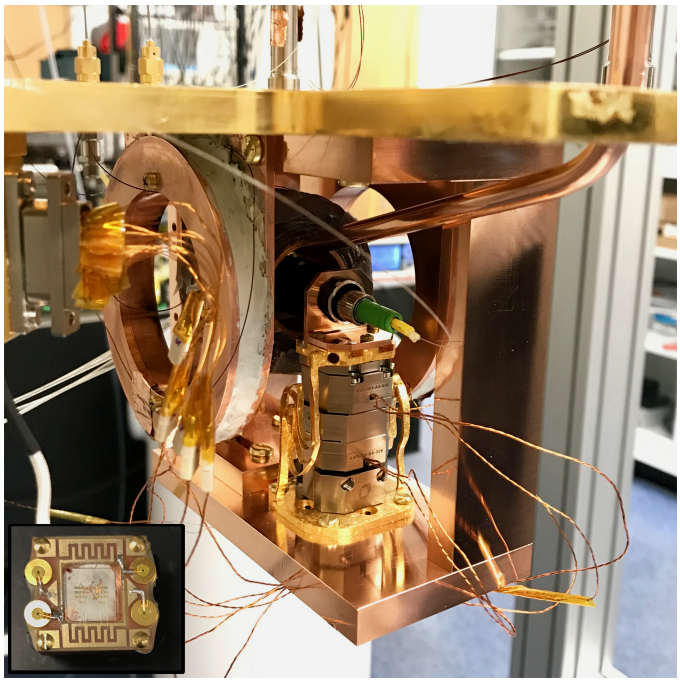

Figure D.2: Picture of measurement setup in Chapter 6. Visible are: the copper assembly connected to the mixing chamber plate (gold); the attocube nanopositioners with wiring; the optical fiber and the 1/2" lens tube containing the lens pair for coupling; the solenoid electromagnet; two magnet trim coils to the left and right of the solenoid; and the copper tuning line pointing at the sample. Not visible are the sample and the SMA cables behind the sample. The inset on the bottom left shows an old sample mounted on a copper chuck and electrically connected with wire-bonds to a custom PCB board with 4 SMP connectors.

D.2 Heterodyne Detection

This section presents the heterodyne measurement setup used for the frequency shift measurement in Chapter 6 (Figure 6.6) and for the T_2 measurement in Fig. 2.4.

In a heterodyne measurement, a small signal $E_s e^{i\omega_s t}$ is combined with a large local oscillator $E_{LO} e^{i\omega_{LO} t}$ on a photodetector, leading to an electronic signal at the beat-note frequency $E(t) = E_s E_{LO} \cos((\omega_s - \omega_{LO})t)$. The local oscillator E_{LO} boosts the small signal amplitude to $E_s E_{LO}$, making it detectable using a photodetector and oscilloscope. Because the electronic signal from the photodetector varies sinusoidally with frequency $f_{het} = \frac{\omega_s - \omega_{LO}}{2\pi}$, and ω_{LO} is known, the frequency of the small signal ω_s can also be measured using this method, by taking the Fourier transform of the photodetector signal. This is how the frequency of the output pulse is measured in Chapter 6.

Figure D.3 shows the heterodyne measurement setup. The laser, wavemeter, laser locking and EOM are all the same as in the previous section. After the EOM, the signal is split using a fiber-optic splitter into the signal arm and the local oscillator (LO) arm. Only the 100 MHz AOM is used in this case, and only on the signal arm. This AOM sets the heterodyne frequency $f_{het} = 100$ MHz, as the signal arm and local oscillator arm differ by 100 MHz (as we have said, the signal frequency can vary – in this case it will vary around 100 MHz). The signal arm goes through additional attenuation, described below, then through the circulator and to the sample. The output signal from the sample goes through the circulator and is combined with the local oscillator with another fiber-optic splitter. Both signals are then measured on a photodetector (photoreceiver). The photodetector signal is amplified using two amplifiers and measured on an oscilloscope (see Table D.2 for part names).

The relative phase between the local oscillator and signal is not stable in this configuration. For this reason, there is significant jitter on the 100 MHz sinusoidal signal, and averaging this signal for improved signal-to-noise would yield zero. For this reason, individual frames are saved from the oscilloscope using the FastFrame feature, then the absolute value of the Fourier transform of the signal is computed. These spectra are then averaged together for improved signal-to-noise.

Coming back to the signal arm, the reason there are two paths after the AOM is because the input signal that probes the AFC still needs to be quite strong (~ 0.12 mW) in order to create an output detectable using our heterodyne setup (the local oscillator power is ~ 0.5 mW). However, this input power level is too strong to create the atomic frequency comb, and the extinction ratio of the AOM is too small

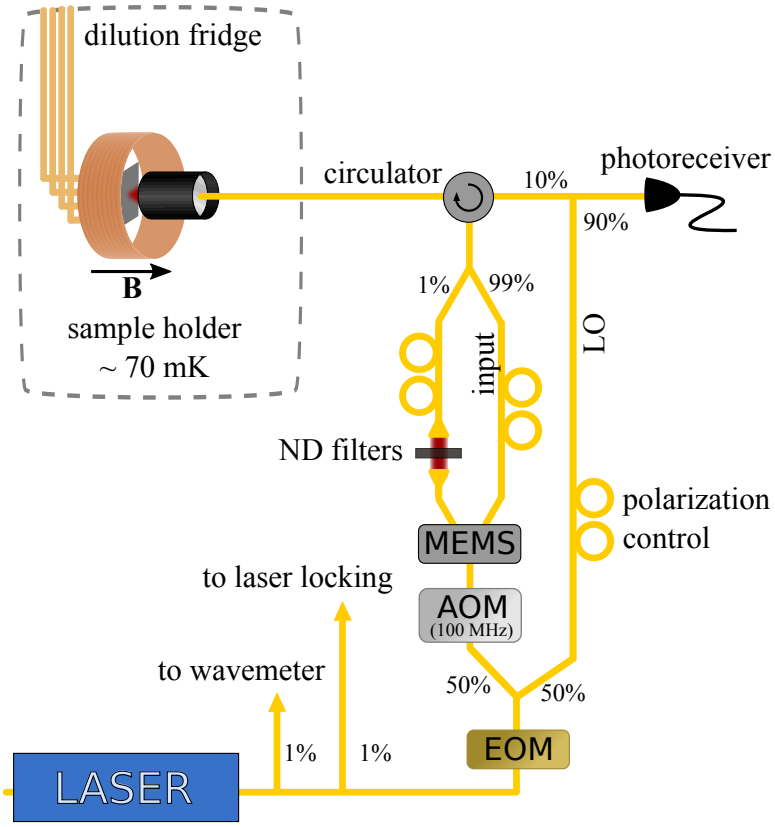

Figure D.3: Measurement setup for Chapter 6 with Heterodyne detection. Details in main text.

to supply both sufficiently high input power and sufficiently low comb burning power. For this reason, there are two paths that split and recombine on the signal arm: the strong "input" arm, and the weak comb burning arm. The MEMS switch sends light through either of the two paths during the experiment as needed.

D.3 Parts List

Tables D.1-D.3 list the part numbers used in the measurement setups.

Part	**Type**
laser	Toptical CTL, 1490 nm - 1580 nm, 50 mW
wavemeter	Bristol 671A
AOM 1	Brimrose AMM-100-20-25-1536-2FP (100 MHz)
AOM 2	Brimrose IPM-500-100-5-1536-2FP (500 MHz)
EOM	iXBlue MPZ-LN-10-P-P-FA-FA (10 GHz)
fiber-coupled splitters	Thorlabs or Oz Optics (PM before modulators)
	Thorlabs or Oz Optics (SM after modulators)
neutral density filters	Thorlabs (C coated)
polarization paddles	Thorlabs (SM)
circulator	Thorlabs (SM)
lens pair	Thorlabs C230260P-C
MEMS	Sercalo SW1x2_9N
SNSPD	WSi from NASA JPL
photoreceiver	Newport 1611 (1 GHz)

Table D.1: Optical components

Part	**Type**
arbitrary wave generator	AWG5014
waveform generator	Agilent Keysight 33622A
voltage controlled oscillator	Analog Devices HMC-C029
amplifier 1	Minicircuits ZFL-1000LN+
amplifier 2	Minicircuits ZX60-P103LN+
oscilloscope	Tektronix TDS7014
RF driver (AOM 1)	Brimrose FFA-100-B1-F0.5 (100 MHz)
RF driver 2 (AOM 2)	Brimrose FFA-500-B1-F1 (500 MHz)
RF switch x2 (for AOM drivers)	ZASWA-2-50DR+

Table D.2: Electronic components

Part	Type
EOM (PDH)	iXBlue MPX-LN-0.1-P-P-FA-FA (150 MHz)
EOM (offset)	iXBlue MPZ-LN-10-P-P-FA-FA (10 GHz)
laser servo electronics	Vescent D2-125
stable cavity	Stable Laser Systems (custom)
function generator	SRS DS345 (PDH EOM)
RF signal generator	WindFreak SynthNV (offset EOM)
photodetector	Thorlabs PDA05CF2

Table D.3: Laser frequency locking components